

Louisiana Tech University

**Louisiana Tech Digital Commons**

---

Doctoral Dissertations

Graduate School

---

Fall 2019

**Dual Purpose Tunable Vibration Isolator Energy Harvester: Design,  
Fabrication, Modeling and Characterization**

S. M. Mahdi Mofidian

Follow this and additional works at: <https://digitalcommons.latech.edu/dissertations>

---

**DUAL PURPOSE TUNABLE VIBRATION ISOLATOR ENERGY  
HARVESTER: DESIGN, FABRICATION, MODELING AND  
CHARACTERIZATION**

by

S. M. Mahdi Mofidian, B.S., M.S.

A Dissertation Presented in Partial Fulfillment  
of the Requirements of the Degree  
Doctor of Philosophy

COLLEGE OF ENGINEERING AND SCIENCE  
LOUISIANA TECH UNIVERSITY

November 2019

LOUISIANA TECH UNIVERSITY

GRADUATE SCHOOL

August 5, 2019

---

Date of dissertation defense

We hereby recommend that the dissertation prepared by

S. M. Mahdi Mofidian, B.S., M.S.

---

entitled **DUAL PURPOSE TUNABLE VIBRATION ISOLATION ENERGY**

---

**HARVESTER:DESIGN, FABRICATION, MODELING AND**

---

**CHARACTERIZATION**

---

be accepted in partial fulfillment of the requirements for the degree of

**Doctor of Philosophy in Engineering, Micro & Nanoscale Systems Conc.**

---

---

Dr. Hamzeh Bardaweel, Supervisor of Dissertation Research

---

Dr. Shengnian Wang,  
Head of Engineering

**Members of the Doctoral Committee:**

Dr. Prabhu Arumugam

Dr. Arden Moore

Dr. Leland Weiss

Dr. Sandra Zivanovic

**Approved:**

**Approved:**

---

Hisham Hegab

Dean of Engineering & Science

---

Ramu Ramachandran

Dean of the Graduate School

## ABSTRACT

This dissertation is focused on design, fabrication, characterization, and modeling of a unique dual purpose vibration isolation energy harvesting system. The purpose of the system is to, simultaneously, attenuate unwanted vibrations and scavenge kinetic energy available in these vibrations. This study includes theoretical modeling and experimental work to fully characterize and understand the dynamic behavior of the fabricated dual purpose system. In the theoretical study, both numerical (Runge-Kutta) and analytical (Harmonic Balance Method, HBM) methods are used to obtain the dynamic behavior of the system. The system features a combination of mechanical and electromagnetic components to facilitate its dual functionality. The system consists of a magnetic spring, mechanical flat spring, and dampers. The combination of negative stiffness of the magnetic spring with positive stiffness of the mechanical spring results in lowering the cut off frequency of the system. Lowering the cut off frequency improves the device's ability to operate in a wider range of frequencies. Results from dynamic measurements and model simulation confirm the ability of the device to function in both vibration isolation and energy harvesting modes simultaneously. The dual-purpose device is able to attenuate vibrations higher than 12.5 [Hz]. The device also produces 26.8 [mW] output power at 1g [ $\text{m/s}^2$ ] and 9.75 [Hz]. Performance metrics of the device including displacement transmissibility and energy conversion efficiency are formulated. Results show that for low acceleration levels, lower damping values are desirable and yield

higher energy conversion efficiencies and improved vibration isolation. At higher acceleration, there is a trade-off where lower damping values worsen vibration isolation but yield higher conversion efficiencies.

## **APPROVAL FOR SCHOLARLY DISSEMINATION**

The author grants to the Prescott Memorial Library of Louisiana Tech University the right to reproduce, by appropriate methods, upon request, any or all portions of this Dissertation. It is understood that “proper request” consists of the agreement, on the part of the requesting party, that said reproduction is for his personal use and that subsequent reproduction will not occur without written approval of the author of this Dissertation. Further, any portions of the Dissertation used in books, papers, and other works must be appropriately referenced to this Dissertation.

Finally, the author of this Dissertation reserves the right to publish freely, in the literature, at any time, any or all portions of this Dissertation.

Author: S. M. Mahdi Mofidian

Date: Oct/08/2019

## **DEDICATION**

Dedicated to my beloved father for his measureless support from the Heaven, and  
my beloved

***Mother***

For her endless love, support and encouragement.

## TABLE OF CONTENTS

|   |      |
|---|------|
| ABSTRACT.....   | iii  |
| APPROVAL FOR SCHOLARLY DISSEMINATION .....  | v    |
| DEDICATION .....  | vi   |
| LIST OF FIGURES .....   | ix   |
| LIST OF TABLES .....  | xiii |
| ACKNOWLEDGMENTS .....   | xiv  |
| CHAPTER 1 INTRODUCTION .....  | 1    |
| 1.1    Description of the Problem.....  | 1    |
| 1.2    Objective of the Work.....   | 2    |
| 1.3    State of the Art .....   | 4    |
| 1.4    Structure of Dissertation .....  | 10   |
| CHAPTER 2 DISPLACEMENT TRANSMISSIBILITY EVALUATION OF<br>VIBRATION ISOLATION SYSTEM EMPLOYING NONLINEAR DAMPING AND<br>NONLINEAR STIFFNESS ELEMENTS ..... | 12   |
| 2.1    Introduction.....  | 12   |
| 2.2    System Description and Structure.....  | 16   |
| 2.3    Static Characterization of a System with “n” Oblique Springs .....   | 18   |
| 2.4    Nonlinearity Analysis .....  | 20   |
| 2.5    Dynamic and Non-dimensional Analysis .....   | 24   |
| 2.6    Analytical Solution .....  | 25   |
| CHAPTER 3 THEORETICAL STUDY AND EXPERIMENTAL IDENTIFICATION<br>OF ELASTIC-MAGNETIC VIBRATION ISOLATION SYSTEM .....                                       | 33   |

|   |  |    |
|---|--|----|
| 3.1   | Introduction.....  | 33 |
| 3.2   | System Design .....  | 36 |
| 3.3   | Manufacturing and Assembly.....  | 39 |
| 3.4   | Theory and Model.....  | 40 |
| 3.5   | Experimental Apparatus for Characterization Tests.....                     | 44 |
| 3.6   | Results and Discussion .....   | 46 |
| CHAPTER 4 A DUAL PURPOSE VIBRATION ISOLATOR ENERGY HARVESTER: EXPERIMENT AND MODEL..... |  | 59 |
| 4.1   | Introduction.....  | 59 |
| 4.2   | Modeling.....  | 64 |
| 4.2.1   | Modeling Displacement Transmissibility Using Harmonic Balance Method ..... | 65 |
| 4.2.2   | Model Estimation of Induced Voltage and Harvested Power.....               | 67 |
| 4.3   | Experiment and Model Validation.....                                       | 68 |
| 4.3.1   | Magnetic Restoring Force.....  | 70 |
| 4.3.2   | Mechanical Spring Restoring Force.....                                     | 75 |
| 4.3.3   | Vibration Isolation and Energy Harvesting .....                            | 77 |
| 4.4   | Model Simulation and Parametric Study .....                                | 82 |
| CHAPTER 5 CONCLUSIONS .....   |  | 89 |
| APPENDIX A NOMENCLATURE .....   |  | 91 |
| Bibliography .....  |  | 95 |

## LIST OF FIGURES

|   |    |
|---|----|
| <b>Figure 1.</b> Representative schematic of described nonlinear-stiffness nonlinear-damping vibration isolation system .....   | 16 |
| <b>Figure 2.</b> Dynamic model of the vibration isolation system in response to harmonic base-excitation .....  | 17 |
| <b>Figure 3.</b> Non-dimensional total stiffness, $K$ of vibration isolation design versus non-dimensional displacement $\chi$ . (a) Effect of $\alpha$ ( $\beta, \sigma = 0$ ) (b) Effect of $\beta$ ( $\alpha, \sigma = 0$ ) (c) Effect of $\sigma$ ( $\alpha, \beta = 0$ ) (d) Effect of $\sigma$ with $\alpha, \beta = 0.5$ . .....                 | 19 |
| <b>Figure 4.</b> Deviation of Taylor series expansion from exact solution of non-dimensional total force ( $F_t$ & $F_{t,a}$ ). .....   | 22 |
| <b>Figure 5.</b> Nonlinearity, $\Lambda$ of described nonlinear-stiffness nonlinear-damping vibration isolation design. (a) Effect of $\alpha$ . ( $\beta = \gamma = 0$ ) (b) Effect of $\beta$ . ( $\alpha = 1e-6, \gamma = 0$ ) (c) Effect of $\gamma$ . ( $\alpha = 1e-6, \beta = 0$ ) and (d) Effect of $\gamma$ . ( $\alpha, \beta = 0.5$ ). ..... | 23 |
| <b>Figure 6.</b> Displacement transmissibility ( $\eta$ ) of examined nonlinear-stiffness nonlinear-damping vibration isolation system compared to linear vibration isolation system. ....  | 27 |
| <b>Figure 7.</b> Effect of nonlinear damping ratio, $\xi_3$ , on displacement transmissibility, $\eta$ , ( $\xi_1 = 0.1$ ). .....   | 28 |
| <b>Figure 8.</b> Comparison of four different vibration isolation designs: Linear system (A). Nonlinear-stiffness due to oblique springs and magnetic spring and nonlinear-damping (B). Nonlinear-stiffness due to magnetic spring and nonlinear-damping (C). Nonlinear stiffness due to oblique springs with nonlinear damping.....                    | 30 |
| <b>Figure 9.</b> Displacement transmissibility ( $\eta$ ) versus non-dimensional frequency ( $\Omega$ ), for Design A, B, C, and D. ( $\xi_1 = 0.1, \xi_3 = 1$ ). .....   | 31 |
| <b>Figure 10.</b> Displacement transmissibility ( $\eta$ ) of proposed nonlinear-stiffness nonlinear-damping Design B compared to standard QZS and linear vibration isolation systems, versus non-dimensional frequency sweeping ( $\Omega$ ). .....  | 32 |
| <b>Figure 11.</b> Cartoon schematic of the elastic-magnetic vibration isolator design: Exploded view (Left) and 3D sectional view (Right). .....  | 37 |

|  |    |
|--|----|
| <b>Figure 12.</b> Working principle of the vibration isolator: Initial static position (Left) and dynamic operation (Right). .....   | 38 |
| <b>Figure 13.</b> The fully assembled vibration isolator enclosed within 3D printed housing.....   | 40 |
| <b>Figure 14.</b> Free-body diagram of the single DOF vibration isolator subject to base excitation.....   | 43 |
| <b>Figure 15.</b> Lab experiment setup used to measure restoring forces of the magnetic and mechanical springs. ....   | 45 |
| <b>Figure 16.</b> Lab experiment setup used for measuring displacement transmissibility of the vibration isolator. ....  | 46 |
| <b>Figure 17.</b> COMSOL simulation of magnets interaction in the vibration isolator: The oscillatory motion of the floating solid magnet as it moves between the two fixed top and bottom ring magnets (Left). Cartoon schematic of the magnets arrangement, dimensions, and geometries (Right). ....           | 47 |
| <b>Figure 18.</b> COMSOL simulated flux density of the floating magnet inside the vibration isolator. ....   | 49 |
| <b>Figure 19.</b> Measured and COMSOL simulated nonlinear magnetic restoring force versus displacement. The nonlinear magnetic force is fit to a third order polynomial of the form $Km1\chi + Km3\chi^3$ .....  | 50 |
| <b>Figure 20.</b> 3D geometry and main components of the mechanical spiral spring used in the vibration isolator. ....   | 51 |
| <b>Figure 21.</b> Measured and COMSOL simulated mechanical spring restoring force versus displacement. The linear mechanical spring restoring force is fit to $Kss\chi$ .....  | 52 |
| <b>Figure 22.</b> COMSOL simulation of the mechanical spiral spring behavior in response to 4 [N] payload: Von Mises stresses (Left) and corresponding displacement (Right). ....  | 53 |
| <b>Figure 23.</b> Measured and model simulation of displacement transmissibility of the vibration isolator versus frequency at acceleration level of 1.0g [ $m\ s^{-2}$ ]. Model simulations are performed using Harmonic Balance Method (HBM) and 4 <sup>th</sup> order Runge-Kutta (RK) numerical method.....  | 55 |
| <b>Figure 24.</b> Measured and model simulation of displacement transmissibility of the vibration isolator versus frequency at acceleration level of 0.25g [ $m\ s^{-2}$ ]. Model simulations are performed using Harmonic Balance Method (HBM) and 4 <sup>th</sup> order Runge-Kutta (RK) numerical method..... | 57 |
| <b>Figure 25.</b> Overall design of the dual purpose vibration isolator energy harvester. ....   | 63 |

|  |    |
|--|----|
| <b>Figure 26.</b> Model schematic of the single DOF dual-purpose vibration isolator energy harvester. ....   | 65 |
| <b>Figure 27.</b> Main parts of the dual-purpose device: a) Top part (Left) and b) Bottom part (Right). ....   | 68 |
| <b>Figure 28.</b> Fully assembled dual-purpose vibration isolator energy harvester device. ....  | 70 |
| <b>Figure 29.</b> Schematic of experimental apparatus used for characterization of mechanical and magnetic springs. ....   | 71 |
| <b>Figure 30.</b> COMSOL model of the three magnets arrangement: a) The Levitated solid magnet sweeping between the two stationary top and bottom ring magnets (Left) and b) Three magnets arrangement, dimensions, and geometries (Right). ....   | 72 |
| <b>Figure 31.</b> COMSOL simulation results of magnetic flux density, $B$ estimated at inner, middle and outer coils. ....   | 73 |
| <b>Figure 32.</b> Load-deflection curve of the magnets arrangement used in dual-purpose device. ....   | 74 |
| <b>Figure 33.</b> 3D cartoon schematic of the mechanical spring design used in this work. ....   | 75 |
| <b>Figure 34.</b> Load-deflection curve of the mechanical spring used in dual-purpose device. ....   | 76 |
| <b>Figure 35.</b> Schematic of experimental apparatus used for dynamic characterization of the dual-purpose device. ....   | 77 |
| <b>Figure 36.</b> Displacement transmissibility of the dual-purpose vibration isolator energy harvester at a) 0.25g [ $m s^{-2}$ ] (TOP) and b) 1g [ $m s^{-2}$ ] (BOTTOM) obtained from experiment and models. ....   | 80 |
| <b>Figure 37.</b> Output voltage from the dual purpose vibration isolator energy harvester at a) 0.25 g [ $m s^{-2}$ ] (TOP) and b) 1 g [ $m s^{-2}$ ] (BOTTOM) obtained from experiment and models. ....  | 81 |
| <b>Figure 38.</b> Electric output power recovered by the dual-purpose vibration isolator energy harvester at a) 0.25g [ $m s^{-2}$ ] (TOP) and b) 1g [ $m s^{-2}$ ] (BOTTOM) obtained from experiment and models. ....   | 82 |
| <b>Figure 39.</b> Effect of linear stiffness coefficient, $K_1$ on device performance: (a) and (c): displacement transmissibility at 0.25g and 1g [ $m/s^2$ ], respectively, (b) and (d): generated power at 0.25g and 1g [ $m/s^2$ ], respectively. Nominal values $R_{Load}=900 \Omega$ , $\xi_1=0.11$ , $K_3=1.368e6 N m^{-3}$ . .... | 84 |
| <b>Figure 40.</b> Effect of nonlinear stiffness coefficient, $K_3$ on device performance: (a) and (c): displacement transmissibility at 0.25g and 1g [ $m/s^2$ ], respectively, (b) and  |    |

(d): generated power at 0.25g and 1g[m/s<sup>2</sup>], respectively. Nominal values  $R_{Load}=900 \Omega$ ,  $\xi_1=0.11$ ,  $K_1=618.6 \text{ N m}^{-1}$ . ..... 85

**Figure 41.** Effect of load resistance,  $R_{Load}$ , on device performance: (a) and (c): displacement transmissibility at 0.25g and 1g [m/s<sup>2</sup>], respectively, (b) and (d): generated power at 0.25g and 1g[m/s<sup>2</sup>], respectively. Nominal values  $\xi_1=0.11$ ,  $K_1=618.6 \text{ N m}^{-1}$ ,  $K_3=1.368\text{e}6 \text{ N m}^{-3}$ . ..... 87

**Figure 42.** Effect of damping,  $\xi_1$  on device performance: (a) and (c): displacement transmissibility at 0.25g and 1g [m/s<sup>2</sup>], respectively, (b) and (d): generated power at 0.25g and 1g[m/s<sup>2</sup>], respectively. Nominal values  $R_{Load}=900 \Omega$ ,  $K_1=618.6 \text{ N m}^{-1}$ ,  $K_3=1.368\text{e}6 \text{ N m}^{-3}$ . ..... 88

## LIST OF TABLES

|  |    |
|--|----|
| <b>Table I.</b> Parameters used in nonlinear vibration isolation model simulation.....                             | 29 |
| <b>Table II.</b> Properties of the assembled vibration isolator prototype.....                                     | 41 |
| <b>Table III.</b> Geometric and material properties of the fabricated dual-purpose device.....                     | 69 |
| <b>Table IV.</b> Summation of sin function coefficients of fitted curve for the magnetic flux density, $B$ . ..... | 73 |
| <b>Table V.</b> Measured stiffness coefficients for the magnetic spring.....                                       | 75 |

## **ACKNOWLEDGMENTS**

I would specially like to express my sincere appreciation to my committee chair, Dr. Hamzeh Bardaweel. Without his guidance, motivation and continuous support, this dissertation would not have been possible. I could not have imagined having a better advisor for my doctoral study. I would like to thank my committee members for their insightful comments and discussions. I also, thanks to all my lab mates for all the fun we have had together.

Last but not least, I would like to express my deepest gratitude to my family. Thanks them for supporting me throughout my life and encouraging me to having confidence in my abilities to go after my wishes.

# **CHAPTER 1**

## **INTRODUCTION**

### **1.1 Description of the problem**

Mechanical vibrations are consequences of natural processes as well as human made structures and equipment. These vibrations are in any forms of continuous or semi-continuous oscillations generated by highway bridges [1], human body motion [2], and moving vehicles [3–6]. However, these vibrations may cause damages to structures or prevent their operations [7]. The severity of damage depends on different factors i.e. intensity of vibration, strength of the structure and vibration duration. To prevent any possible damages, vibration isolation systems are deployed to cancel out the undesired vibrations from traveling through structures and machineries. In a traditional vibration isolation system, elements like spring and damper are designed to prevent oscillation from traveling between the source of vibration and the isolated mass [8]. Although, these unwanted vibrations carry kinetic energy that is taken off from the oscillation source. However, vibration isolation systems turn this energy into wasted heat which conducts away to the environment.

In parallel to progresses in vibration isolation systems, there has been recent advances in electronics industries that employs low-power miniature wireless sensing technologies [9]. As a result, equipment, structures, and machineries are loaded with onboard sensors and gadgets to monitor their health and conditions through measuring

their temperature, pressure, stress, strain, humidity, corrosion, etc [9-12]. Moreover, there is an increasing trend to deploy advanced technology sensors in the future that are integrated into equipment or make a wireless sensor networks for things around us. The serious challenge arises from providing power supply to these sensors. That's where it opens up an opportunity for utilizing vibrations experienced by those structures and machineries as a power source to operate the onboard sensors. The energy recovered from vibration sources is free, abundant and can be converted into electric energy to replace or extend the life time of traditional batteries for the usage of onboard sensors and gadgets [13, 14]. Therefore, the presented dissertation is focused on developing a dual-purpose vibration isolation energy harvesting system. This system is supposed to act as vibration isolator and energy scavenging system at the same time. Thus, the main purpose of the dual-purpose device is preventing vibrations from traveling through the isolated mass. Also as a secondary task, it converts some of the energy contained in these oscillations into useful electric charge instead of wasted heat.

## 1.2 Objective of the work

The traditional vibration isolation systems terminate the undesired oscillation at the cost of converting vibration kinetic energy into waste heat. These systems are single-functional and are not capable to scavenge usable power from the environment. Besides, the traditional vibration isolators suffer from fatigue and failure in their components as they mostly utilize mechanical apparatus in their design. The main objective of present dissertation is building a dual-purpose vibration isolation energy harvesting system capable of preventing vibrations from traveling (as its primary function) and then convert

these vibrations into useful electric charge (its secondary function). To achieve to this goal, these sub-objectives were taken:

- Design a dual function vibration isolation energy harvesting system: The basic operation of the device depends on applying magnetic spring components to isolate the payload mass and induce current in the wrapped coil around the device. The faster response to the exerted forces, longer expected life, less chances of failure and more smooth operation compared to traditional mechanical spring caused to use magnetic apparatus in the design. Then the body of the device sketched including all the parts with complete details. In this step, different sketches and assemblies were considered and the best configuration was selected.
- Fabricate the dual function vibration isolation energy harvesting system: The device was manufactured using a rapid prototyping technique. The 3D sketch of the design converted into readable format by a fused deposition modeling 3D printer. Upon assembly of all the parts after printing, other apparatus i.e. magnets, coil and mount were fixed in their positions to get the device ready for experimental test.
- Experimental characterization of the dual function vibration isolation energy harvesting system: Prior to run any experimental test, the full characterization of the device was performed. This characterization includes measuring restoring force of the magnets, damping coefficient and resonant frequency of the device. Then the experimental tests on the shaker table was accomplished. During the vibration test, transmissibility of the system, generated power and voltage were measured to validate the results later obtained from modelling.

- Modeling of the dual function vibration isolation energy harvesting system: In the modeling of the system, a single degree of freedom vibration system with nonlinear stiffness component and harmonic vibration input was considered. The transmissibility characterization calculated based on both numerical and analytical approaches. Also, the simulation on magnetic flux density at the location of the coil was performed which was used to model the generated power and voltage of the device. Finally, the results from modeling compared to those of experimental run in order to make sure about the validity of the model.

### 1.3 State of the art

Recently, there has been growing interest in using dual purpose devices that are able to eliminate undesired vibration and scavenging energy from the vibration source at the same time. Li et al. [15] experimentally tested a 3D printed metamaterial dual purpose device. The design was consisted of a square array of free-standing piezoelectric cantilevers to simultaneously harvest energy and isolate undesired vibrations. They operated the system within the bandgap to scavenge the vibration energy. The results demonstrated that the 3D printed metamaterial is able to suppress the wave propagation within the stop band of 146-171 Hz while converts the kinetic energy into electric power through piezoelectric elements. The maximum obtained voltage and power was reported as 0.22 V and 0.05  $\mu$ W respectively. Hu et al. presented an analytical model of a vibration isolation energy harvesting acoustic-elastic metamaterial structure [16]. In the proposed design, the metamaterial structure was integrated with piezoelectric energy-harvesting components. The prototype was investigated in both unit-cell and multi-cell configurations with two degree of freedom. Each unit cell is modeled as an outer sphere

with mass  $m_1$  connected to an inner ball with mass  $m_2$ , including damper and springs with coefficients of  $c_1$  and  $k_1$  connected to the outer mass and  $c_2$  and  $k_2$  for the inner mass respectively. They demonstrated that a double valley-phenomenon results in a band gap that can alter the resonant frequency of the system and make the band gap wider. The authors also performed a dimensionless parametric study to optimize the performance of their model. They concluded that there is a tradeoff in optimization of the device where the effect of studied parameters is in opposite direction for suppressing the vibration or scavenging the energy.

Davis and McDowell proposed a passive vibration isolation device that harvests energy using post-buckled beam and piezoelectric elements [17]. The buckled beam behaved as nonlinear stiffness spring to lower the resonant frequency while there was less static deflection. Approximately,  $0.36 \mu\text{W}$  electric power was harvested at 2% transmissibility. Their results demonstrated that there is not necessary tradeoff between vibration isolation and energy harvesting. Li et al. [18] proposed an energy harvesting shock damper system to attenuate vibrations transferred from vehicle-road interaction while simultaneously generates electrical power. This study used a mechanical motion rectifier rather than an electrical rectifier to generate DC current. The experimental data showed over 60% efficiency of the system at high frequency in shock absorption which is higher than its traditional models. Also, it was able to generate 15.4 W at 15 mph on a smooth paved road condition. Similarly, Ali and Adhikari [19] theoretically studied the performance of a vibration absorber device supplemented with a piezoelectric stack for power recovery. A closed form formula for optimal frequency ratio based on fixed-point theory was proposed. Then, it was proved that there is a relationship between electrical

parameters in the model that minimizes the structure vibration. Their study showed that the energy harvester module introduced an additional damping into the system.

Madhav and Ali [20] worked on the feasibility of integrating vibration absorber with piezoelectric stack for power generation under stationary Gaussian white noise excitations. They used probabilistic linear random vibration theory to solve the model. The authors concluded that the recovered energy can be increased when the mass of the structure increases. So, the generated power from large structures like bridges is enough to power the sensors that are installed on them. Tang et al. [21] worked on the recovery of vibration energy from tall buildings using active tuned mass dampers and electromagnetic harvesters. The control unit of the energy harvesting circuit was able to switch between three different modes as semi-active, self-powered active and passive-matching configurations. The experiments were run on a three story prototype building leading to 60 mW power generation at 3.3 Hz when the system was excited by a harmonic force of 15 N. They concluded that the semi-active and self-power active control system outperform in attenuating the vibration compare to the passive one.

Buelga et al. [5] both analytically and experimentally investigated the concept of energy recovery from a tuned mass damper system using an electromagnetic transducer. They used adaptive and semi-active control system and concluded the better performance of the semi-active controller compare to the adaptive control system. The harvested energy above 50 mW for both semi-active and adaptive controllers was reported while the performance for semi-active was 8% and the adaptive controller reached to 3% performance. The maximum power available to harvest for adaptive control system was about 0.45 W. The authors concluded that the performance of vibration isolation energy

harvester will be enhanced if the coil resistance and parasitic damping of the device reduces.

It also showed that the transmissibility's peak was reduced in a system with both magnetic and spiral flexural springs compare to a system with only magnetic negative stiffness spring. Moreover, a dual-purpose device was developed to isolate micro vibrations and harvest energy from micro-jitters of a cooler during satellite on-orbit operation [1, 7]. To demonstrate the feasibility of these dual functioning devices, the authors used a tuned mass damper integrated with electromagnetic elements to isolate the vibration and scavenge the energy at the same time. The dual-purpose device was able to isolate the primary jitter level of the cooler by a factor of 10.8 and recovered  $5.84 \mu\text{W}$  of vibration energy into electric energy.

Monaco et al. [22] worked on a semi-active controller and introduced time-dependent damper to improve the performance of the device. An optimization technique was utilized as a function of the excitation frequency and the numerical and analytical results compared together. The analytical results showed that the average power of the presented device at 50 Hz was 0.180 mW, compare to 0.11 mW for that of passive system. Also, the average harvested energy at 80 Hz for passive and time-varying damper was respectively 0.495 and 0.769 mW. However, the transmissibility of the device is above one at 80 Hz and it does not behave as a vibration isolator anymore. Chitba et al. [23] proposed a flexible structure with piezoelectric elements and absorbers for isolation and harvesting energy simultaneously. They used a numerical approach, Galerkin procedure, to optimize the design in which the aim was defined to minimize the total energy of the uncontrolled structure. A set of factors as stiffness, mass, load resistance

and damping coefficient were used with initial values and a code was developed to update these parameters to minimize the total energy in the structure. They concluded that their design is able to confine undesired vibration and harvest electrical power at the same time. In another study, a hydraulic electromagnetic shock absorber was studied by Fang et al. [24]. The device was tested under a sinusoidal excitation with 10 Hz frequency and 3 mm peak amplitude. The recovered energy under these conditions was about 200 W within 16.6% efficiency of the device. However, they analytically proved that the energy loss will be decrease when the inner diameter of pipelines increases. During the test, the average of rotational speed of the motor was 1100 rev/min with working volume of hydraulic of 5.5 cc/rev. Also, they claimed that the energy regenerative characteristic of the device depends on the pressure drop on check valve of the hydraulic rectifier. Ding et al. [25] proposed a hybrid electromagnetic suspension with modified skyhook control that was able to regenerate energy and isolate the vibration. The proposed device had two working forms as passive and active control modes. The effect of damping on both vibration isolation and energy harvesting was discussed. The simulation results showed that the vibration isolation in the hybrid electromagnetic suspension has improved by 22.2% compared to that of only passive suspension. The authors used body acceleration and the taken energy indexes to evaluate the vibration isolation and energy regeneration of the system. The instantaneous energy of the system for a device with  $1.82 \text{ m/s}^2$  body acceleration was 1185 J at frequency range 0.5-8 Hz. Pei et al. [26] studied multi-resonant electromagnetic shunts for vibration isolation energy harvesting system. They compared multi-mode resonant shunt with single resonant shunt circuit to show the effectiveness of their design. The authors run a

numerical study on a case study including a base-isolated building with primary mass of 1315417 kg and base mass of 789250 kg. The time period of the fixed-base building supposed to 0.85 s and the building was exposed to two forms of earthquake within frequency range 0-3 Hz. Two earthquake forms considered as the Northridge earthquake which occurred in 1994 in Reseda, California with peak amplitude of 0.6 g, and the second form was Kobe earthquake which occurred in 1995 in Japan with ground acceleration with peak amplitude of 0.8 g. Under Northridge earthquake loads, the total average power obtained during the earthquake was 203.37 Kilowatts. However, under Kobe earthquake, the total average harvested power was 101.26 Kilowatts. The time history response of the isolated base under Northridge and Kobe earthquake showed that the peak of relative displacements of the building were around 0.15 m and 0.08 m respectively. The authors run the experiments under scaled Northridge and Kobe earthquakes and showed that the design can effectively suppress the vibration and reduce the displacement peak value by 31.72% and 72.81% for single and multi-mode shunt circuits respectively. The generated voltage in experiments was 30 mV and 18 mV under scaled Northridge and Kobe earthquake models respectively. Kan et al. [27] theoretically and experimentally worked on a piezohydraulic vibration isolator that was able to harvest the energy as well. They discussed on the advantages of the design including ability to reduce/tune the resonant frequency and improvement of the output power. A fabricated prototype experimentally tested and it was showed that the maximal voltage and bandwidth can be tuned with changing the backpressure and proof mass. The minimal optimal frequency of 13 Hz with the relative voltage of 81.6 V at 0.2 MPa and 10 Kg proof mass was reported. Huang et al. [28] discussed on development and optimal design

of an energy regenerative suspension system. The optimal design was aimed to determine the damping and stiffness coefficients for optimum performance with comfort riding and energy harvesting metrics. They considered the actual road roughness regulations and applied a low power switch mode rectifier circuit to vary the damping coefficient in the real-time mode to adapt to the optimum performance. The experiment performed on a 1-DOF quarter-car prototype, a DC motor and a ground ball screw utilized to convert the vertical movement to the rotary motion. The authors demonstrated that the system's response under highway driving condition with optimal damping coefficient can lead to absolute peak acceleration of  $20\text{m/s}^2$  with approximately maximum generated power of 10 W. In another study, a semi-active vibration isolator with magnetorheological damper was utilized by Sapinski [29]. In this work, the harvested energy from structural vibration is used to control the damping coefficient of the system. The experimental results compared to a passive system, when magnetorheological (MR) damper was off-state, and also a system with external power supply. The tests demonstrated that the regenerative energy can supply the required power for a MR damper. The testing machine run with a sine displacement excitation of amplitude 6 mm and frequency range 0.5-6.5 Hz. The resonant frequency of the system was 5 Hz in which a significant vibration reduction was reported in the nearby of the resonant frequency compared to the passive configuration.

#### 1.4 Structure of dissertation

In the following chapters, in chapter 2 a nonlinear stiffness- nonlinear damping system is analyzed analytically. In chapter 3, a vibration isolator system with elastic and

magnetic stiffness components is studied. In chapter 4, a vibration isolator energy harvester device is investigated numerically and experimentally.

## **CHAPTER 2**

### **DISPLACEMENT TRANSMISSIBILITY EVALUATION OF VIBRATION ISOLATION SYSTEM EMPLOYING NONLINEAR DAMPING AND NONLINEAR STIFFNESS ELEMENTS**

The current chapter discusses on a vibration isolation system with both nonlinear damping and nonlinear stiffness elements. The author has used parts of the current chapter in the research article, “Displacement Transmissibility Evaluation of Vibration Isolation System Employing Nonlinear-Damping and Nonlinear-Stiffness Elements “by S. M. Mahdi Mofidian and H. Bardaweel, published in Journal of Vibration and Control, Volume 24, issue 18 (2018) which is adapted with permission from SAGE.

#### **2.1 Introduction**

Unwanted oscillations commonly encountered in engineering practice can be harmful and problematic. For example, undesirable vibrations produced by mechanical systems inside spacecraft may persist for an extended duration in a micro-gravity environment [30]. These small oscillations may deteriorate the working environment of onboard instruments, and prevent astronauts from reading instrument panels and operating switches precisely due to blurry vision [2]. Vibration isolation systems are used to attenuate unwanted vibrations. Examples of vibration isolation systems include shock absorbers used for vehicle ride comfort [31-33]. In its simplest form, a vibration isolation system is made of flexible supporting mechanism, i.e. linear spring, and an

energy dissipation mechanism, i.e. damper, connected to the isolated mass. The kinetic energy carried by vibrations is converted into heat before it is dissipated through the damper. Nonetheless, a linear vibration isolation system is most effective over narrow frequency bandwidth and when the excitation frequency is well above its natural frequency [34]. However, unwanted oscillations commonly encountered in engineering practice are made of wideband low frequency spectrum. This includes shocks and random and chaotic excitations transmitted to structures and machinery including spacecraft, buildings, bridges, and automobiles [34]. For a fixed mass, a vibration isolation system with soft spring suffers from undesired large static deflections. As a result, nonlinear approaches [35-38] including nonlinear damping [39-45], nonlinear stiffness [38, 46-49], and geometric nonlinearities [50-52] have been investigated to overcome the major design constraints facing linear isolation systems. The nonlinear design of a vibration isolation system offers few advantages over a linear design [34]. A nonlinear design has the promise to attenuate unwanted oscillations at lower and wider frequency band.

Several studies have investigated nonlinear approaches towards vibration isolation using both numerical and experimental techniques. Reviewing the massive literature on this subject is beyond the scope of this article. Nonetheless, Liu, C et al. [30] and Ibrahim, R [34] provide a thorough and detailed review of the subject. For instance, researchers have investigated the effect of nonlinear cubic viscous damping on vibration isolation systems [39, 40, 42, 43]. Jing et al. studied the effect of a simple nonlinear damping element on the performance of a vibration isolation system subject to periodic excitation [40]. Jing and Lang [41] performed a theoretical study on effects of cubic

nonlinear damping on a vibration isolation system with linear stiffness element using a dimensionless model subject to a harmonic excitation. Results show that the cubic nonlinear damping element has little effect on the response of vibration isolation system away from resonant frequency. Frequency domain analysis [40] and transmissibility of a nonlinear damping element [44-45] in a vibration isolation system with linear stiffness have been also investigated.

Another nonlinear approach is a design that combines positive stiffness and negative stiffness elements and known as the quasi-zero-stiffness (QZS) vibration isolation system. QZS is considered as a promising approach towards nonlinear design of vibration isolation systems [53-55]. The QZS design is characterized by its ability to support large static loads due to its high static stiffness, while simultaneously maintaining small dynamic stiffness [46, 57]. Consequently, the QZS offers lower resonant frequency and wider frequency bandwidth compared to a linear design. QZS vibration isolation systems using vertical springs connected to horizontal oblique springs [30, 55, 56], extreme geometric nonlinearities [50-52], and magnets [30, 46-49] have been proposed and investigated. For example, a bio-inspired limb-like nonlinear vibration isolation system has been proposed and modeled by Wu and Jing [58]. In their analysis, the legs of *grus japonensis* were modeled as a single-degree-of-freedom vibration isolation system with stiffness nonlinearities. Results showed beneficial stiffness nonlinearities providing quasi-zero stiffness. Sun and Jing proposed a three-dimensional symmetrically scissor-like QZS isolation system employing both stiffness and damping nonlinearities [35]. Their theoretical analysis and comparative study demonstrated improved vibration isolation characteristics in multi-direction due to geometric nonlinearities. Nonetheless,

these standard QZS designs face challenges including frequency jump phenomenon induced as a result of stiffness nonlinearities introduced into the system and instability induced as a result of negative stiffness [35].

Considering the advantages of the QZS vibration isolation system, in this work a cubic nonlinear damping element in the presence of a nonlinear magnetic spring (with positive stiffness) and oblique mechanical springs (with geometric nonlinear negative stiffness) in a QZS vibration isolation system is theoretically investigated. A system with similar structure may be used in active/semi-active vibration isolation or multi-function energy harvesting [5, 17, 19] where the oscillating magnet mass can be used to generate useful electric charge. The generated electric charge may be stored in batteries or used to, actively, adjust damping properties of the isolation system. To the best knowledge of authors, only the effect of linear viscous damping in presence of a nonlinear stiffness element in QZS design has been investigated [35, 38]. Although the intentionally introduced damping nonlinearities add to the complexity of the analysis of the vibration isolation system [41] it may have major effects on the performance of a standard QZS vibration isolation system. In this work, we theoretically investigate a design based on a QZS system with nonlinear stiffness elements combined with a nonlinear damping element. The Harmonic Balance Method (HBM) is used as the mathematical technique to solve the governing dynamic equation of the system. Results from HBM are compared to those obtained from numerical techniques. Moreover, the results from this study are compared against standard vibration isolation systems.

## 2.2 System description and structure

Here we consider a representative design of a vibration isolation system shown in Figure 1. A total mass,  $m$ , made of isolated object and levitated magnet mass is vertically aligned using mechanical springs,  $n$ , with linear stiffness,  $nk_s$ , from wall sides. The levitated magnet is positioned between bottom and top (optional) stationary magnets as shown in Figure 1. The repulsive magnetic force developed between matching poles of levitated and fixed magnets is described with a nonlinear magnetic springs,  $k_{m1}$  &  $k_{m3}$  [59-61]. Figure 2 shows model schematic of the described system. Nonlinear viscous damping of  $n$ th power has been demonstrated and achieved using few techniques reported in literature [62, 63] including fluid flow through an orifice [64] and magnetorheological fluid flow [65-67].

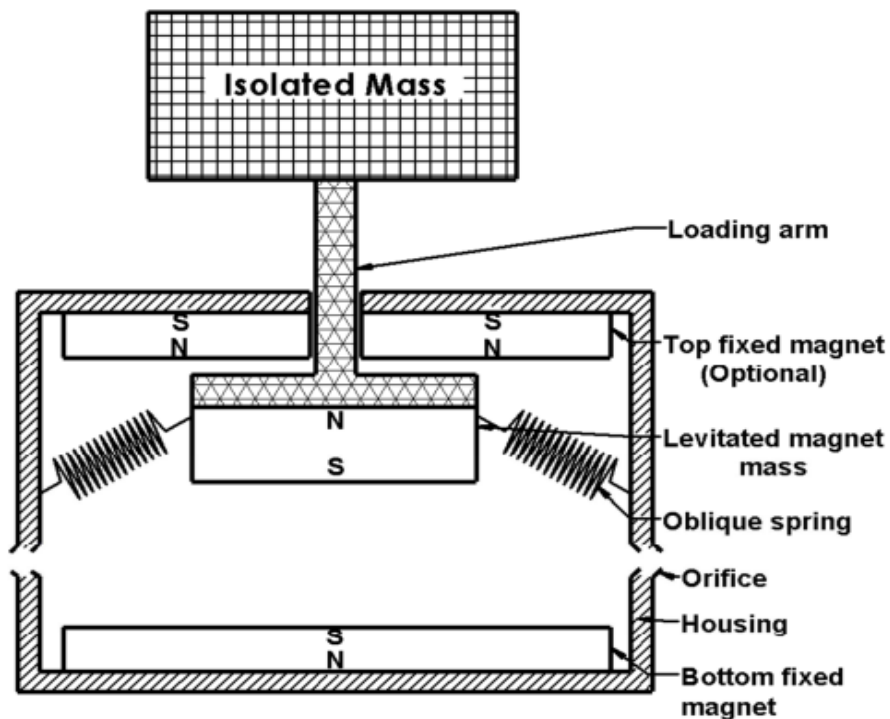


**Figure 1.** Representative schematic of described nonlinear-stiffness nonlinear-damping vibration isolation system

For the sake of general analysis in this article, the small orifices shown in Figure 1, presumably, introduce  $n^{\text{th}}$  power nonlinear viscous air damping into the system described using  $C_1$  and  $C_3$ , respectively. Additional forms of damping such as coulomb dry-friction damping [3, 68] and electric damping [59] may be introduced into the system design. However, these forms are left for future work and investigation. It should be noted that the goal of this work is not to model a specific vibration isolation device or to examine different forms of damping present in a particular vibration isolation device.

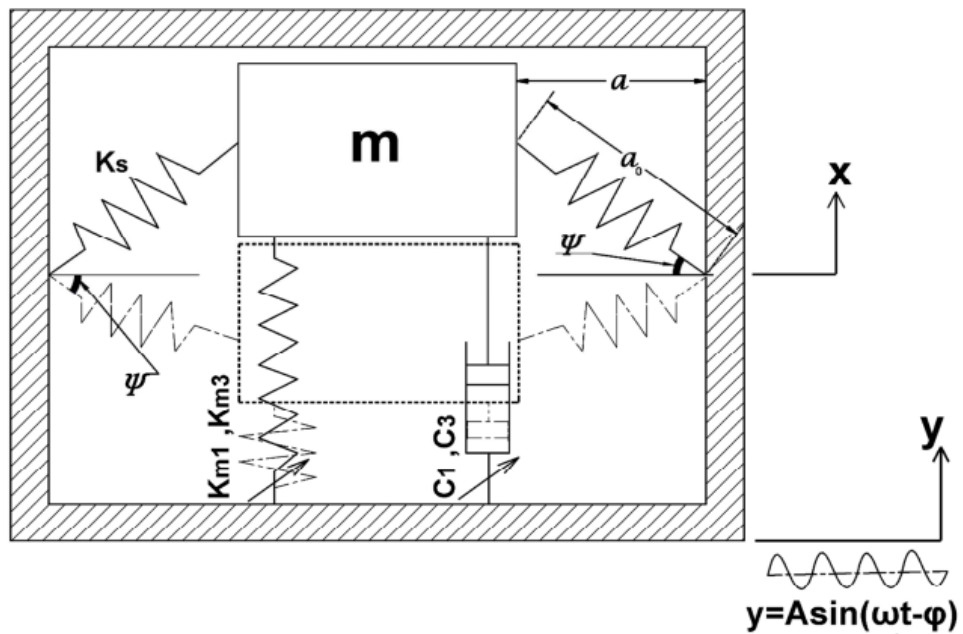


**Figure 2.** Dynamic model of the vibration isolation system in response to harmonic base-excitation

The main goal of this work is to design and analyze a vibration isolation system employing cubic nonlinear viscous damping in presence of nonlinear stiffness element, and investigate their effect on performance of the vibration isolation system.

### 2.3 Static characterization of a system with “n” oblique springs

The unique arrangement of the levitated magnet and the oblique springs, shown in Figure 1, produces desirable stiffness nonlinearities in the system [69]. In addition to the positive nonlinear stiffness introduced by the magnetic spring, the oblique mechanical springs produce geometric nonlinearity and negative stiffness [69]. For static condition, i.e.  $y=0$ , the force of a single oblique mechanical spring along its axis is given by

$$\mathcal{F}_s = k_s \left( \sqrt{\chi^2 + a^2} - a_0 \right) \quad \text{Eq. (1)}$$

The nomenclature of the letters and symbols is described in Appendix A. The total oblique mechanical springs forces in vertical direction is given by

$$F_s = n\mathcal{F}_s \sin \psi = nk_s(\sqrt{\chi^2 + a^2} - a_0) \sin \psi \quad \text{Eq. (2)}$$

where  $\sin \psi = \frac{\chi}{\sqrt{\chi^2 + a^2}}$ . Further simplification yields

$$F_s = nk_s \left( 1 - \frac{a_0}{\sqrt{\chi^2 + a^2}} \right) \chi \quad \text{Eq. (3)}$$

The magnetic spring force is estimated numerically [70,71] and fit to  $n^{\text{th}}$  order polynomial [60,72] of the form:

$$F_{mag} = k_{m1}\chi + k_{m3}\chi^3 \quad \text{Eq. (4)}$$

Using equations (3-4) the total restoring force in vertical direction is given by

$$F_t = nk_s \left( 1 - \frac{a_0}{\sqrt{\chi^2 + a^2}} \right) \chi + k_{m1}\chi + k_{m3}\chi^3 \quad \text{Eq. (5)}$$

Introducing non-dimensional parameters  $\alpha = \frac{k_{m1}}{nk_s}$ ,  $\beta = \frac{k_{m3}a_0^2}{nk_s}$ ,  $\bar{\chi} = \frac{\chi}{a_0}$  &  $\sigma = \frac{a}{a_0}$  and rewriting (5) in non-dimensional form yields

$$\bar{F}_t = \frac{F_t}{nk_s a_0} = \left(1 - \frac{1}{\sqrt{\bar{\chi}^2 + \sigma^2}} + \alpha\right) \bar{\chi} + \beta \bar{\chi}^3 \quad \text{Eq. (6)}$$

In addition, non-dimensional total stiffness,  $\bar{K}$  is defined as

$$\bar{K} = \frac{d\bar{F}_t}{d\bar{\chi}} = 1 - \frac{\sigma^2}{(\bar{\chi}^2 + \sigma^2)^{3/2}} + \alpha + 3\beta \bar{\chi}^2 \quad \text{Eq. (7)}$$

**Figure 3** shows non-dimensional overall stiffness,  $\bar{K}$ , obtained from (7) for different non-dimensional parameters  $\alpha$ ,  $\beta$ , and  $\sigma$ . The ratio of the two linear stiffness coefficients, i.e.  $k_{m1}$  and  $nk_s$ , respectively, is denoted by  $\alpha$ . The ratio of nonlinear magnetic stiffness,  $k_{m3}$ , to linear spring stiffness,  $nk_s$ , is denoted by  $\beta$ . The initial inclination angle,  $\Psi$ , of the mechanical spring is described using  $\sigma$ .

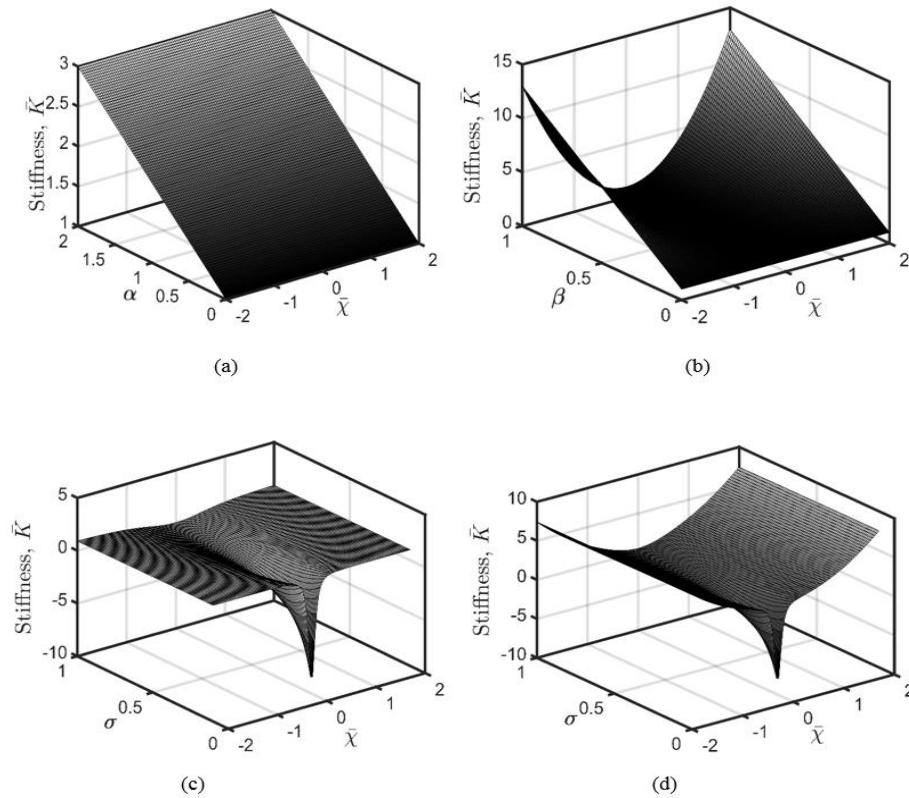


**Figure 3.** Non-dimensional total stiffness,  $\bar{K}$  of vibration isolation design versus non-dimensional displacement  $\bar{\chi}$ . (a) Effect of  $\alpha$  ( $\beta, \sigma = 0$ ) (b) Effect of  $\beta$  ( $\alpha, \sigma = 0$ ) (c) Effect of  $\sigma$  ( $\alpha, \beta = 0$ ) (d) Effect of  $\sigma$  with  $\alpha, \beta = 0.5$ .

**Figure 3** shows the effect of each parameter and its contribution to the overall stiffness of the vibration isolation system. As  $\alpha$  is increased, the overall stiffness increases linearly as shown in Figure 3a. This is expected as a traditional linear spring shows a constant stiffness value along the displacement line,  $\bar{\chi}$ . An increasing nonlinear relationship between the restoring force,  $\bar{F}_t$ , and the displacement,  $\bar{\chi}$ , is observed in (6) as  $\beta$  is increased. This results in an increasing nonlinear stiffness observed in Figure 3b. With  $\alpha$  and  $\beta$  suppressed ( $\alpha, \beta = 0$ ), the system demonstrates a negative stiffness behavior as shown in Figure 3c. The combination of magnetic and oblique, mechanical springs can produce a unique stiffness profile as shown in Figure 3d. The system exhibits a negative stiffness behavior for  $0 < \sigma < 0.5$  for fixed linear and nonlinear stiffness parameters  $\alpha, \beta = 0.5$ . This can be achieved by adjusting the separating distance between the levitated and stationary magnets via screw mechanism until the desired behavior of the system is achieved. A hardening system can be achieved in a similar fashion by tuning the distance between the magnets or by increasing the spring inclination,  $\Psi$ , for  $\sigma > 0.5$ .

#### 2.4 Nonlinearity analysis

**Figure 3** shows the nonlinear characteristics of the total stiffness of the described system. To get further insights into the nonlinearity of the system, a third order Taylor series approximation is used to describe the oblique mechanical spring force,  $F_s$ , in (3) for small displacements,  $\chi$ , and given by

$$F_{s,a} = \sum_{n=0}^{\infty} \frac{F_s^{(n)}(0)\chi^n}{n!} \approx F_s(0) + F_s'(0)\chi + \frac{F_s^{(2)}(0)\chi^2}{2!} + \frac{F_s^{(3)}(0)\chi^3}{3!} \quad \text{Eq. (8)}$$

$$= \frac{nk_s a_o}{2a^3} \chi^3$$

where  $F_{s,a}$  indicates a 3<sup>rd</sup> order approximation using a Taylor series expansion for the restoring force. Further, the non-dimensional total restoring force in the vertical direction described in (6) and (8) becomes

$$\bar{F}_{t,a} = \alpha \bar{\chi} + \left( \frac{1}{2} \gamma^3 + \beta \right) \bar{\chi}^3 \quad \text{Eq. (9)}$$

where  $\bar{F}_{t,a}$  is an approximation of the non-dimensional total restoring force using a Taylor series expansion. The approximate non-dimensional stiffness,  $\bar{K}_a$ , based on the Taylor series expansion becomes

$$\bar{K}_a = \alpha + 3 \left( \frac{1}{2} \gamma^3 + \beta \right) \bar{\chi}^2 \quad \text{Eq. (10)}$$

where  $\gamma = \frac{1}{\sigma}$ . Using the method described by Wu et al. [46] to estimate the stiffness nonlinearity of the described system, the nonlinear component is compared to the linear component of the total stiffness,  $\bar{K}_a$ , described in (10). This results in the nonlinearity,  $\Lambda$ , of the system defined as

$$\Lambda = \left| \frac{3 \left( \frac{1}{2} \gamma^3 + \beta \right) \bar{\chi}^2}{\alpha} \right| \quad \text{Eq. (11)}$$

**Figure 4** evaluates the deviation of the Taylor series approximation compared to exact calculations of total stiffness and total restoring force of the described system, respectively. **Figure 4** shows non-dimensional total spring force,  $\bar{F}_t$  &  $\bar{F}_{t,a}$ , versus non-dimensional displacement,  $\bar{\chi}$ , calculated using (6) and (9), respectively. Figure 4 reveals that for small displacements,  $\bar{\chi}$ , the Taylor series approximation is comparable to the exact solutions. However, deviation between approximate and exact force appears at higher displacements,  $\bar{\chi}$ . This is expected since Taylor series expansion was performed

near  $\bar{\chi} = 0$ . Deviation also increases for smaller values of the ratio  $\frac{\beta}{\gamma^3} = \beta\sigma^3$ . This behavior can be explained in light of set (5-10).

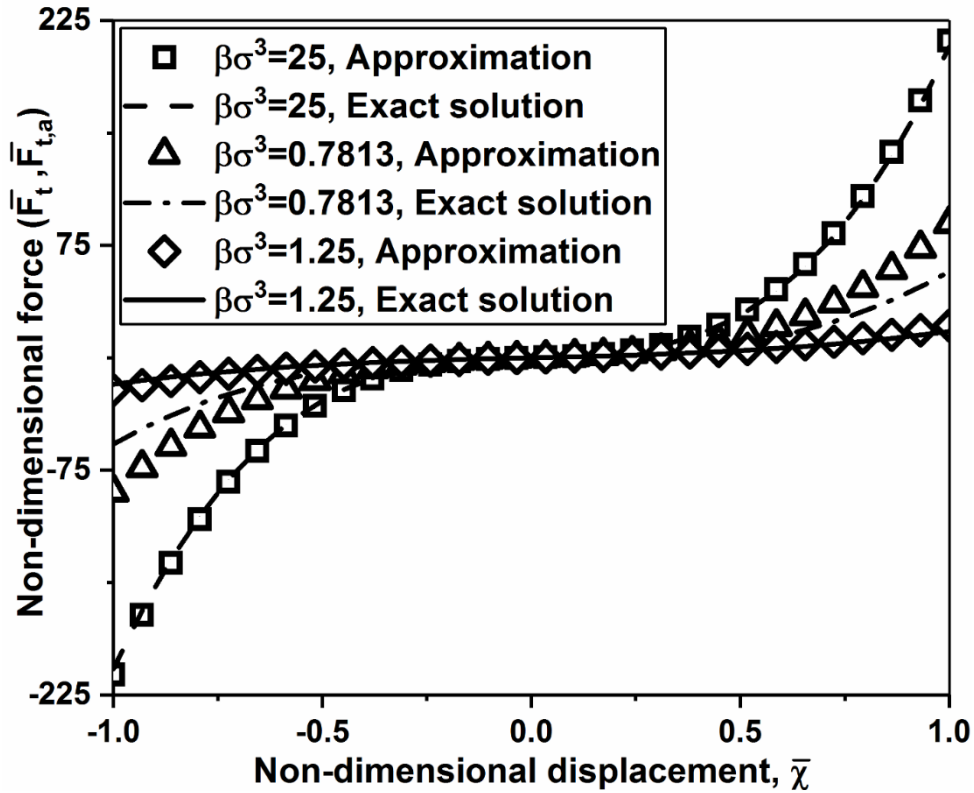


**Figure 4.** Deviation of Taylor series expansion from exact solution of non-dimensional total force ( $\bar{F}_t$  &  $\bar{F}_{t,a}$ ).

The non-dimensional parameter,  $\beta$ , describes the nonlinearity of magnetic spring compared to linear oblique spring stiffness, i.e.  $\beta = \frac{k_{m3}a_0^2}{nk_s}$ . The geometric nonlinearity of the oblique springs is described using the non-dimensional parameter,  $\sigma = \frac{a}{a_0}$ . Thus, as  $\beta$  increases, geometric nonlinearity of oblique springs,  $\sigma^3$ , becomes less significant compared to the magnetic nonlinearity described by  $\beta = \frac{k_{m3}a_0^2}{nk_s}$ . As a result, the contribution of oblique spring approximated force (8) becomes less significant compared

to the total spring force given in (9). The estimated nonlinearity of the system, obtained using (11), is shown in **Figure 5**.

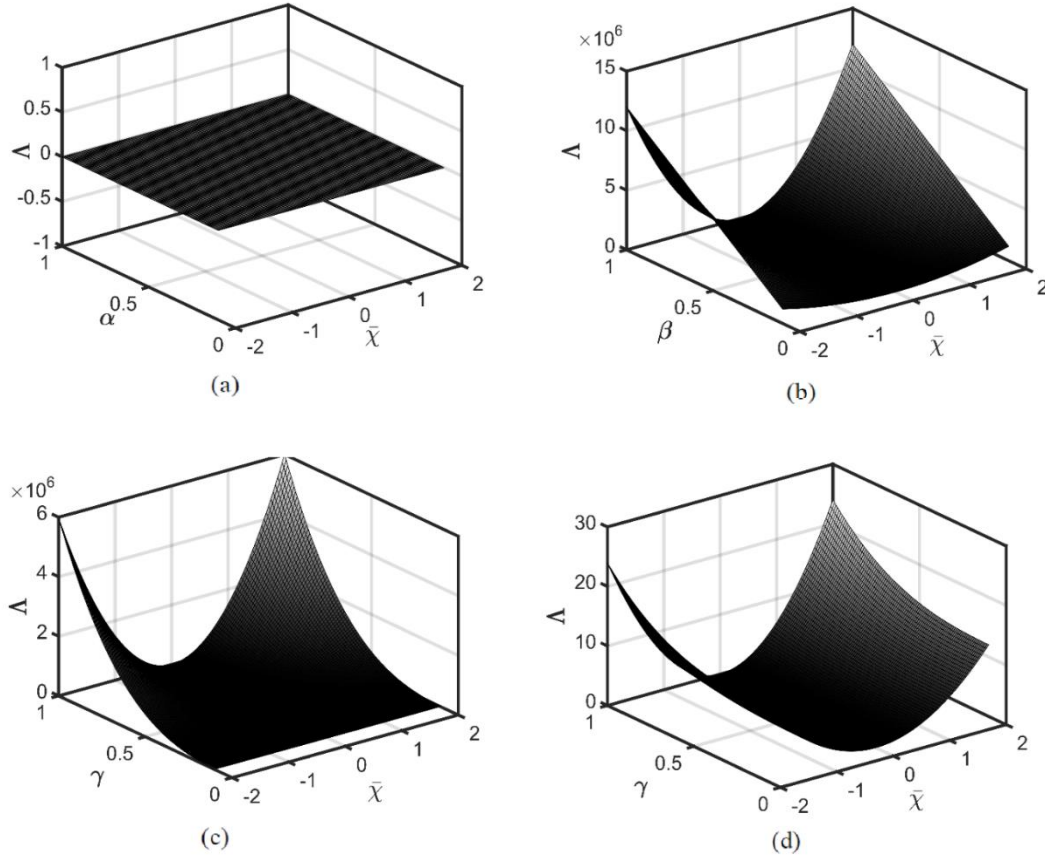


**Figure 5.** Nonlinearity,  $\Delta$  of described nonlinear-stiffness nonlinear-damping vibration isolation design. (a) Effect of  $\alpha$ . ( $\beta = \gamma = 0$ ) (b) Effect of  $\beta$ . ( $\alpha = 1e^{-6}, \gamma = 0$ ) (c) Effect of  $\gamma$ . ( $\alpha = 1e^{-6}, \beta = 0$ ) and (d) Effect of  $\gamma$ . ( $\alpha, \beta = 0.5$ ).

The effect of magnetic spring non-dimensional parameters,  $\alpha$  and  $\beta$ , is shown in Figure 5 a-b. The linear stiffness parameter,  $\alpha$ , has no effect on the nonlinearity of the system, while larger non-dimensional parameter,  $\beta = \frac{k_{m3}a_0^2}{nk_s}$ , increases the overall nonlinearity of the system. This is because a larger  $\beta$  manifests the effect of nonlinear stiffness of the magnetic springs,  $k_{m3}$ . The effect of oblique mechanical springs on total nonlinearity of the system is shown in Figure 5c. Figure 5c shows that the nonlinearity

improves for larger  $\gamma$ , corresponding to oblique springs inclination in the range  $0 < \sigma < 1$ . Thus, a combination of mechanical oblique springs and magnetic springs, shown in Figure 5d, enhances the total nonlinearity of the system compared to their individual counterparts.

## 2.5 Dynamic and non-dimensional analysis

**Figure 2** shows the dynamic model of the vibration isolation system for base excitation,  $y$ . Upon harmonic base excitation  $y = A \sin(\omega t - \varphi)$  the total mass,  $m$ , moves with relative displacement,  $\chi = x - y$ , at time,  $t + \Delta t$ . The dynamic behavior of the moving mass,  $m$ , is described using conservation of momentum, i.e. Newton's second law, and given by

$$m\ddot{\chi} + c_1\dot{\chi} + c_3\dot{\chi}^3 + nk_s\chi\left(1 - \frac{a_0}{\sqrt{\chi^2 + a^2}}\right) + k_{m1}\chi + k_{m3}\chi^3 = -m\ddot{y} \quad \text{Eq. (12)}$$

where  $(\blacksquare)$  represents the time derivatives. Rewriting (12) in non-dimensional form for a base excitation with amplitude,  $A$ , and phase,  $\varphi$ , of the form  $y = A \sin(\omega t - \varphi)$  yields

$$\begin{aligned} \bar{\chi}'' + 2\xi_1\bar{\chi}' + 2\xi_3\bar{\chi}'^3 + \frac{1}{\alpha}\left(\alpha + 1 - \frac{1}{\sqrt{\bar{\chi}^2 + \sigma^2}}\right)\bar{\chi} + \frac{\beta}{\alpha}\bar{\chi}^3 \\ = \bar{A}\Omega^2 \sin(\Omega\tau - \varphi) \end{aligned} \quad \text{Eq. (13)}$$

where  $\bar{A} = \frac{A}{a_0}$ ,  $\omega_n = \sqrt{\frac{k_{m1}}{m}}$ ,  $\Omega = \frac{\omega}{\omega_n}$ ,  $\tau = \omega_n \cdot t$  and  $(\blacksquare)' = \frac{d}{d\tau}(\blacksquare)$ ,  $(\blacksquare)'' = \frac{d^2}{d\tau^2}(\blacksquare)$ .

Non-dimensional velocity and acceleration of the moving mass are defined as  $\dot{\chi} =$

$$a_0\omega_n\bar{\chi}', \ddot{\chi} = a_0\omega_n^2\bar{\chi}'', \text{ respectively, and } \xi_1 = \frac{c_1}{2m\omega_n}, \xi_3 = \frac{c_3a_0^2\omega_n}{2m}.$$

## 2.6 Analytical solution

To gain more insights of the dynamic behavior of the system the Harmonic Balance Method (HBM) is used to approximate the displacement transmissibility,  $\eta$ , of the vibration isolation system subject to sinusoidal excitation of the form  $\bar{A}\Omega^2 \sin(\Omega\tau - \varphi)$ . Using (8) and the non-dimensional form of the equation of motion (12) yields

$$\bar{\chi}'' + 2\xi_1\bar{\chi}' + 2\xi_3\bar{\chi}'^3 + \bar{\chi} + \frac{1}{\alpha}\left(\frac{\gamma^3}{2} + \beta\right)\bar{\chi}^3 = \bar{A}\Omega^2 \sin(\Omega\tau - \varphi) \quad \text{Eq. (14)}$$

Next the response of the system is assumed to be dominated by the first harmonic of amplitude, and given by

$$\bar{\chi}(\tau) = \bar{X} \sin(\Omega\tau) \quad \text{Eq. (15)}$$

Substituting (15) and its non-dimensional derivatives  $\frac{d}{d\tau}$  (■) and  $\frac{d^2}{d\tau^2}$  (■) into (14) yields

$$\begin{aligned} -\Omega^2 \bar{X} \sin(\Omega\tau) + 2\xi_1\Omega\bar{X} \cos(\Omega\tau) + 2\xi_3\Omega^3\bar{X}^3 \cos^3(\Omega\tau) + \\ \bar{X} \sin(\Omega\tau) + \frac{1}{\alpha}\left(\frac{\gamma^3}{2} + \beta\right)\bar{X}^3 \sin^3(\Omega\tau) = \bar{A}\Omega^2[\sin(\Omega\tau) \cos(\varphi) - \\ \cos(\Omega\tau) \sin(\varphi)] \end{aligned} \quad \text{Eq. (16)}$$

Applying trigonometric relations and taking up to the first harmonic term yields

$$\cos^3(\Omega\tau) = \left(\frac{\cos(3\Omega\tau)}{4} + \frac{3\cos(\Omega\tau)}{4}\right) \approx \frac{3}{4} \cos(\Omega\tau) \quad \text{Eq. (17-a)}$$

$$\sin^3(\Omega\tau) = \left(\frac{-\sin(3\Omega\tau)}{4} + \frac{3\sin(\Omega\tau)}{4}\right) \approx \frac{3}{4} \sin(\Omega\tau) \quad \text{Eq. (17-b)}$$

Further, substituting (17a-b) into (16) results in

$$\begin{aligned} -\Omega^2 \bar{X} \sin(\Omega\tau) + 2\xi_1\Omega\bar{X} \cos(\Omega\tau) + \frac{3}{2}\xi_3\Omega^3\bar{X}^3 \cos(\Omega\tau) + \\ \bar{X} \sin(\Omega\tau) + \frac{3}{4\alpha}\left(\frac{\gamma^3}{2} + \beta\right)\bar{X}^3 \sin(\Omega\tau) = \bar{A}\Omega^2[\sin(\Omega\tau) \cos(\varphi) - \\ \cos(\Omega\tau) \sin(\varphi)] \end{aligned} \quad \text{Eq. (18)}$$

Equating the coefficients of  $\sin(\Omega\tau)$  and  $\cos(\Omega\tau)$  results in

$$[-\Omega^2\bar{X} + \bar{X} + \frac{3}{4\alpha}(\frac{\gamma^3}{2} + \beta)\bar{X}^3] = \bar{A}\Omega^2\cos(\varphi) \quad \text{Eq. (19)}$$

$$2\xi_1\Omega\bar{X} + \frac{3}{2}\xi_3\Omega^3\bar{X}^3 = -\bar{A}\Omega^2\sin(\varphi) \quad \text{Eq. (20)}$$

Further simplification yields

$$[-\Omega^2\bar{X} + \bar{X} + \frac{3}{4\alpha}(\frac{\gamma^3}{2} + \beta)\bar{X}^3]^2 + [2\xi_1\Omega\bar{X} + \frac{3}{2}\xi_3\Omega^3\bar{X}^3]^2 = \bar{A}^2\Omega^4 \quad \text{Eq. (21)}$$

Displacement transmissibility is then defined as

$$R = \eta = \frac{\bar{X}}{\bar{A}} = \frac{\Omega^2}{\sqrt{(1 - \Omega^2 + \frac{3}{4\alpha}(\frac{\gamma^3}{2} + \beta)\bar{X}^2)^2 + (2\xi_1\Omega + \frac{3}{2}\xi_3\Omega^3\bar{X}^2)^2}} \quad \text{Eq. (22)}$$

In order to verify the validity of the HBM, a numerical simulation is conducted using fourth order Runge-Kutta method. The model's validation is examined in **Figure 6** which shows transmissibility,  $\eta$ , of the vibration isolation system versus non-dimensional frequency,  $\Omega$ . Both analytical and numerical solutions are shown in **Figure 6**. For comparison, transmissibility of linear system, i.e.  $\bar{\chi}'' + 2\xi_1\bar{\chi}' + \bar{\chi} = \bar{A}\Omega^2\sin(\Omega\tau - \varphi)$ , is also shown. **Table I** lists non-dimensional parameters used in model simulation. **Figure 6** shows good agreement between numerical and analytical solutions for the nonlinear vibration isolation system. Moreover, the superiority of the proposed nonlinear vibration isolation system compared to a linear system is evident around the resonant peak, i.e.  $\Omega = 1$ . The linear system, expectedly, has resonant peak at  $\Omega = 1$ .

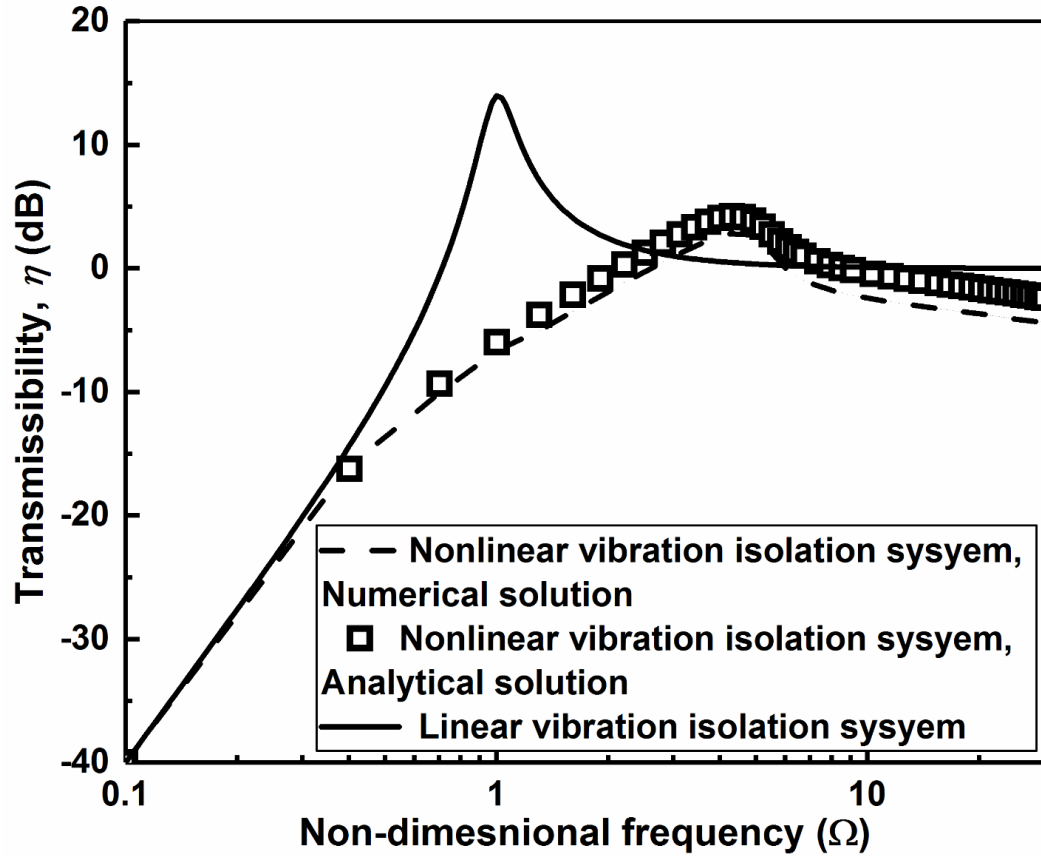


**Figure 6.** Displacement transmissibility ( $\eta$ ) of examined nonlinear-stiffness nonlinear-damping vibration isolation system compared to linear vibration isolation system.

However, **Figure 6** shows that the proposed nonlinear-damping nonlinear-stiffness vibration isolation system is more effective, compared to the linear system, in attenuating vibrations around resonance. The nonlinear vibration isolation system shows comparable vibration isolation characteristics at excitations lower than resonant frequency.

The effect of nonlinear damping,  $\xi_3$ , on displacement transmissibility is examined in **Figure 7**. Figure 7 shows that increasing the nonlinear damping,  $\xi_3$ , can suppress displacement transmissibility at higher frequencies by eliminating the undesired frequency-jump inherited in standard QZS vibration isolation systems.

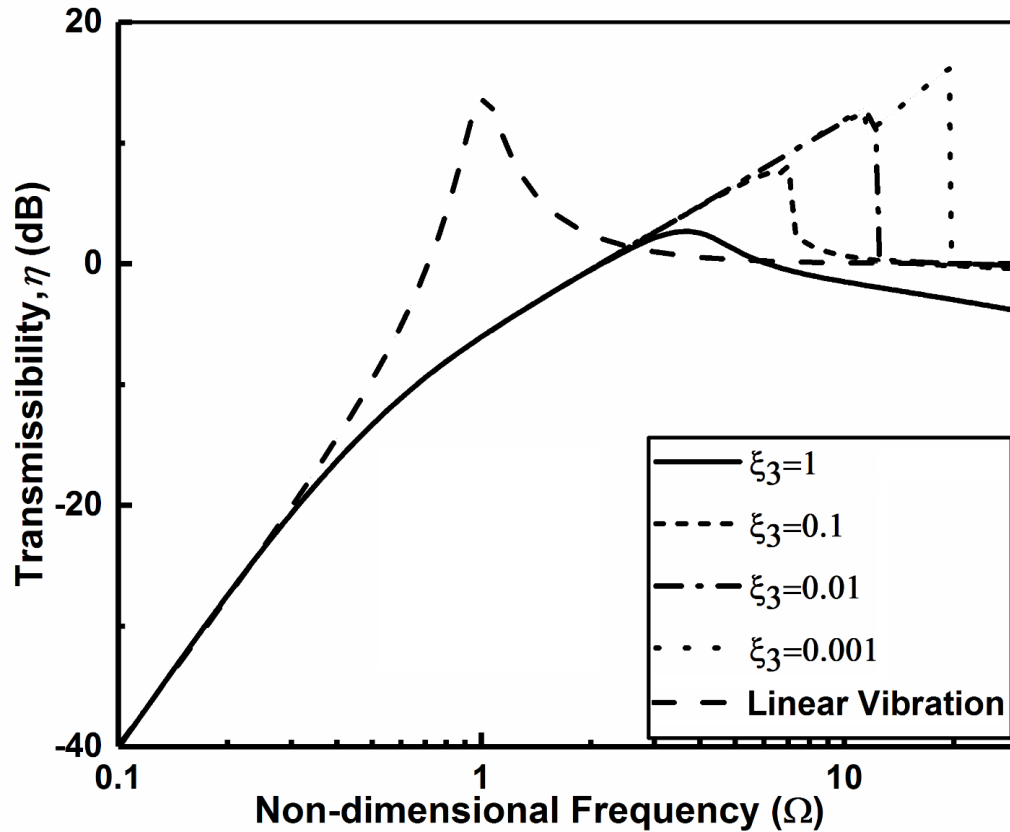


**Figure 7.** Effect of nonlinear damping ratio,  $\xi_3$ , on displacement transmissibility,  $\eta$ , ( $\xi_1 = 0.1$ ).

This is in agreement with the observations made by Daolin Xu et al. [40] and [64] Tehrani & Elliott. That is, both Daolin Xu et al. [38] and Tehrani & Elliott [62] noted that frequency jump phenomena is greatly affected by damping properties of the system. The superiority of the proposed vibration isolation system design is evident. Compared to a linear vibration isolation system, introducing additional damping nonlinearities suppresses displacement transmissibility not only around resonant frequencies,  $\Omega = 1$  but also at higher frequencies,  $\Omega > 1$ . The ability to attenuate higher frequencies is a desirable characteristic in vibration isolation systems. Next, the effect of stiffness nonlinearities introduced by the oblique mechanical springs and magnetic spring is

examined. **Figure 8** shows four different designs considered here to examine stiffness nonlinearities. A typical linear-damping linear-stiffness vibration isolation system (Design A) is shown for comparison. Designs B, C and D implement vibration isolation systems with different sources of stiffness nonlinearities.

**Table I.** Parameters used in nonlinear vibration isolation model simulation.

| Parameter | Value |
|-----------|-------|
| $\bar{A}$ | 1     |
| N         | 4     |
| $\alpha$  | 7.5   |
| $\beta$   | 1250  |
| $\xi_1$   | 0.1   |
| $\xi_3$   | 0.5   |
| $\sigma$  | 0.5   |

Linear and nonlinear damping is present and fixed, i.e.  $\xi_1 = 0.1$ ,  $\xi_3 = 1$ , respectively, in Designs B, C and D. However, Designs B, C and D have different sources of stiffness nonlinearities. Design B is described in (12) and has both oblique springs and a magnetic spring. Design C considers stiffness nonlinearities due to a magnetic spring only. Design D considers geometric stiffness nonlinearities due to mechanical oblique springs only. **Figure 9.** shows displacement transmissibility,  $\eta$ , for the four designs (A-D). The figure reveals the effectiveness of the combined nonlinear-damping nonlinear stiffness design (Design B) in suppressing vibrations across large frequency bandwidth. For Design C, when stiffness nonlinearities are only attributed to

the magnetic spring, displacement transmissibility increases significantly, compared to Design B. This is due to the absence of geometric negative stiffness nonlinearities introduced purposefully in Design B using oblique mechanical springs. On the other hand, the absence of large stiffness nonlinearities,  $k_{m3}$ , introduced by the magnetic spring is evident in displacement transmissibility of Design D.

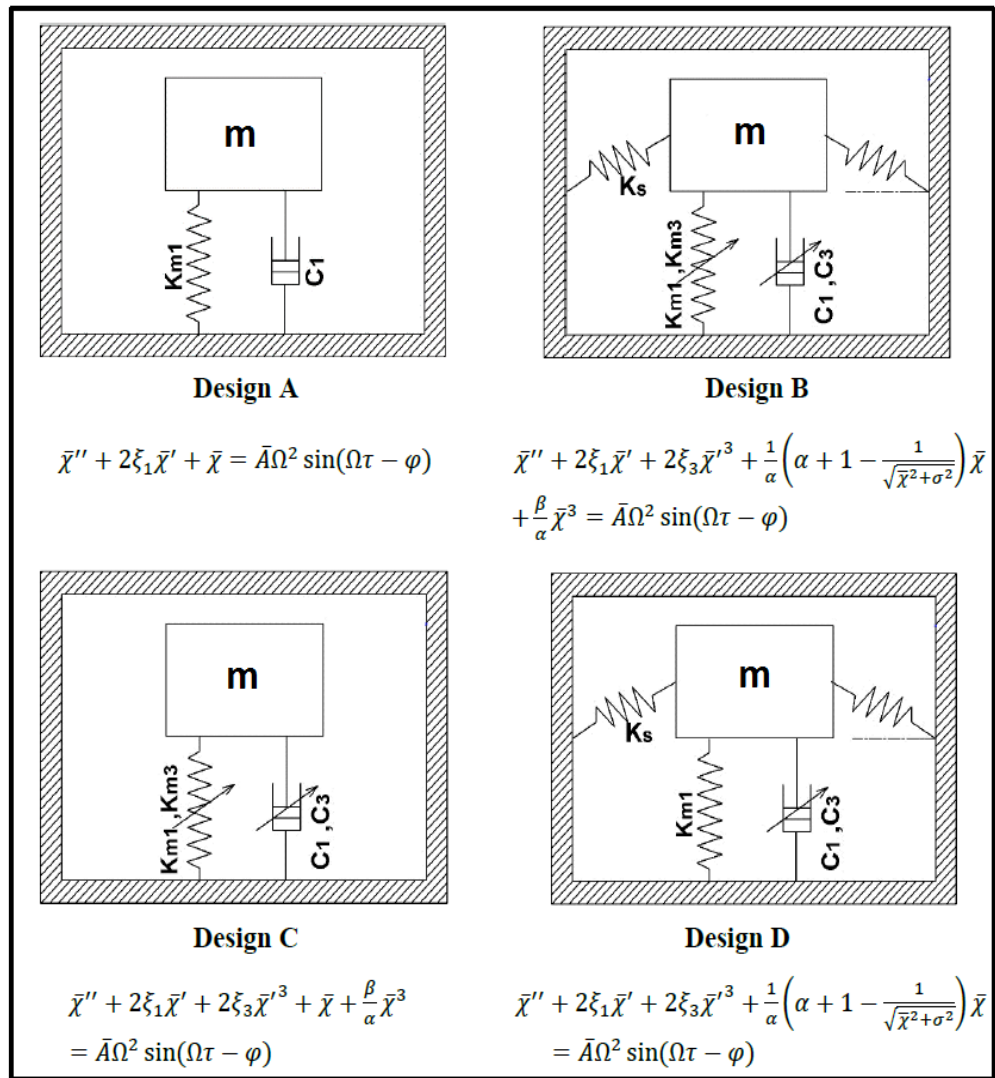


**Figure 8.** Comparison of four different vibration isolation designs: Linear system (A). Nonlinear-stiffness due to oblique springs and magnetic spring and nonlinear-damping (B). Nonlinear-stiffness due to magnetic spring and nonlinear-damping (C). Nonlinear stiffness due to oblique springs with nonlinear damping.

Compared to Design B, where both oblique springs and magnetic springs are present, Design D shows little impact on displacement transmissibility around resonance, i.e.  $\Omega = 1$ .

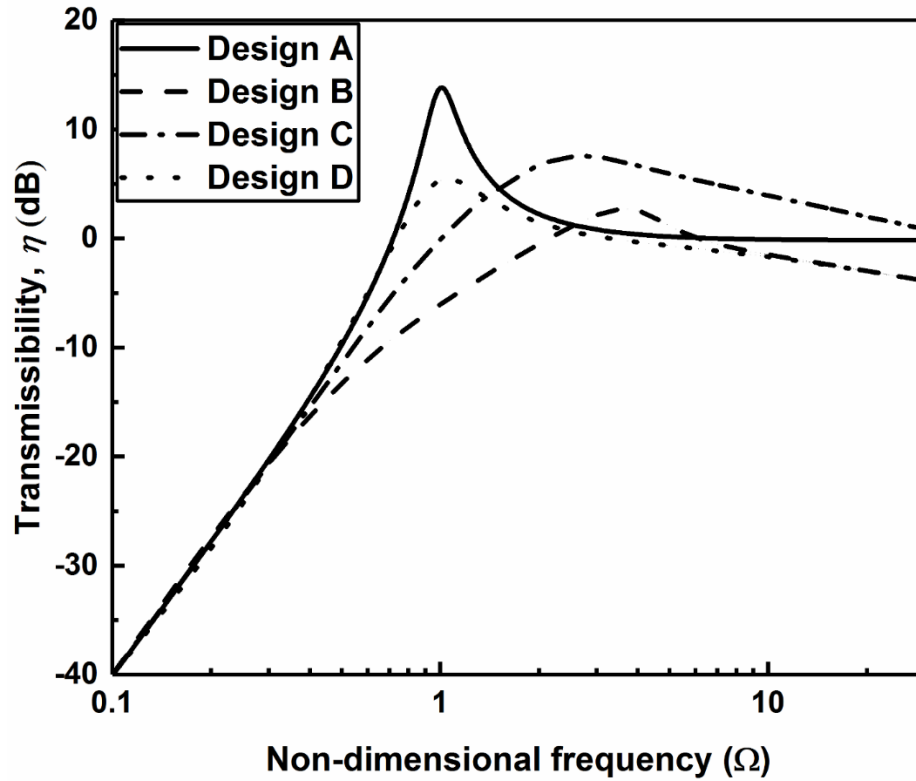


**Figure 9.** Displacement transmissibility ( $\eta$ ) versus non-dimensional frequency ( $\Omega$ ), for Design A, B, C, and D. ( $\xi_1 = 0.1$ ,  $\xi_3 = 1$ ).

**Figure 10** compares performance of described nonlinear-damping nonlinear-stiffness vibration isolation system to standard QZS system and linear system. Around resonance, i.e.  $\Omega = 1$ , both QZS system and described nonlinear-damping nonlinear-stiffness vibration isolation system appear to perform better in comparison to a linear vibration isolation system. In addition, both QZS and proposed nonlinear system have similar characteristics at lower frequencies, i.e.  $\Omega < 1$ . At higher levels of excitations, i.e.  $\Omega > 1$ , displacement transmissibility of described nonlinear vibration isolation system

decreases significantly, compared to QZS. The proposed nonlinear vibration isolation system appears to eliminate the frequency jump down phenomena traditionally inherited in standard QZS vibration isolation systems. This observation is, also, in agreement with results from **Figure 7**.

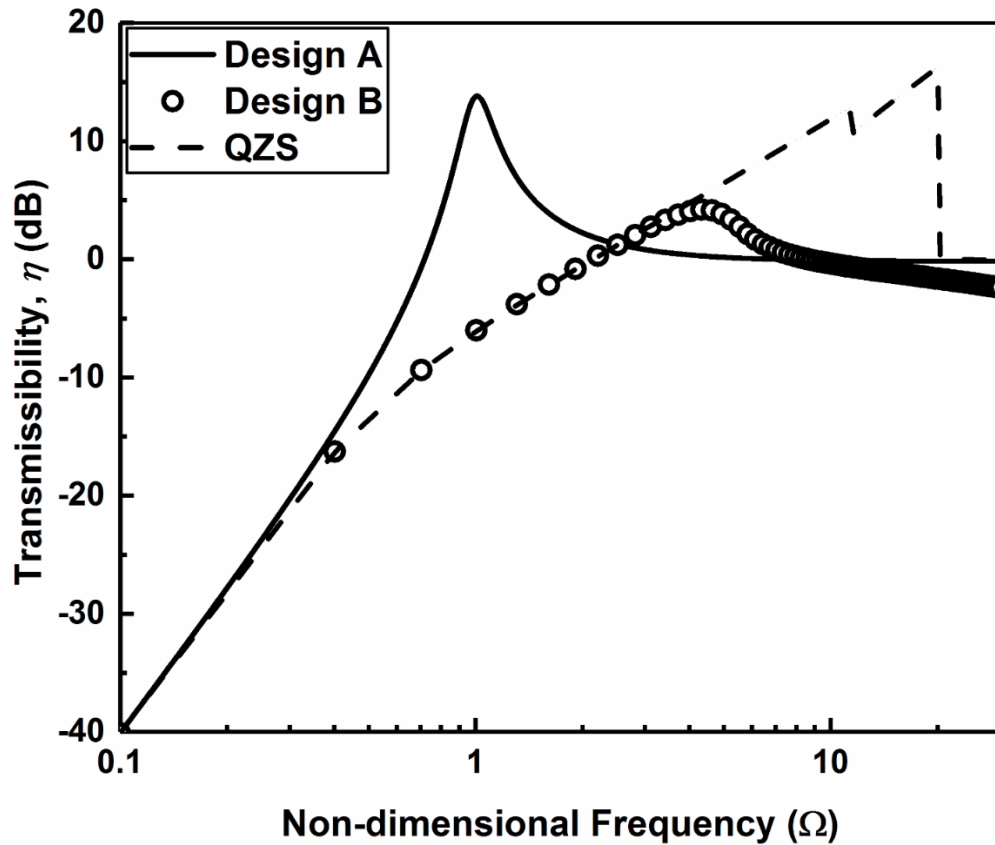


**Figure 10.** Displacement transmissibility ( $\eta$ ) of proposed nonlinear-stiffness nonlinear-damping Design B compared to standard QZS and linear vibration isolation systems, versus non-dimensional frequency sweeping ( $\Omega$ ).

## **CHAPTER 3**

### **THEORETICAL STUDY AND EXPERIMENTAL IDENTIFICATION OF ELASTIC-MAGNETIC VIBRATION ISOLATION SYSTEM**

The current chapter discusses on theoretical and experimental study of an elastic-magnetic vibration isolation device. The author has used parts of the current chapter in the research article, “Theoretical study and experimental identification of elastic-magnetic vibration isolation system “by S. M. Mahdi Mofidian and H. Bardaweel, published in Journal of Intelligent Material Systems and Structures, Volume 29, issue 18 (2018) which is adapted with permission from SAGE.

#### **3.1 Introduction**

Engineers have been dealing with ambient vibrations and oscillations generated by mechanical systems for over a century [5,6]. These vibrations may damage structures and machines or obstruct their operations. Hence, vibration isolation systems are used to prevent oscillations from traveling through equipment, structures, and machines that are susceptible to vibrations. Reviewing the massive literature on this subject is beyond the scope of this work. In this article, we briefly discuss the main advancements of recent vibration isolation systems. Nonetheless, Liu, C et al [30] and Ibrahim, R [34] provided detailed reviews on the subject of vibration isolation. Rivin also reviewed the fundamental information related to the design and operation of vibration isolation systems [4, 73]. Collette et al. performed a comprehensive review on recent patented

developments in active seismic vibration isolation systems [74]. Additionally, a survey of advances in vibration attenuation and control for space application was performed by Winthrop and Cobb [75].

Largely, vibration isolation systems can be characterized as linear and nonlinear vibration isolation systems [76,77]. A classical linear vibration isolation system uses a resilient stiffness element and energy dissipation element to absorb oscillations or obstruct their path [8]. Using this linear spring-mass-damper system, undesired vibrations are suppressed and dissipated via the damper into waste heat that is conducted away to the surrounding. However, traditional linear vibration isolation systems face major obstacles. Linear isolation systems are effective when the oscillation frequencies are well above their resonant frequency, i.e.  $\sqrt{2} \omega_n$ . A low resonant frequency isolation system of a fixed mass requires a soft spring [17]. This results in unavoidable higher static deflections. Additionally, several engineering structures and machines are subject to broadband oscillations with low frequency components. This includes shocks and random and chaotic disturbances transmitted to structures and machines including spacecraft, buildings, bridges, and automobiles [34]. This poses significant obstacles on design of linear vibration isolation systems.

Nonlinear approaches have been proposed as alternative route for traditional linear isolation systems. Stiffness nonlinearities [36,38,47,52] and damping nonlinearities [43,61,78] have been explored as techniques to improve isolation characteristics of vibration isolation systems. For instance, Bian and Jing proposed a passive bio-inspired, limb-like nonlinear vibration damper [79]. Their experimental and theoretical studies revealed that the nonlinear damping characteristics were beneficial for vibration isolation.

Additionally, Carrella et al. employed oblique springs along with vertical springs in the design of a vibration isolation system to achieve stiffness nonlinearities [48]. Results from their work revealed lower dynamic stiffness compared to static stiffness and nonlinear cubic force-displacement relationship. Moreover, a vibration isolation system with geometric nonlinearities was constructed using a scissor-like structure [36].

Recently, there has been growing interest in employing magnetic springs in the design of nonlinear vibration isolation systems [21,46,49]. For example, a tunable high-static–low-dynamic stiffness vibration isolator was introduced by Zhou and Liu [80]. The isolator was constructed by connecting a structural beam in parallel with a magnetic spring that is made of pair of electromagnets and a permanent magnet. Dong et al. built a high-static-low-dynamic stiffness vibration isolator using a combination of a magnetic negative stiffness spring and spiral mechanical spring [81]. Results from their work confirmed the ability of the isolator to attenuate vibrations in the range of 10 [Hz]. Other examples of magnetic spring based vibration isolation systems are reported in [82-84].

In this work we present a unique nonlinear vibration isolation system suitable for attenuating low frequency oscillations. The functionality of the presented vibration isolation system is achieved using a combination of elastic and magnetic structures with positive and negative stiffness characteristics, respectively, and viscous and magnetic damping components. The next section, i.e. Section 3.2, describes the design features and working principle of the vibration isolation system presented in this work.

Manufacturing and assembly of the isolator prototype are presented in Section 3.3. In Section 3.4 fundamental modeling of the presented isolator is performed. A two-prong modeling approach is carried out in Section 3.4: System-level and component-level

modeling approach. First, a finite element COMSOL model is developed for the main components of the proposed system: mechanical spiral spring and magnetic spring. Second, a lumped parameter model of the whole system is developed using first principle and solved using Harmonic Balance Method (HBM). The experimental apparatus used for characterization of the manufactured isolator is described in Section 3.5. Model validation and results from experiment are discussed in Section 3.6.

### 3.2 System design

**Figure 11** shows the design and configuration of the proposed elastic-magnetic vibration isolation system. Similar to a traditional vibration isolation system, the presented system uses a combination of springs and dampers to isolate the desired mass. It should be noted that this design is utilized based on 3D printing of different designs and the more efficient design is selected for the experiments. The system consists of springs, i.e. magnetic and mechanical springs, and dampers, i.e. viscous and magnetic dampers. Basic operation of the system begins with a solid magnet that is levitated between two stationary top and bottom ring permanent magnets. This three magnets arrangement results in a magnetic spring force developed between the levitated magnet and the stationary magnets. As shown in Figure 11, the levitated magnet is placed inside a mechanical flat spiral spring that is used to guide the levitated magnet and prevent it from realigning itself with the stationary magnets. A similar spring configuration was reported by Dong et al. [81]. The described combination of mechanical flat spiral spring and magnetic spring reduces the resonant frequency of the vibration isolator. As will be demonstrated in this article, the measured force-displacement curves of the flat spiral spring and the magnetic spring are characterized by positive and negative stiffness,

respectively. This results in lower resonant frequency and high-static-low-dynamic stiffness behavior of the described elastic-magnetic vibration isolation system.

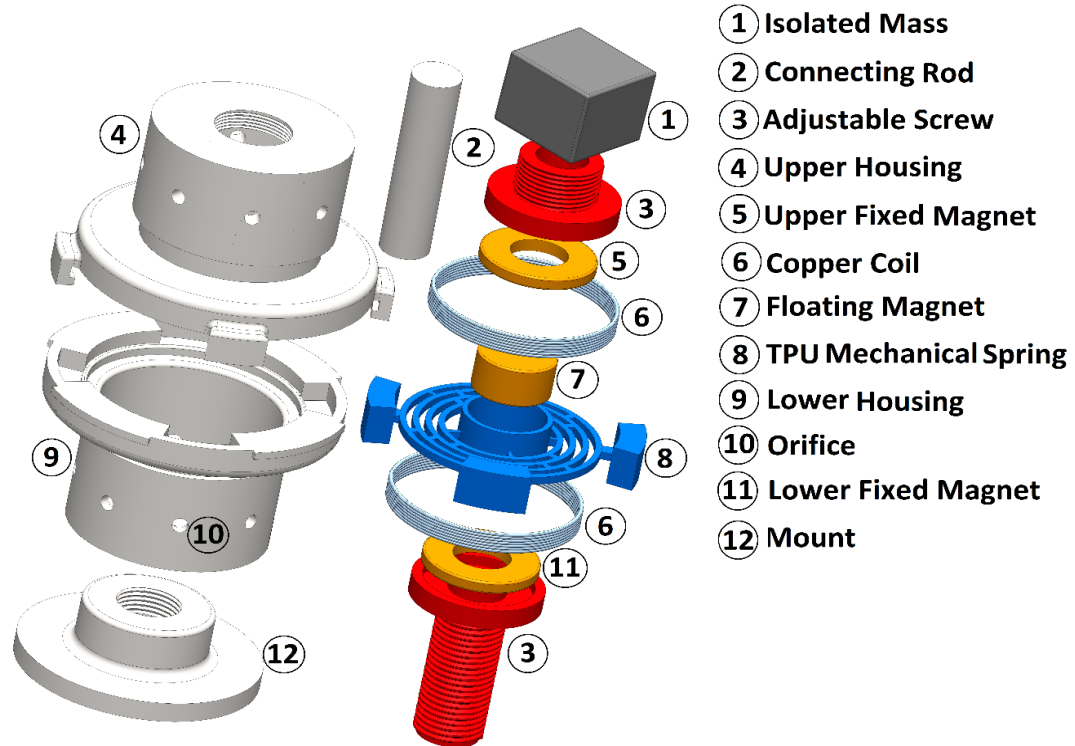


**Figure 11.** Cartoon schematic of the elastic-magnetic vibration isolator design: Exploded view (Left) and 3D sectional view (Right).

The working principle of the vibration isolator is explained in **Figure 12**. Here, copper coils are fixed around the rest position of the levitated magnet. When subject to external vibration, the levitated magnet moves vertically. Based on Lorentz Law, the relative motion of the levitated magnet inside the copper coils induces eddy currents in these coils. Consequently, a magnetic flux is generated in these coils that opposes the external magnetic flux and, thus, magnetic damping force is generated [85,86]. Additionally, orifices are implemented via top and bottom holes to introduce viscous damping. Consequently, the air inside the chamber is forced through the orifices and

around the levitated magnet mass. This results in additional viscous damping associated with air movement inside the isolator.

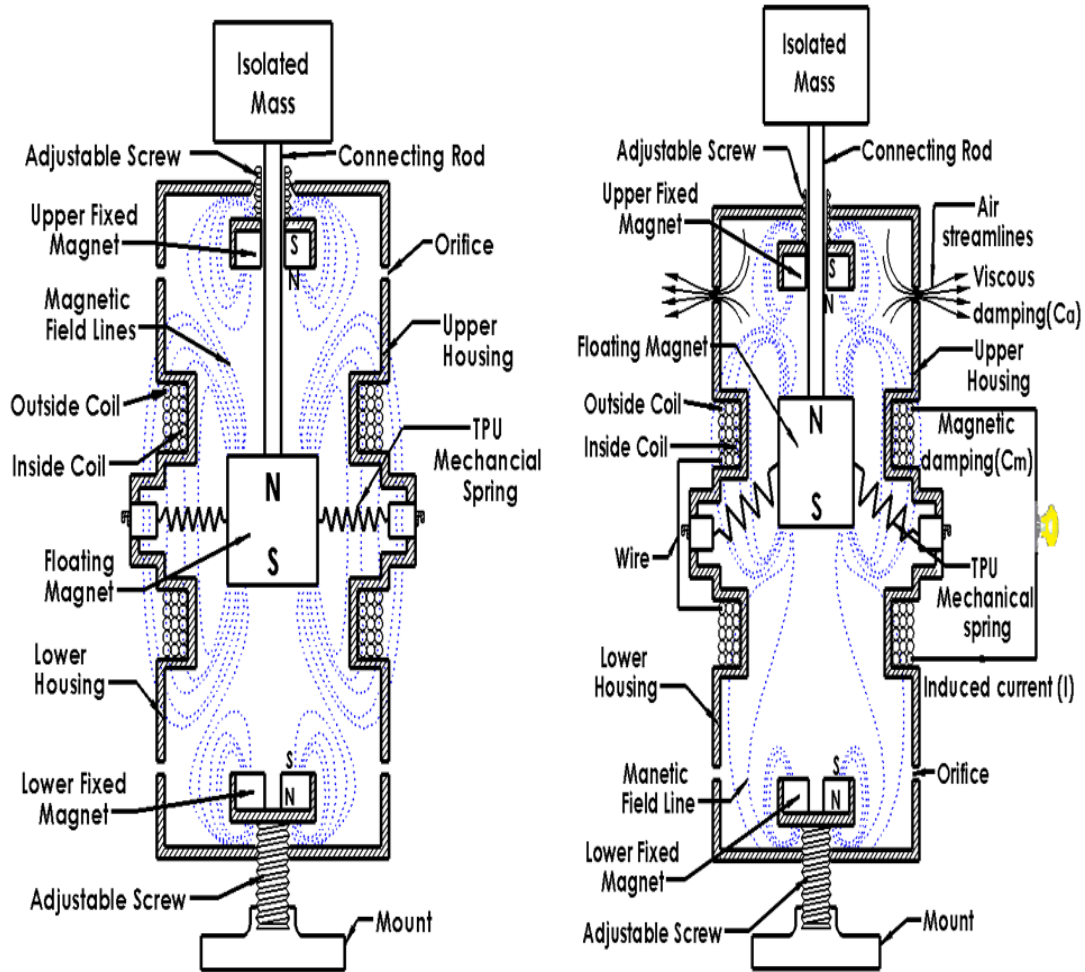


**Figure 12.** Working principle of the vibration isolator: Initial static position (Left) and dynamic operation (Right).

The isolated mass is connected to the mechanical and magnetic springs through a connecting rod. The rod passes through the top ring magnet while the bottom end of the rod is connected to the levitated magnet, as shown in **Figure 11**. Unlike previous studies [46, 47], direct mechanical contact between the levitated magnet and surrounding walls is avoided in the presented vibration isolation system. Additionally, this novel isolator is

oil-free and uses a combination of magnetic damper and magnetic spring to isolate the desired mass. On one hand, the use of magnetic spring results in negative stiffness. This plays essential role in decreasing the operational frequency of the isolator to lower values. Moreover, the eddy current damper implemented in this design is unique and makes the isolator oil-free and leakage-free. These unique features play significant role during the operation of the system. Moreover, a tuning screw is adopted in the design of the system to adjust the separating distance between magnets. As a result, the tuning screw can be used to alter the stiffness to a desired value in order to change system characteristics.

### 3.3 Manufacturing and assembly

For proof-of-concept purposes, the main parts of the elastic-magnetic vibration isolation prototype were manufactured using a rapid prototyping technique. CAD 3D drawings of the system components were prepared using Solidworks software and then converted into STereoLithography (STL) format readable by an Ultimaker 3 fused deposition modeling (FDM) 3D printer. The top and bottom casings were printed using Polylactic acid (PLA) thermoplastic filament. The mechanical spiral spring was printed using Thermoplastic Poly-Urethane (TPU) rubber-like filament. Upon assembly, neodymium iron boron (NdFeB) ring magnets were fixed on the top and bottom casings of the vibration isolator. The mechanical spiral spring was anchored inside the slots of the bottom casing. The solid magnet was then centered inside the spiral spring in a repulsive arrangement with respect to top and bottom ring magnets. The bottom and top ends of the connecting rod were glued to the levitated magnet and the isolated object mount, respectively. Next, the two casings, i.e. top and bottom, were locked together using the

latches and a 40 AWG copper wire was wrapped around the equilibrium position of the levitated magnet. The fully assembled device is shown in **Figure 13**. Properties of the assembled device are listed in **Table II**. Properties of the assembled vibration isolator prototype.

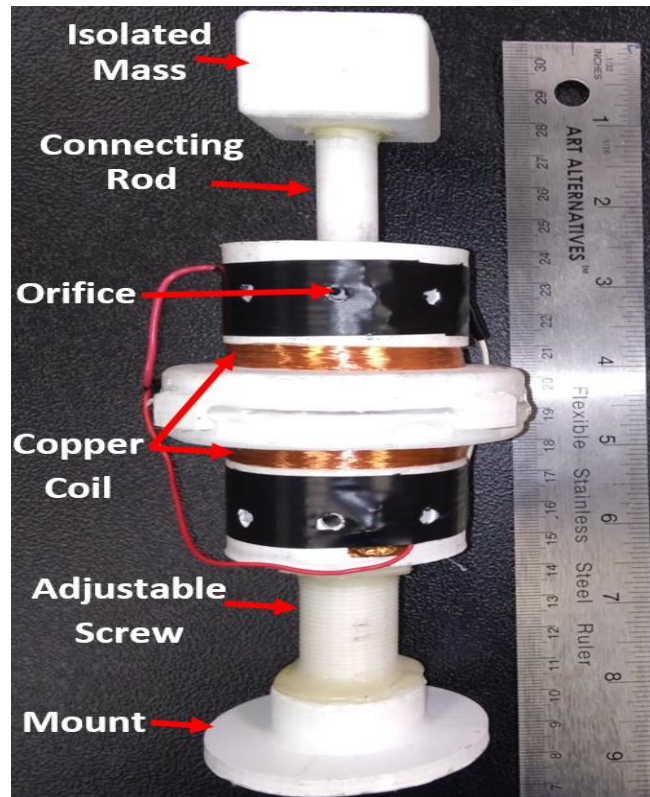


**Figure 13.** The fully assembled vibration isolator enclosed within 3D printed housing.

### 3.4 Theory and model

The described vibration isolator is modeled as a single DOF system and its free-body diagram is shown in **Figure 14**. In this analysis, it is assumed that there is no lateral movement and the effective mass,  $m$ , is displaced vertically with relative displacement,  $\chi = x - y$ .

**Table II.** Properties of the assembled vibration isolator prototype.

| <b>Parameter</b>  | <b>Property</b>                   | <b>Unit</b> |
|---|-----------------------------------|-------------|
| Coil material   | Copper, 40 AWG                    | -           |
| Coil resistance   | 1280                              | $\Omega$    |
| Coil number of turns  | 2000                              | -           |
| Isolator size (height $\times$ outer diameter)                              | 81.5 $\times$ 80.5                | mm          |
| Floating magnet material  | NdFeB-N42                         | -           |
| Floating magnet size (height $\times$ diameter)                             | 12.7 $\times$ 19.05               | mm          |
| Fixed magnets material  | NdFeB-N42                         | -           |
| Fixed magnets size (Outer diameter $\times$ Inner diameter $\times$ height) | 2.54 $\times$ 12.7 $\times$ 3.175 | mm          |
| Housing material  | Polylactic Acid (PLA)             | -           |
| Isolated mass   | 0.2                               | kg          |
| Length of coil per turn   | 0.142                             | m           |
| Mechanical spring material  | Thermoplastic poly-Urethane (TPU) | -           |
| Diameter of magnet holder in mechanical spring                              | 19.05                             | mm          |
| Thickness of mechanical spring structure                                    | 2                                 | mm          |
| Width of mechanical spring structure  | 2                                 | mm          |
| Diameter of orifices  | 3.8                               | mm          |

As we will demonstrate later in this article, the mechanical spiral spring behaves in a linear fashion with stiffness coefficient,  $K_{ss}$ , while the magnetic spring exhibits nonlinear behavior described using linear,  $K_{m1}$ , and nonlinear,  $K_{m3}$ , stiffness coefficients, respectively. Using Newton's Second Law, the equation of motion describing the dynamic behavior of the vibration isolator is

$$m\ddot{x} + c_a(\dot{x} - \dot{y}) + c_m(\dot{x} - \dot{y}) + K_{ss}(x - y) + K_{m1}(x - y) + K_{m3}(x - y)^3 = 0 \quad \text{Eq. (23)}$$

In this analysis, it is assumed that both viscous damping and magnetic damping are proportional to velocities, i.e.  $(\dot{x} - \dot{y})$ . To further simplify the governing equation (23), subtract and add  $m\dot{y}$  from both sides of (23) and use  $\ddot{\chi} = \ddot{x} - \ddot{y}$ ,  $\dot{\chi} = \dot{x} - \dot{y}$  and  $\chi = x - y$  to obtain

$$m\ddot{\chi} + c\dot{\chi} + K_1\chi + K_3\chi^3 = -m\ddot{y} \quad \text{Eq. (24)}$$

In (24) it is assumed that air viscous damping,  $c_a$ , and magnetic damping,  $c_m$ , are both linearly dependent on velocity,  $\dot{\chi}$  and, thus, lumped into total damping parameter,  $c_1$ , given by  $c_1\dot{\chi} = (c_a + c_m)\dot{\chi}$ . Moreover, the linear stiffness coefficients of spiral spring,  $K_{ss}$ , and magnetic spring,  $K_{m1}$ , are lumped into  $K_1 = K_{ss} + K_{m1}$  and the nonlinear stiffness coefficient of the magnetic spring is  $K_3 = K_{m3}$ . Harmonic Balance Method (HBM) [87,88] is implemented to solve the nonlinear equation of motion of the described system. Rewriting (24) in non-dimensional form for a base-excitation harmonic waveform  $y = A \sin(\omega t + \varphi)$  yields

$$\bar{\chi}'' + 2\xi_1\bar{\chi}' + \bar{\chi} + \alpha\bar{\chi}^3 = \Omega^2 \sin(\Omega\tau + \varphi) \quad \text{Eq. (25)}$$

where  $\bar{\chi} = \frac{\chi}{A}$ ,  $\omega_n = \sqrt{\frac{k_1}{m}}$ ,  $\alpha = \frac{k_3 A^2}{m\omega_n^2} = \frac{k_3 A^2}{k_1}$ ,  $\Omega = \frac{\omega}{\omega_n}$ ,  $\tau = \omega_n \cdot t$ ,  $\bar{\chi}' = \dot{\chi}/A\omega_n$ ,  $\bar{\chi}'' = \ddot{\chi}/A\omega_n^2$ , and  $\xi_1 = \frac{c_1}{2m\omega_n}$ . For a harmonic base-excitation waveform, the response of the system is assumed to be dominated by the first harmonic of amplitude [78, 87], and given by

$$\bar{\chi}(\tau) = \bar{X} \sin(\Omega\tau) \quad \text{Eq. (26)}$$

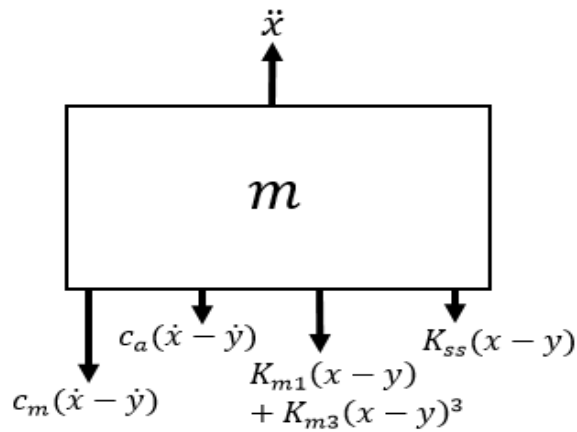


**Figure 14.** Free-body diagram of the single DOF vibration isolator subject to base excitation.

Substituting (26) and its non-dimensional derivatives  $\frac{d}{d\tau}$  (■) and  $\frac{d^2}{d\tau^2}$  (■) into (25) yields

$$\begin{aligned} -\Omega^2 \bar{X} \sin(\Omega\tau) + 2\xi\Omega\bar{X} \cos(\Omega\tau) + \bar{X} \sin(\Omega\tau) + \alpha\bar{X}^3 \sin^3(\Omega\tau) \\ = \Omega^2 \sin(\Omega\tau + \varphi) \end{aligned} \quad \text{Eq. (27)}$$

Applying trigonometric relations and taking up to the first harmonic term yields

$$\sin^3(\Omega\tau) = \left( \frac{-\sin(3\Omega\tau)}{4} + \frac{3\sin(\Omega\tau)}{4} \right) \approx \frac{3}{4} \sin(\Omega\tau) \quad \text{Eq. (28)}$$

Further, substituting (28) into (27) results in

$$\begin{aligned}
& -\Omega^2 \bar{X} \sin(\Omega\tau) + 2\xi\Omega\bar{X} \cos(\Omega\tau) + \bar{X} \sin(\Omega\tau) + \frac{3}{4}\alpha\bar{X}^3 \sin(\Omega\tau) \\
& = \Omega^2 [\sin(\Omega\tau) \cos(\varphi) + \cos(\Omega\tau) \sin(\varphi)]
\end{aligned} \tag{Eq. (29)}$$

Equating the coefficients of  $\sin(\Omega\tau)$  and  $\cos(\Omega\tau)$  in (27) results in

$$[\bar{X} - \Omega^2 \bar{X} + \frac{3\alpha}{4} \bar{X}^3] = \Omega^2 \cos(\varphi) \tag{Eq. (30-a)}$$

$$2\xi\Omega\bar{X} = \Omega^2 \sin(\varphi) \tag{Eq. (30-b)}$$

Further simplification yields

$$[\bar{X} - \Omega^2 \bar{X} + \frac{3\alpha}{4} \bar{X}^3]^2 + [2\xi\Omega\bar{X}]^2 = \Omega^4 \tag{Eq. (31)}$$

Using the absolute displacement of the payload mass, i.e.  $x = A\bar{X}\sin(\Omega\tau) + y$ ,

the absolute displacement transmissibility ratio,  $\eta_a$  is given by

$$\eta_a = \left| \frac{x}{y} \right| = \left| \frac{A(\bar{X} \sin(\Omega\tau) + \sin(\Omega\tau + \varphi))}{A} \right| = \sqrt{1 + \bar{X}^2 + 2\bar{X} \cos(\varphi)} \tag{Eq. (32)}$$

Substituting (30-a) into (32) the absolute transmissibility ratio,  $\eta_a$ , is given by

$$\eta_a = \sqrt{\frac{\Omega^2 + \bar{X}^2(2 - \Omega^2) + \frac{3\alpha}{2}\bar{X}^4}{\Omega^2}} \tag{Eq. (33)}$$

### 3.5 Experimental apparatus for characterization tests

This section describes the experimental setups used for characterizing the fabricated vibration isolator prototype. The two main experimental setups used in this work are shown in Figure 15-16. **Figure 15** shows the apparatus used for measuring restoring forces of mechanical and magnetic springs. The vibration isolator was fixed on a test stand (SHIMPO FGS-250W), and displacement sensor (KEYENCE IL-100) and digital force sensor (SHIMPO FG-3006) were used to measure displacement and restoring forces, respectively. While the hand-operated wheel was gradually lowered,

both displacement and force readings were recorded using a data acquisition system (NI myDAQ) and stored on a PC for later analysis. The experiment setup was also used to measure damping and the resonant frequency of the vibration isolator.

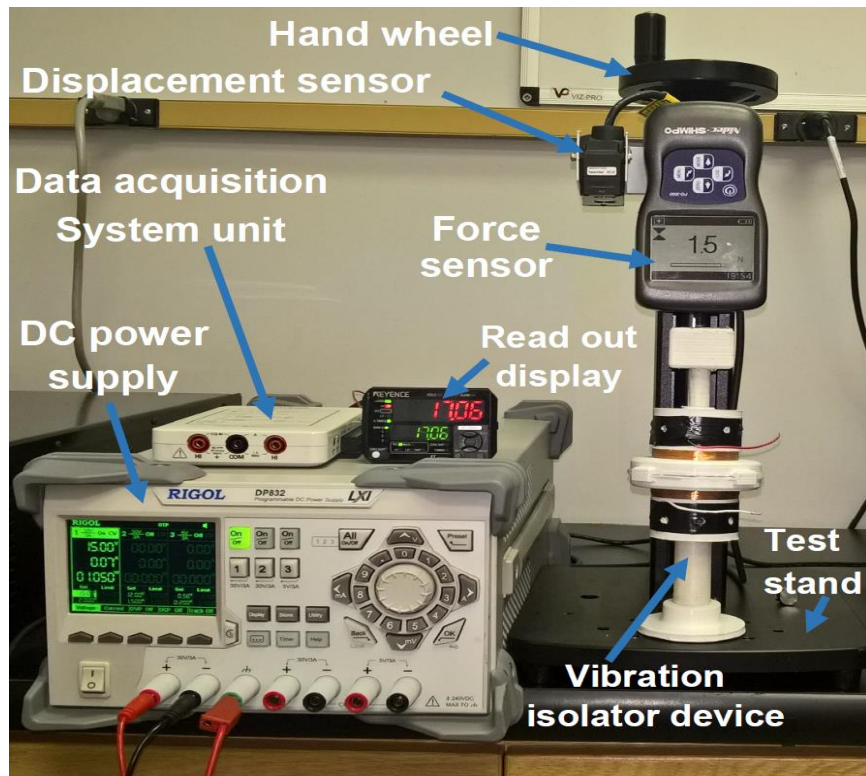


**Figure 15.** Lab experiment setup used to measure restoring forces of the magnetic and mechanical springs.

**Figure 16** shows the apparatus used for dynamic characterization of the vibration isolator. The setup consists of a shaker table (VT-500, SENTEK DYNAMICS), two accelerometers (PCB333B30 model, PCB Piezotronics), power amplifier (LA-800, SENTEK DYNAMICS), vibration controller (S81B-P02, SENTEK DYNAMICS), data acquisition system (NI myDAQ) and a PC. Upon characterization tests, the device was securely mounted on the shaker table top as shown in Figure 16. The PC-controlled shaker table was then used to excite the device at predetermined frequencies, i.e. 7-30

[Hz]. Transmissibility and isolation characteristics of the device were detected using the data acquisition system.

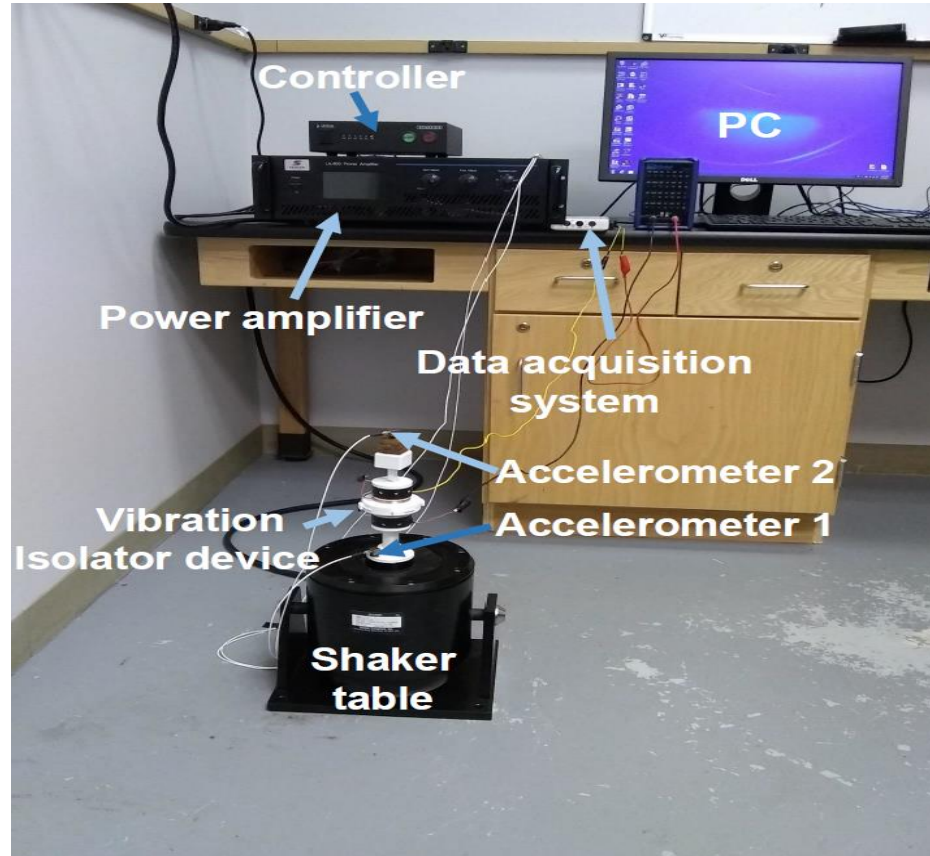


**Figure 16.** Lab experiment setup used for measuring displacement transmissibility of the vibration isolator.

### 3.6 Results and discussion

Both experimentation and theoretical analysis were used to fully characterize the vibration isolator. Tests were focused on component-level and system-level characterization. Magnetic spring and mechanical spiral spring were characterized using the apparatus shown in **Figure 15**. In addition, COMSOL models were developed for both magnetic and mechanical springs. The system-level characterization tests were focused on dynamic behavior of the device using the apparatus shown in **Figure 16**.

Transmissibility of the device was measured and modeled. The results from these measurements and models are discussed in this section.

A COMSOL model was developed in order to estimate both magnetic force and magnetic damping characteristics of the three magnet arrangement. The model was developed using the AC/DC Module in COMSOL Multi-physics software. For the geometry shown in **Figure 17**, a 2D axisymmetric model was adopted, and thereby, all the magnets were represented by rectangles along the  $\chi$ -plane.

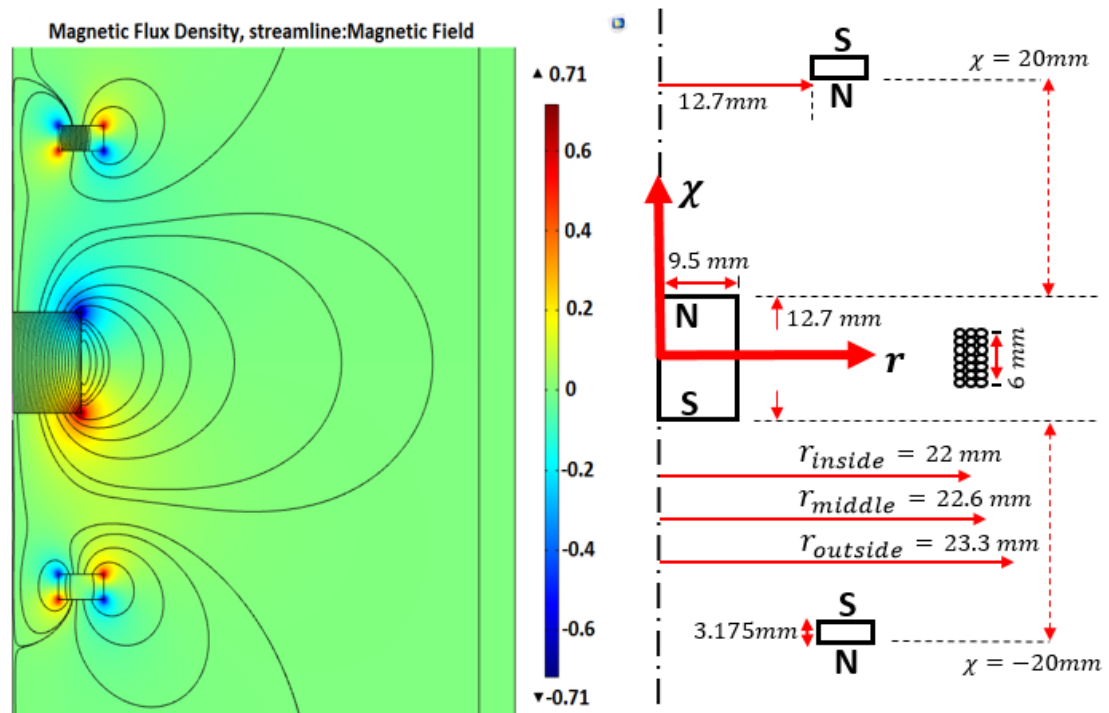


**Figure 17.** COMSOL simulation of magnets interaction in the vibration isolator: The oscillatory motion of the floating solid magnet as it moves between the two fixed top and bottom ring magnets (Left). Cartoon schematic of the magnets arrangement, dimensions, and geometries (Right).

In model simulation, it was assumed that the remaining edges of each magnet were magnetically insulated and the relative permeability of air domain surrounding the magnets was set to a unity. A moving mesh function was used upon model simulation of

the levitated magnet as it oscillated between the two fixed top and bottom magnets. A parametric sweep was used to estimate the magnetic restoring force and magnetic flux density as a result of the oscillatory motion of the levitated magnet. The governing equation for the COMSOL model simulation was based on Ampère's law. The relative tolerance was set to  $5e-6$ . **Figure 17** shows results from COMSOL model for the three magnet arrangement at predetermined position, i.e.  $\chi = 0$  [mm]. As the levitated magnet moved between the two stationary magnets, the magnetic flux density,  $B$ , was estimated at three coil sections, i.e. inner ( $r_{\text{inside}}=22$  mm), mid-way ( $r_{\text{middle}}=22.6$  mm), and outer ( $r_{\text{outside}}=23.3$  mm). **Figure 18** shows the simulation results at these three different locations. As shown in **Figure 18**, the magnetic flux density,  $B$ , varied slightly at those three sections and became stronger towards the inner side of the coil. Assuming uniform magnetic flux density [59, 89], the magnetic damping is given by  $c_m = \frac{(\sigma)^2}{R} = \frac{(N\bar{B}l)^2}{R}$  [61] and estimated at approximately,  $c_m=0.051[\text{N} \cdot \frac{\text{s}}{\text{m}}]$ , where  $\sigma = N\bar{B}l$  is the electromechanical coupling coefficient,  $R$  is total resistance,  $l$  is length of the coil per turn,  $N$  is the number of coil turns, and  $\bar{B}=0.0286$  [T] is taken as the maximum magnetic flux density in the air gap between the moving magnet mass and middle coil section ( $r_{\text{middle}}=22.6$  mm) [90]. The COMSOL model was also used to simulate the restoring force of the magnet arrangement,  $F_m$ . Figure 19 compares the magnetic force,  $F_m$ , obtained using COMSOL model against measured magnetic force, obtained using apparatus shown in **Figure 15**. In both experiment and COMSOL model, the levitated magnet was displaced vertically between the two stationary magnets. During this process, the magnetic force was estimated at several points. Simulation results agree with

measured data. In addition, the force-displacement curve exhibits hardening nonlinear characteristics with nonlinear stiffness behavior.

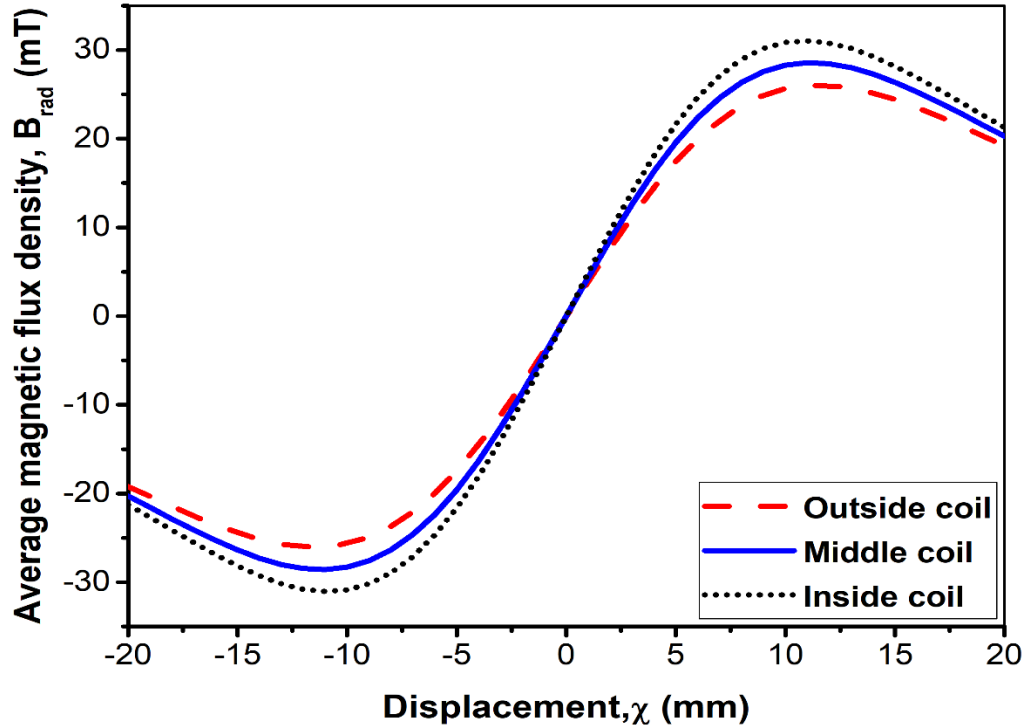


**Figure 18.** COMSOL simulated flux density of the floating magnet inside the vibration isolator.

The obtained force-displacement curve was curve-fitted to a higher order polynomial, i.e.  $K_{m1}\chi + K_{m3}\chi^3$  and the obtained linear and nonlinear stiffness coefficients of the magnetic spring i.e.  $K_{m1}$  and  $K_{m3}$ , respectively, are shown in **Figure 19**. The flat spiral spring plays an essential role in the presented vibration isolation design. **Figure 20** shows the design of the spiral spring adopted in this work. The spring consists of a central holder where the levitated magnet is placed. The magnet holder is connected to a flat spiral structure which supports loads along the longitudinal axis. A set of supporting bridges across the spiral structure is used to prevent the levitated magnet

from tilting along the transverse plane. To fully characterize the spiral spring, a COMSOL model was developed to obtain force-displacement curve and stress concentration points.

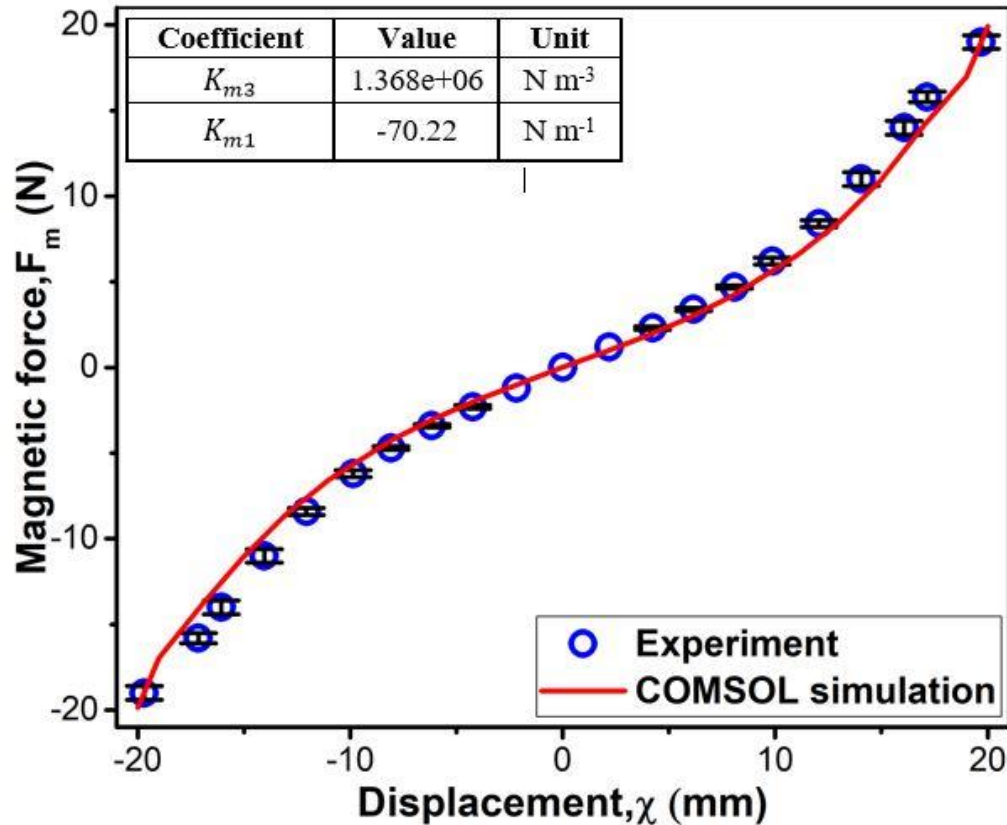


**Figure 19.** Measured and COMSOL simulated nonlinear magnetic restoring force versus displacement. The nonlinear magnetic force is fit to a third order polynomial of the form  $K_{m1}\chi + K_{m3}\chi^3$ .

The COMSOL model was developed using the Solid Mechanics Interface under the Structural Mechanics module in COMSOL Multi-physics software. A 3D model of the mechanical spring was adopted. All the anchors of the spring shown in **Figure 20** were set as fixed constrains boundary conditions. Upon modeling, a distributed load was applied on the magnet holder of the spring shown in **Figure 20**. The governing equation used was based on the linear elastic material model and the convergence tolerance was

set to  $1e-4$ . Additionally, the force-displacement curve was measured experimentally using the apparatus shown in **Figure 15**.

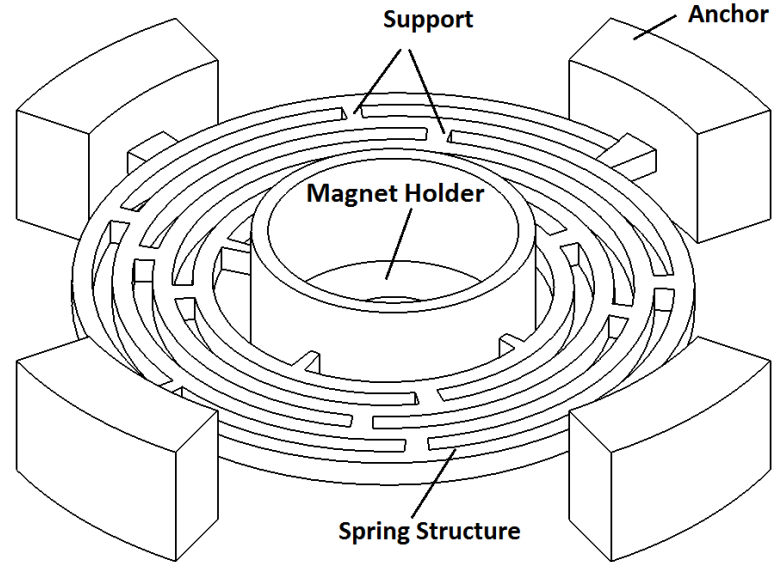


**Figure 20.** 3D geometry and main components of the mechanical spiral spring used in the vibration isolator.

**Figure 21** shows the force-displacement curve of the spiral spring obtained using experiment and COMSOL. Both COMSOL simulation model and experimentally measured data exhibit linear behavior with a positive stiffness coefficient of approximately  $K_{ss} = 688.8 \text{ [N m}^{-1}\text{]}$  and  $681.8 \text{ [N m}^{-1}\text{]}$ , respectively. On the other hand, the magnetic spring has a negative linear stiffness coefficient of  $K_{m1} = -70.2 \text{ [N m}^{-1}\text{]}$ . This negative stiffness, when combined with the positive stiffness of the spiral spring, reduces resonant frequency of the overall vibration isolation system, i.e.  $k_1 = K_{ss} + K_{m1} = 618.6 \text{ [N m}^{-1}\text{]}$ . The presence of both positive and negative stiffness elements in the vibration isolation system enables the system to support high static loads while having smaller dynamic stiffness. Thus, the vibration isolation system experiences small-

static deflections due to the high-static stiffness while, simultaneously, possesses lower resonant frequency due to the high-dynamic stiffness characteristics [48].

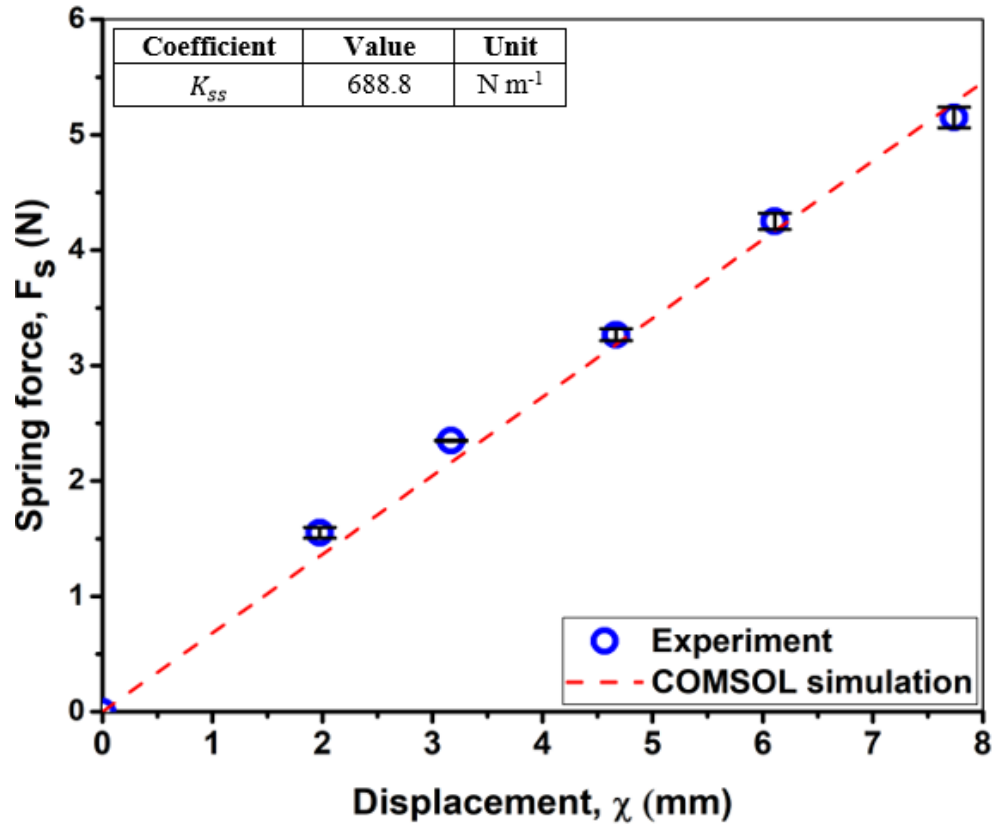


**Figure 21.** Measured and COMSOL simulated mechanical spring restoring force versus displacement. The linear mechanical spring restoring force is fit to  $K_{ss}\chi$ .

It is worth noting that the work presented in this article focused on proof-of-concept characterization tests and modeling rather than optimization of design parameters. Nonetheless, proof-of-concept characterization tests and modeling efforts reported here confirm the positive and negative stiffness characteristics of the mechanical spiral spring and magnetic spring, respectively. Next, stress concentration points were determined using the COMSOL model. **Figure 22** shows Von Mises stress distribution and deflections in response to pre-specified payload, i.e. 4 [N]. This payload value used

in the model simulation was set as twice as the value observed in the experiment. The results show that the supporting bridges are the most susceptible part of the spiral spring to axial loads. The maximum Von Mises stress observed was around 3.0 [MPa]. Simulation results also suggests that stress increases towards the center, i.e. closer to the levitated magnet. That is, bridges closer to the magnet holder experienced approximately 3.0 [MPa] while bridges far away from the socket experienced less stress, 1.9 [MPa].

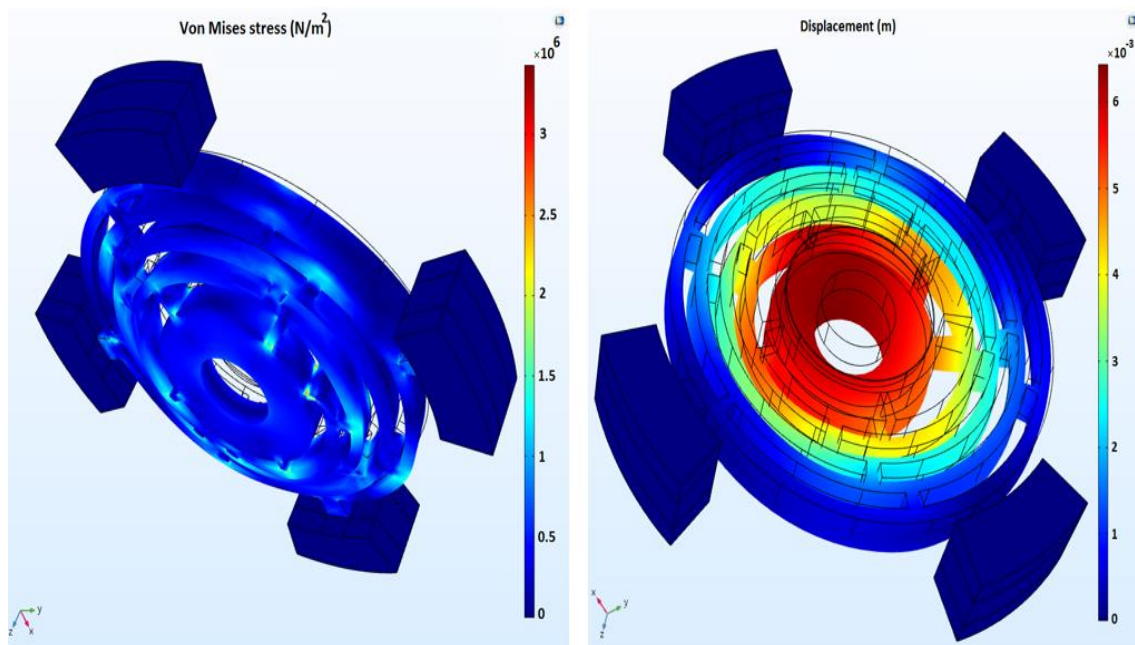


**Figure 22.** COMSOL simulation of the mechanical spiral spring behavior in response to 4 [N] payload: Von Mises stresses (Left) and corresponding displacement (Right).

To fully characterize the vibration isolation system, both resonant frequency,  $\omega_n$ , and total damping,  $c$ , were measured using ring-down technique. With no external source of excitation, the vibration isolator was held steadily and then released after the levitated magnet was brought to a predetermined height. The obtained ring-down waveform was then used to estimate resonant frequency,  $\omega_n$ , and total damping of the system,  $c$ , using the logarithmic decrement method [76, 91,92]. The resonant frequency of the vibration

isolator was approximately 8.85 [Hz]. The total damping,  $c$ , was found approximately 2.44  $[\text{N} \cdot \frac{\text{s}}{\text{m}}]$  which implied viscous damping of  $c_a = 2.389 [\text{N} \cdot \frac{\text{s}}{\text{m}}]$  and magnetic damping of  $c_m = 0.051 [\text{N} \cdot \frac{\text{s}}{\text{m}}]$ . Next, the apparatus shown in **Figure 16** was used to investigate the frequency response of the device. Upon running the experiment, a sampling rate of 1000 [Hz] was used and 60,000 data points per test were collected while the frequency was swept between 7- 30 [Hz]. Each experiment was repeated twice and uncertainty analysis was carried out as indicated by the error bars on Figure 23-24. **Figure 23** shows model simulation (33) and measured absolute displacement transmissibility,  $\eta_a$ , of the device at acceleration level of 1.0 g  $[\text{m s}^{-2}]$ .

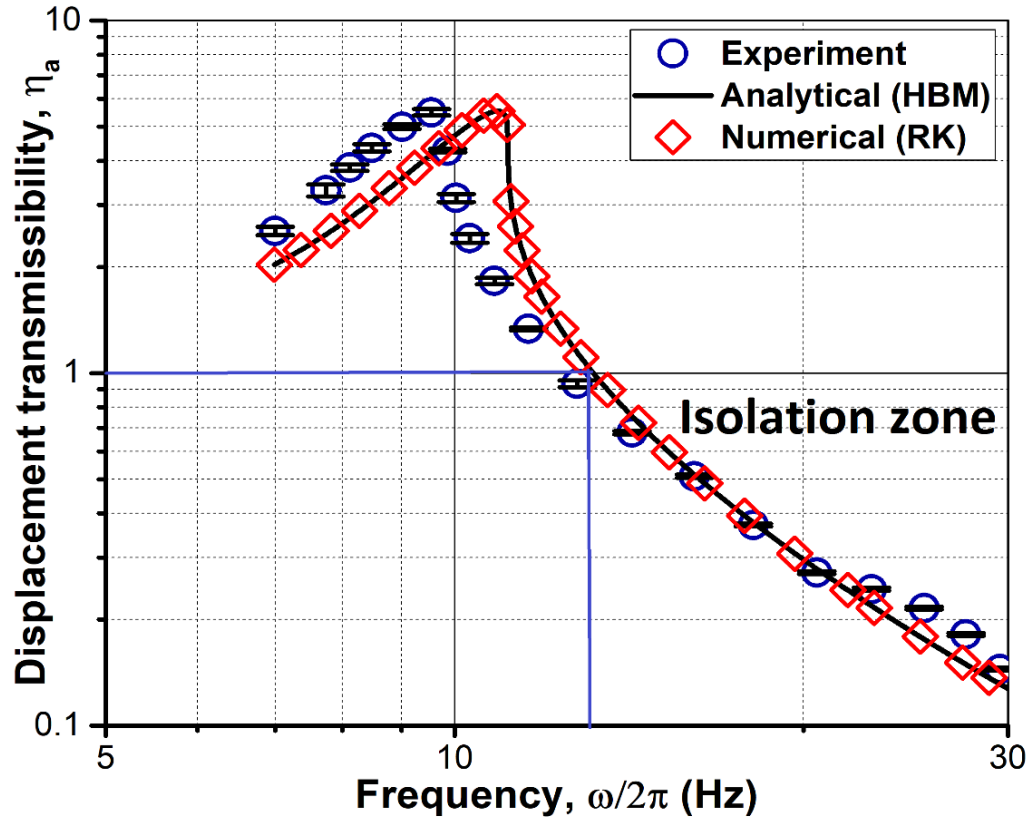


**Figure 23.** Measured and model simulation of displacement transmissibility of the vibration isolator versus frequency at acceleration level of  $1.0g$  [ $m\ s^{-2}$ ]. Model simulations are performed using Harmonic Balance Method (HBM) and 4<sup>th</sup> order Runge-Kutta (RK) numerical method.

The isolation region of the vibration isolator is apparent at frequencies higher than  $12.5$  [Hz] where transmissibility of the vibration isolator drops to less than unity, i.e.  $\eta_a < 1$ . Prior to  $12.5$  [Hz] disturbances from the base were transmitted to the isolated mass. Nonetheless, this lower frequency region is not of significance to the design of an isolator since vibration isolators are meant to operate beyond the cut-off frequency, i.e. when  $\eta_a \leq 1$ . **Figure 23** also shows acceptable match between HBM model simulations and measured data. However, **Figure 23** suggests that some deviation between HBM model simulations and experiment exists. Dong et al. [81] and Berdy et al. [92] made similar observations where peaks predicted by models were slightly shifted from

measured data. To investigate this mismatch between HBM model simulation and experiment a fourth order Runge-Kutta (RK) numerical method was used to solve the dynamic model of the vibration isolator given by (24). Results from Runge-Kutta numerical method confirmed those obtained using HBM model simulations. During experiment, a lateral vibration was observed-especially near resonance. This suggests that discrepancy between model and experiment may be attributed to the presence of lateral vibrations (wobbling) in the system. That is, at high level of acceleration, i.e.  $1g [m s^{-2}]$  and close to resonance, geometry misalignment results in lateral relative displacement of the levitated magnet. As a result, this lateral motion triggers other modes of vibrations that are not accounted for in the presented model. This is because the model we present in this work accounts only for vertical displacement along the  $\chi$ -direction. Similar observation was made by [81].

**Figure 24** shows displacement transmissibility of the isolator obtained using experiment and model simulations at lower acceleration level, i.e.  $0.25g [m s^{-2}]$ . Results from model simulations show good agreement with experimentally measured data. At this lower acceleration level, the lateral vibrations of the isolator decreased significantly.

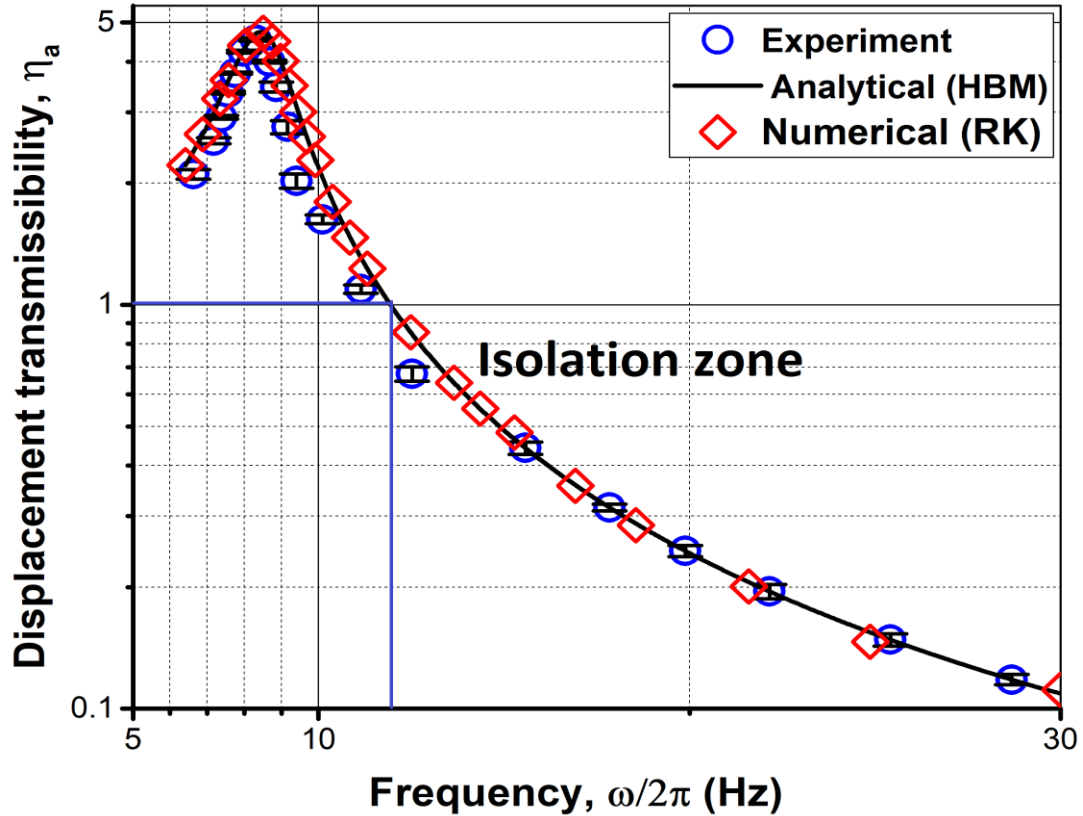


**Figure 24.** Measured and model simulation of displacement transmissibility of the vibration isolator versus frequency at acceleration level of  $0.25g$  [ $m\ s^{-2}$ ]. Model simulations are performed using Harmonic Balance Method (HBM) and 4<sup>th</sup> order Runge-Kutta (RK) numerical method.

As a result, agreement between HBM and Runge-Kutta models and measured data improved due to the absence of lateral vibrations. Thereby, Figure 23-24 suggests that a nonlinear vibration model that accounts for oscillations in multiple directions is needed to accurately capture the dynamic behavior of these types of vibration systems- especially at high level of accelerations. Additionally, at  $0.25g$  [ $m\ s^{-2}$ ] the cut-off frequency, where transmissibility drops to less than unity, decreased to approximately  $8.8$  [Hz] compared to  $12.5$  [Hz] at  $1.0\ g$  [ $m\ s^{-2}$ ]. This is mainly due to the hardening nonlinearities of the magnetic spring. At higher acceleration level, i.e.  $1.0\ g$  [ $m\ s^{-2}$ ], stiffness nonlinearity of

the magnetic spring manifest itself and causes a shift in frequency response towards higher values, i.e. hardening effects.

## **CHAPTER 4**

### **A DUAL PURPOSE VIBRATION ISOLATOR ENERGY HARVESTER: EXPERIMENT AND MODEL**

The current chapter discusses on theoretical and experimental study of an elastic-magnetic vibration isolation device. The author has used parts of the current chapter in the research article, “A dual purpose vibration isolator energy harvester “by S. M. Mahdi Mofidian and H. Bardaweel, published in Journal Mechanical Systems and Signal Processing, Volume 118 (2019) which is adapted with permission from ELSEVIER.

#### **4.1 Introduction**

Undesired vibrations and oscillations are the by-products from natural processes as well as human made structures and equipment. Examples of these vibrations include continuous or semi-continuous oscillations generated by highway bridges [1], human body motion [2, 5], and moving vehicles [3-6]. On one hand, some of these vibrations may cause severe damage to structures or obstruct their operations [7]. On the other hand, these vibrations represent free and abundant form of kinetic energy [13, 14]. As a result, dealing with these vibrations has grown in two main directions: vibration isolation [74,78, 93], and energy harvesting [12,94].

The literature on both vibration energy harvesting and vibration isolation is massive. Reviewing this massive literature is beyond the scope of this work. Nonetheless, energy from ambient vibrations has been successfully converted into useful electric

energy via electrostatic [95,96], piezoelectric [97], and electromagnetic transducers [98-100]. Recent advances and approaches in energy harvesting have been reviewed in Ref. [12,94]. Similarly, active and passive vibration control systems have been developed and thoroughly investigated over the past few decades [101,102]. A typical vibration isolation system uses a spring and a damper to prevent these oscillations from traveling between the source of vibrations and the isolated mass [8]. Using this spring-mass-damper system the kinetic energy from these oscillations is suppressed and dissipated into waste heat that is conducted away to the surrounding.

Continuous improvement in electronics manufacturing has led to deployment of low-power sensors and gadgets [103,104]. Nowadays, onboard sensing units are installed on equipment and structures to monitor their health conditions including temperature, pressure, stress, strain, humidity, corrosion, etc [1, 9, 11, 12, 105]. Thus, there has been growing interest in using the energy from these oscillations as power source replacing or complementing traditional batteries used to operate onboard sensors [17,106,108]. For instance, Davis and McDowell built a passive regenerative vibration isolation device using post-buckled beam as spring element and piezoelectric film as power conversion unit [17]. Their results showed that experimental transmissibility of 2% and harvested power of  $0.36 \mu\text{W}$  were achieved simultaneously. Similarly, Ali and Adhikari studied, theoretically, the performance of regenerative vibration absorber device supplemented with a piezoelectric stack for power recovery [19]. The study focused on modeling and design aspects of optimal design parameters using approximate fixed-point theory. Their study concluded that specific parameters of the energy harvester could lead to broadband harvesting combined with vibration absorption. In Ref. [20] the feasibility of integrating

vibration absorber with piezoelectric stack for power generation under random excitations was investigated using probabilistic linear random vibration theory. Results from this theoretical study showed that the recovered power increases with increase in the mass of structure. Moreover, a dual-purpose device was developed to isolate micro vibrations and harvest energy from micro-jitters of a cooler during satellite on-orbit operation [7]. The dual-purpose device was able to isolate the desired mass and recovered  $5.84 \mu\text{W}$  of vibration energy into electric energy. Also, a semi-active energy harvesting vibration suppression system using piezoelectric platform was proposed [107]. Tang and Zuo investigated the recovery of vibration energy from tall buildings using active tuned mass dampers and electromagnetic harvesters [21]. Furthermore, several studies investigated energy recovery from vehicle road interactions using regenerative vibration shock absorbers [6-9, 24, 108-110]. These studies focused on manufacturing of large scale regenerative hydraulic/pneumatic suspension systems that convert kinetic vibrational energy into hydraulic/pneumatic pressure and storing it in an accumulator [24, 108-110]. This hydraulic power was then used to run a hydraulic motor. For instance, a macro-scale hydraulic-electromagnetic vibration absorber capable of recovering energy from vehicle interaction with road was investigated by Fang et al. [24]. While energy losses from pipelines were significant the device was able to recover energy from vibrations. The authors of the study denoted that the energy recovery efficiency of their device decreased as the excitation frequency increased. Recent progress on regenerative vibration suppression systems for vehicles was reviewed by Zhang Jin-qiu et al. [106]

The work presented here is focused on developing a unique dual-purpose vibration isolation energy recovery system shown in Figure 25. While several studies

were focused on coupling small scale piezoelectric energy harvesting units with vibration isolation [17], the work presented here targets the use of elastic and magnetic elements to achieve the dual functionality of the device. The main purpose of the dual-purpose device is preventing vibrations from traveling through the isolated mass using magnetic and viscous dampers and elastic and magnetic springs. However, a secondary task of the dual-purpose device is converting some of the kinetic energy contained in these oscillations into useful electric charge, instead of waste heat, using magnetic levitation based energy harvester. Thus, another novel feature of the presented design is the use of an elastic mechanical spring along with a magnetic spring. As will be demonstrated in this article, this combination results in lower resonant frequency and desired nonlinearities. Additionally, unlike previous work [24, 108-110], the presented design is compact, light, and simple and does not require considerable added volume due to complex pipelines, accumulators, hydraulic motor, or oil tank [4, 106].

As shown in **Figure 25**, the presented device consists of a magnetic spring, mechanical flat spring, and dampers, i.e. viscous and magnetic dampers. The movement of the levitated magnet is guided and aligned using the mechanical flat spiral spring. Thus, an additional novel feature of the presented device is the reduced friction and wearing due to lack of direct contact between components. The isolated mass is connected to the mechanical and magnetic springs through a connecting rod. The rod passes through the top ring magnet while the bottom end of the rod is connected to the levitated magnet, as shown in **Figure 25**. A stationary coil is fixed around the rest position of the levitated magnet. Viscous damping effects are introduced via top and bottom orifices shown in **Figure 25**.

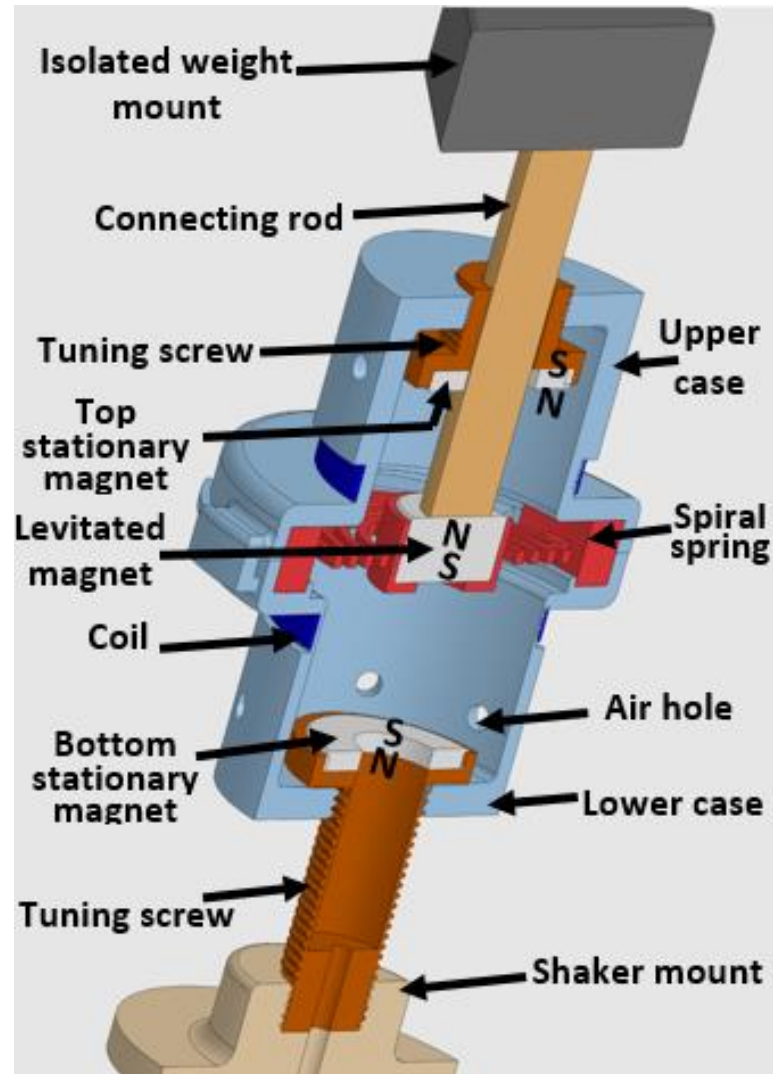


**Figure 25.** Overall design of the dual purpose vibration isolator energy harvester.

When the dual-purpose device is subject to external vibration, the levitated magnet moves vertically. Subsequently, the air inside the device chamber is forced through the orifices and around the levitated magnet mass. Moreover, as the levitated magnet moves, voltage is induced in the coil. As a result, the kinetic energy from the vibrations is converted into electric energy. Magnetic damping is generated as a result of eddy currents induced in the coil because of variation in magnetic flux as the levitated magnet is displaced [85]. Thus, energy dissipation in the dual-purpose device is achieved

through a combination of viscous damping due to airflow, and magnetically-induced damping due to levitated magnet movement inside the coil. The damping (viscous and magnetic) and stiffness (mechanical and magnetic spring) form the platform for vibration isolation. Simultaneously, the levitated magnet movement inside the coil forms the base for converting the kinetic energy of vibrations into electric charge.

## 4.2 Modeling

**Figure 26** shows a mechanical lumped parameter model schematic of the dual-purpose vibration isolator energy harvester device. The moving levitated magnet inside the dual-purpose device is modeled as a single-degree-of-freedom system with effective mass,  $m$ , displaced vertically with relative displacement,  $\chi = x - y$ . The fixed and levitated magnets generate repulsive restoring force that can be represented using linear,  $K_{m1}$ , and nonlinear,  $K_{m3}$ , stiffness coefficients, respectively. Likewise,  $K_{ss}$  represents a linear stiffness coefficient of the mechanical spring restoring force. The linear,  $K_{m1}$  and  $K_{ss}$ , and nonlinear  $K_{m3}$  stiffness coefficients are obtained using both experiment and COMSOL finite element analysis. Here, it is assumed that viscous damping due to air flow through the orifices and magnetic damping due to eddy currents induced in the coil are the two major sources responsible for energy dissipation and their damping coefficients are given by  $C_a$  and  $C_m$ , respectively. The equation of motion for the described dual-purpose device, is given by

$$m\ddot{\chi} + C_a(\dot{\chi} - \dot{y}) + C_m(\dot{\chi} - \dot{y}) + K_{ss}(x - y) + K_{m1}(x - y) + K_{m3}(x - y)^3 = 0 \quad \text{Eq. (34)}$$

The equation of motion (34) can be further simplified by subtracting  $m\ddot{y}$  from both sides of Eq. (34) and substituting  $\ddot{\chi} = \ddot{x} - \ddot{y}$ ,  $\dot{\chi} = \dot{x} - \dot{y}$  and  $\chi = x - y$

$$\ddot{\chi} + c_1\dot{\chi} + K_1\chi + K_3\chi^3 = -m\ddot{y} \quad \text{Eq. (35)}$$

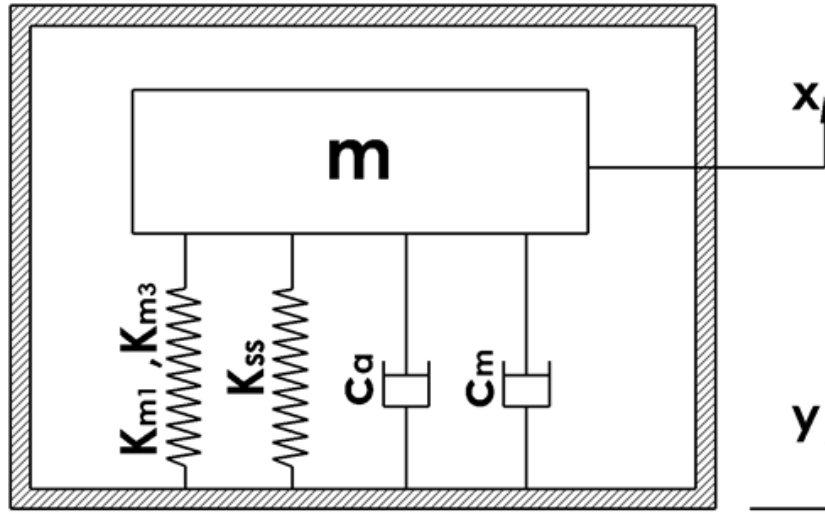


**Figure 26.** Model schematic of the single DOF dual-purpose vibration isolator energy harvester.

where  $(\ddot{\chi})$  and  $(\dot{\chi})$  represent the second and first time derivatives, i.e. acceleration and velocity, respectively. Additionally, the lumped parameter,  $c_1$ , represents total damping of the system as a result of viscous and magnetic damping, i.e.  $c_1 = c_a + c_m$ , while linear stiffness coefficients,  $K_s$  and  $K_{m1}$ , are lumped into parameter,  $K_1 = K_{ss} + K_{m1}$  and  $K_3 = K_{m3}$ .

#### 4.2.1 Modeling displacement transmissibility using Harmonic Balance Method

The dynamic model described in Eq. (35) represents a nonlinear Duffing-type oscillator [111]. Direct numerical integration [112], the method of multiple scales [113-115], or the harmonic balance method coupled with an asymptotic numerical method [116,117], have been used to solve Duffing nonlinear equation of motion. In this work Harmonic Balance Method (HBM) is used to solve the system described in Eq. (35). For

harmonic base-excitation  $y = A \sin(\omega t + \varphi)$  and using  $\bar{\chi} = \frac{\chi}{A}$ ,  $\omega_n = \sqrt{\frac{K_1}{m}}$ ,  $\alpha = \frac{K_3 A^2}{m\omega_n^2} =$

$\frac{K_3 A^2}{k_1}$ ,  $\Omega = \frac{\omega}{\omega_n}$ ,  $\tau = \omega_n \cdot t$ , the non-dimensional equation of motion becomes

$$\bar{\chi}'' + 2\xi_1 \bar{\chi}' + \bar{\chi} + \alpha \bar{\chi}^3 = \Omega^2 \sin(\Omega\tau + \varphi) \quad \text{Eq. (36)}$$

where  $A$  and  $\varphi$  are amplitude and phase, respectively. Here,  $(\blacksquare)' = \frac{d}{d\tau}(\blacksquare)$ ,  $(\blacksquare)'' =$

$\frac{d^2}{d\tau^2}(\blacksquare)$  are the non-dimensional velocity and acceleration of the effective mass defined

as  $\bar{\chi}' = \dot{\chi}/A\omega_n$ ,  $\bar{\chi}'' = \ddot{\chi}/A\omega_n^2$ , respectively, and,  $\xi_1 = \frac{c_1}{2m\omega_n}$ . Assuming that higher

order harmonics are negligible and the dynamic response of the oscillator is dominated

by the first harmonic of amplitude, the solution becomes

$$\bar{\chi}(\tau) = \bar{X} \sin(\Omega\tau) \quad \text{Eq. (37)}$$

Substituting Eq. (37) and its non-dimensional derivatives  $\frac{d}{d\tau}(\blacksquare)$  and  $\frac{d^2}{d\tau^2}(\blacksquare)$  into Eq. (36)

yields

$$\begin{aligned} -\Omega^2 \bar{X} \sin(\Omega\tau) + 2\xi_1 \Omega \bar{X} \cos(\Omega\tau) + \bar{X} \sin(\Omega\tau) + \alpha \bar{X}^3 \sin^3(\Omega\tau) \\ = \Omega^2 \sin(\Omega\tau + \varphi) \end{aligned} \quad \text{Eq. (38)}$$

Applying trigonometric relations and taking up to the first harmonic term yields

$$\sin^3(\Omega\tau) = \left( \frac{-\sin(3\Omega\tau)}{4} + \frac{3\sin(\Omega\tau)}{4} \right) \approx \frac{3}{4} \sin(\Omega\tau) \quad \text{Eq. (39)}$$

Further, substituting Eq. (39) into Eq. (38) results in

$$\begin{aligned} -\Omega^2 \bar{X} \sin(\Omega\tau) + 2\xi_1 \Omega \bar{X} \cos(\Omega\tau) + \bar{X} \sin(\Omega\tau) + \frac{3}{4} \alpha \bar{X}^3 \sin(\Omega\tau) \\ = \Omega^2 [\sin(\Omega\tau) \cos(\varphi) + \cos(\Omega\tau) \sin(\varphi)] \end{aligned} \quad \text{Eq. (40)}$$

Equating the coefficients of  $\sin(\Omega\tau)$  and  $\cos(\Omega\tau)$  in Eq. (40) results in

$$[\bar{X} - \Omega^2 \bar{X} + \frac{3\alpha}{4} \bar{X}^3] = \Omega^2 \cos(\varphi) \quad \text{Eq. (41-a)}$$

$$2\xi_1 \Omega \bar{X} = \Omega^2 \sin(\varphi) \quad \text{Eq. (41-b)}$$

Further simplification yields

$$[\bar{X} - \Omega^2 \bar{X} + \frac{3\alpha}{4} \bar{X}^3]^2 + [2\xi_1 \Omega \bar{X}]^2 = \Omega^4 \quad \text{Eq. (42)}$$

Using the absolute displacement of the payload mass, i.e.  $x = A\bar{X}\sin(\Omega\tau) + y$

the absolute displacement transmissibility ratio,  $\eta_a$ , is given by

$$\eta_a = \left| \frac{x}{y} \right| = \left| \frac{A(\bar{X}\sin(\Omega\tau) + \sin(\Omega\tau + \varphi))}{A} \right| = \sqrt{1 + \bar{X}^2 + 2\bar{X}\cos(\varphi)} \quad \text{Eq. (43)}$$

Substituting Eq. (41-a) into Eq. (43), the absolute transmissibility ratio,  $\eta_a$ , can be further simplified to

$$\eta_a = \sqrt{\frac{\Omega^2 + \bar{X}^2(2 - \Omega^2) + \frac{3\alpha}{2}\bar{X}^4}{\Omega^2}} \quad \text{Eq. (44)}$$

#### 4.2.2 Model estimation of induced voltage and harvested power

Using the velocity solution,  $\dot{\chi}$  from Eq. (35), induced voltage,  $V$ , and output power harvested using the dual-purpose device,  $P$ , across a load resistance,  $R_{Load}$ , are given by

$$V = \frac{BNl \dot{\chi}}{R_{coil} + R_{Load}} R_{Load} \quad \text{Eq. (45)}$$

$$P = \left( \frac{BNl \dot{\chi}}{R_{coil} + R_{Load}} \right)^2 R_{Load} \quad \text{Eq. (46)}$$

Where  $R_{coil}$  is coil resistance,  $l$  is the length of the coil per turn,  $N$  is the number of coil turns, and  $B$  is the average magnetic flux density in the air gap between the moving magnet mass and the coil.

### 4.3 Experiment and model validation

The main objective of the experiment is to validate the theoretical model and investigate the ability of the device to, simultaneously reduce vibration transmissibility and generate electric power. To achieve this goal, a prototype of the dual-purpose vibration isolator energy harvester is manufactured. **Figure 27** shows the major components of the dual-purpose device obtained using additive manufacturing. **Table III** lists dimensions and properties of the manufactured dual-purpose device. First, the top and bottom casings and the mechanical spring were printed using Polylactic acid (PLA) thermoplastic filament and Thermoplastic Poly-Urethane (TPU) rubber-like filament, respectively. Neodymium iron boron (NdFeB) ring magnets were fixed on the top and bottom parts of the device as shown in **Figure 27**.

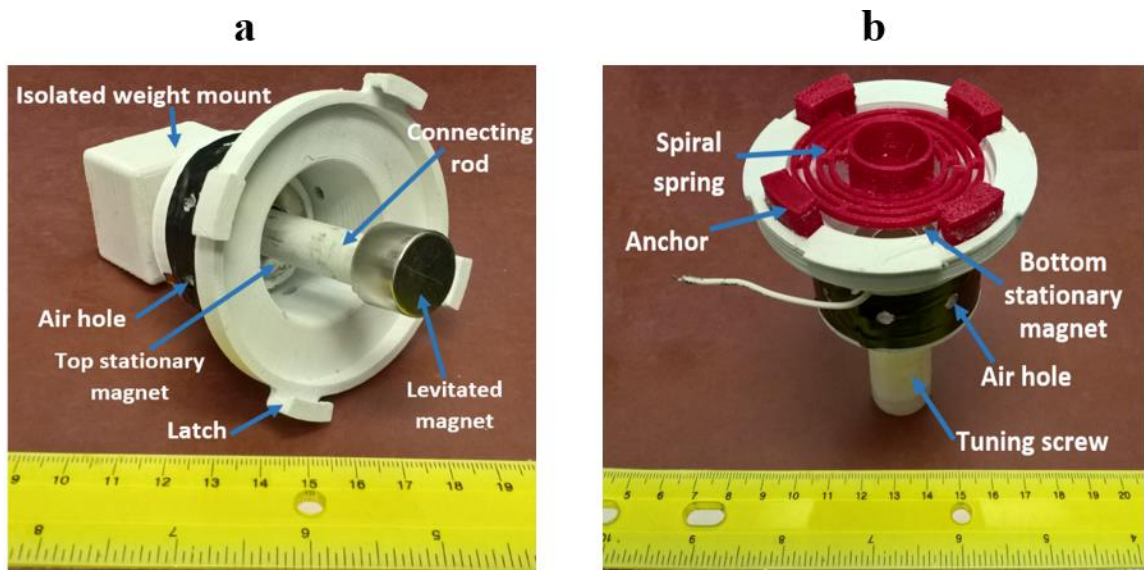


**Figure 27.** Main parts of the dual-purpose device: a) Top part (Left) and b) Bottom part (Right).

The mechanical spring was anchored inside the slots of the bottom part. The solid magnet was then centered inside the mechanical spring in a repulsive arrangement with respect to top and bottom ring magnets.

**Table III.** Geometric and material properties of the fabricated dual-purpose device.

| Parameter  | Properties                        |
|--|-----------------------------------|
| Coil resistance ( $R_{\text{coil}}$ ) [ $\Omega$ ]                                   | 1280                              |
| Load resistance ( $R_{\text{Load}}$ ) [ $\Omega$ ]                                   | 900                               |
| Coil turns   | 2000                              |
| Coil material  | Copper, 40 AWG                    |
| Levitated magnet size (height $\times$ diameter) [mm]                                | 12.7 $\times$ 19.05               |
| Levitated magnet material  | NdFeB-N42                         |
| Stationary magnet size (Outer diameter $\times$ Inner diameter $\times$ height) [mm] | 2.54 $\times$ 12.7 $\times$ 3.175 |
| Stationary magnet material   | NdFeB-N42                         |
| Device casing size (height $\times$ outer diameter) [mm]                             | 81.5 $\times$ 80.5                |
| Air hole diameter [mm]   | 3.8                               |
| Isolated mass (kg)   | 0.2                               |
| Mechanical spring material   | Thermoplastic poly-Urethane (TPU) |
| Casing material  | Polylactic acid (PLA)             |

The bottom and top ends of the connecting rod were glued to the levitated magnet and the isolated object mount, respectively. Lastly, 40 AWG copper coil was placed around the equilibrium position of the levitated magnet. The fully assembled device was

obtained by locking the top and bottom casings together using the latches as shown in **Figure 28**.

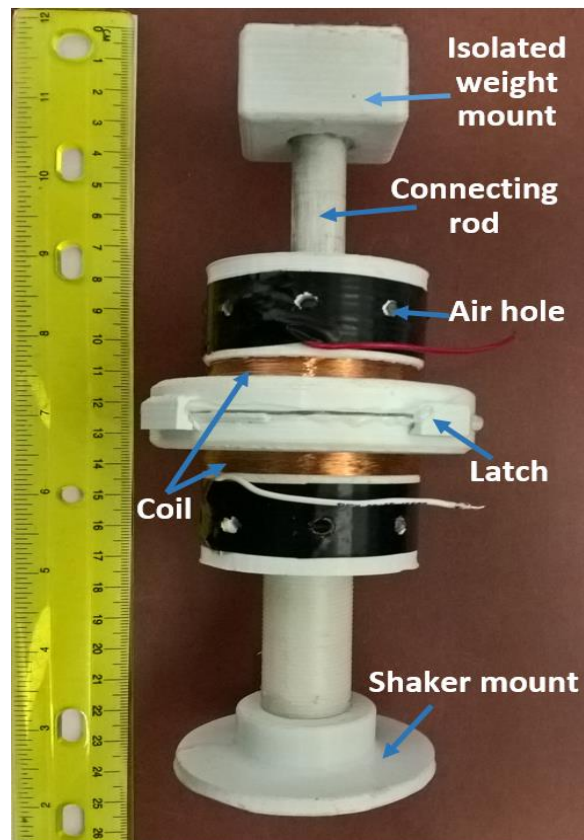


**Figure 28.** Fully assembled dual-purpose vibration isolator energy harvester device.

#### 4.3.1 Magnetic restoring force

The repulsive force developed between the top and bottom fixed magnets and levitated magnet was obtained using experiment and COMSOL software. The experiment setup used to measure the repulsive magnetic force is shown in **Figure 29**. The experiment apparatus consists of test stand (SHIMPO FGS-250W), displacement sensor (KEYENCE IL-100), and digital force sensor (SHIMPO FG-3006). Both displacement and force readings were recorded using data acquisition system (NI

myDAQ) and stored on a PC. A COMSOL model was developed in order to estimate the magnetic flux density,  $B$ , as the levitated magnet was swept vertically between the two stationary magnets.

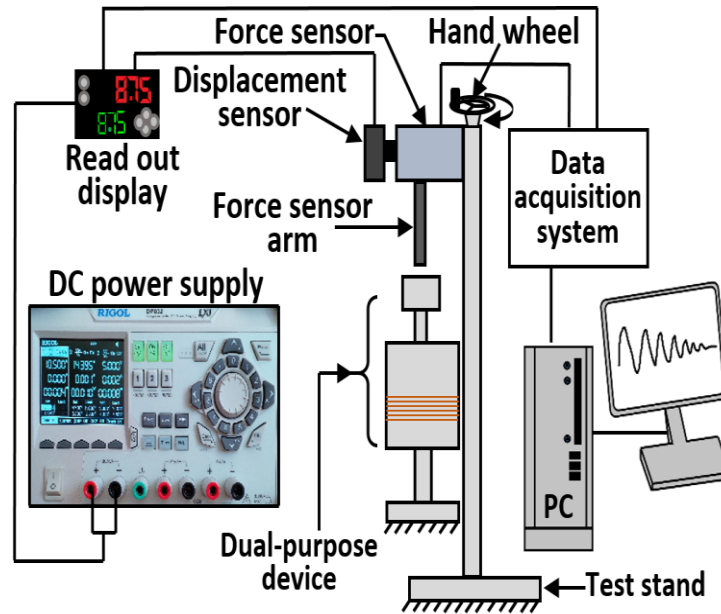


**Figure 29.** Schematic of experimental apparatus used for characterization of mechanical and magnetic springs.

**Figure 30** shows COMSOL simulation of magnetic flux density,  $B$ , at three coil positions at  $\chi = 0$  mm during levitated magnet sweeping between the two stationary magnets. The three locations represent the inner ( $r_{inner} = 22$  mm), mid-way ( $r_{middle} = 22.6$  mm), and outer ( $r_{outer} = 23.3$  mm) layers of the coil. The obtained average magnetic flux densities,  $B$ , versus displacement,  $\chi$ , at these three different positions are shown in Figure 31. Slight variation in the average magnetic flux density at these three locations is evident. That is, the magnetic flux density became stronger towards the levitated magnet, i.e. ( $r_{inner} = 22$  mm). Thus, in this work, the average flux density of the middle coil ( $r = 22.6$  mm) was used to perform voltage,  $V$ , and power,  $P$ , calculations given by (45) and (46),

respectively. The average flux density shown in Figure 31 was fitted to a sine summation function [117] and given by

$$B \cong \sum_{i=1}^8 a_i \sin(b_i \chi + c_i) \quad \text{Eq. (47)}$$

where  $a_i$ ,  $b_i$ , and  $c_i$  are the magnetic flux density constants obtained from curve fitting and given in **Table IV**.

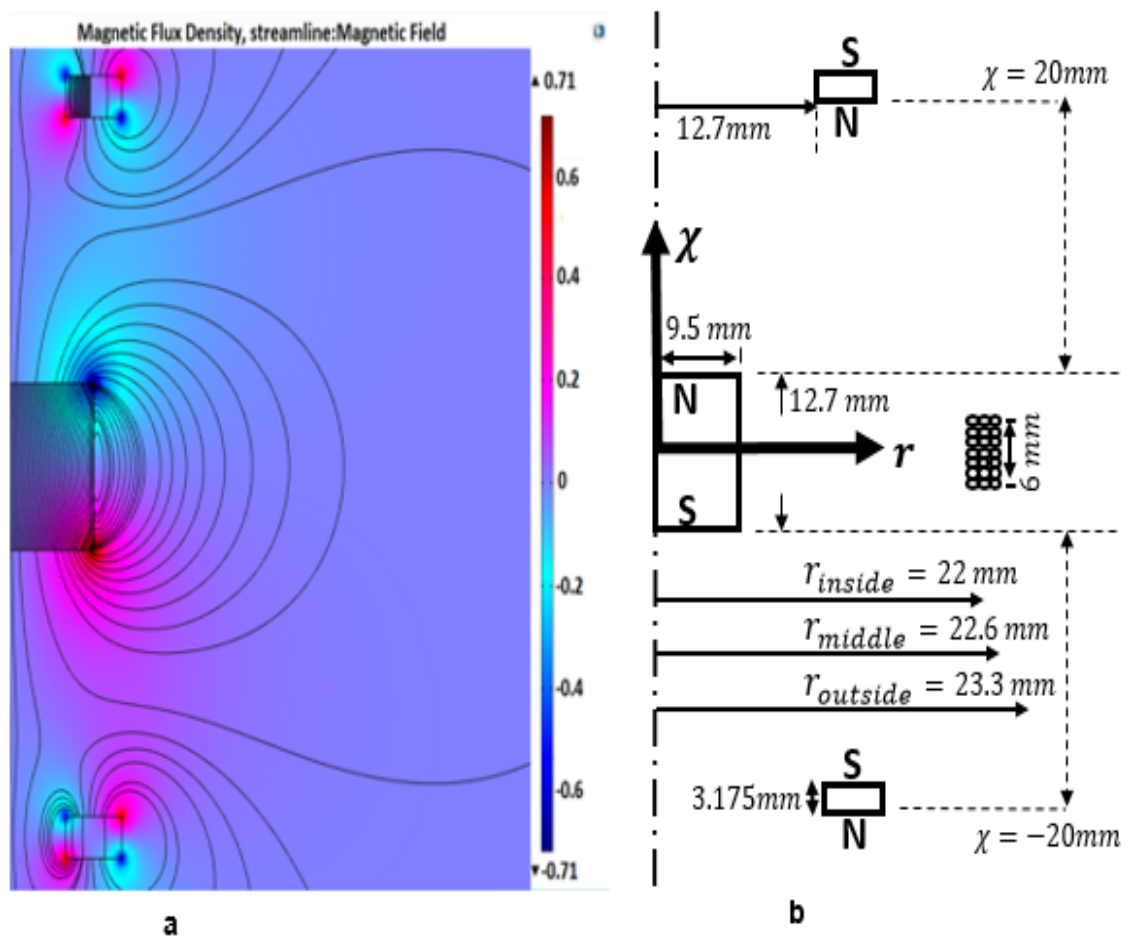


**Figure 30.** COMSOL model of the three magnets arrangement: a) The Levitated solid magnet sweeping between the two stationary top and bottom ring magnets (Left) and b) Three magnets arrangement, dimensions, and geometries (Right).

**Table IV.** Summation of sin function coefficients of fitted curve for the magnetic flux density,  $B$ .

|                     |                  |                     |                   |
|---------------------|------------------|---------------------|-------------------|
| $a_1 = 0.03026$     | $a_2 = 0.004159$ | $a_3 = 0.003037$    | $a_4 = 0.001898$  |
| $a_5 = 0.001071$    | $a_6 = 0.000515$ | $a_7 = 0.000318$    | $a_8 = 3.45e - 5$ |
| $b_1 = 163.4$       | $b_2 = 332.2$    | $b_3 = 502.8$       | $b_4 = 673.5$     |
| $b_5 = 829.2$       | $b_6 = 1026$     | $b_7 = 1231$        | $b_8 = 1520$      |
| $c_1 = 5.063 e - 5$ | $c_2 = -3.141$   | $c_3 = -2.167e - 3$ | $c_4 = 3.143$     |
| $c_5 = 0.001205$    | $c_6 = 3.127$    | $c_7 = -7.962e - 3$ | $c_8 = -3.065$    |

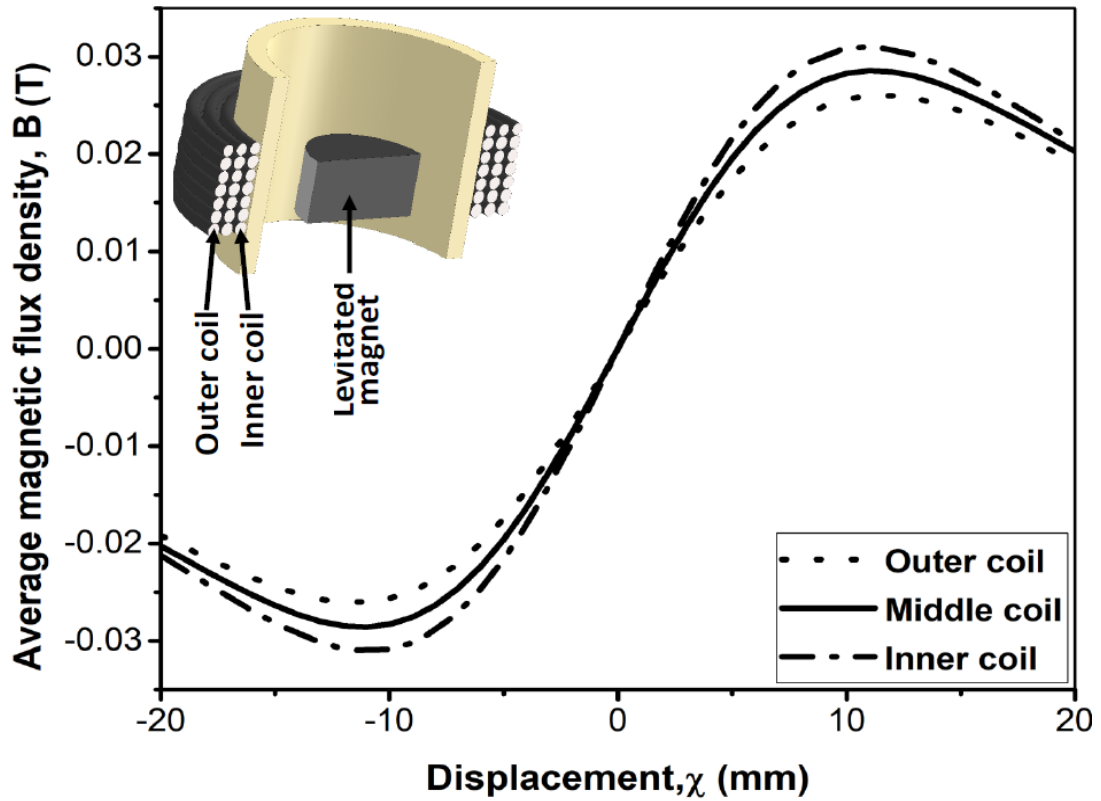


**Figure 31.** COMSOL simulation results of magnetic flux density,  $B$  estimated at inner, middle and outer coils.

The measured and COMSOL modeled magnetic force,  $F_{mag}$ , is shown in Figure 32. Good agreement between simulation results and measured data is evident. The load-deflection curve exhibits nonlinear restoring force behavior. This indicates a nonlinear stiffness behavior of the magnetic spring, thus, leading to a non-resonant Duffing-type energy harvesting scheme.

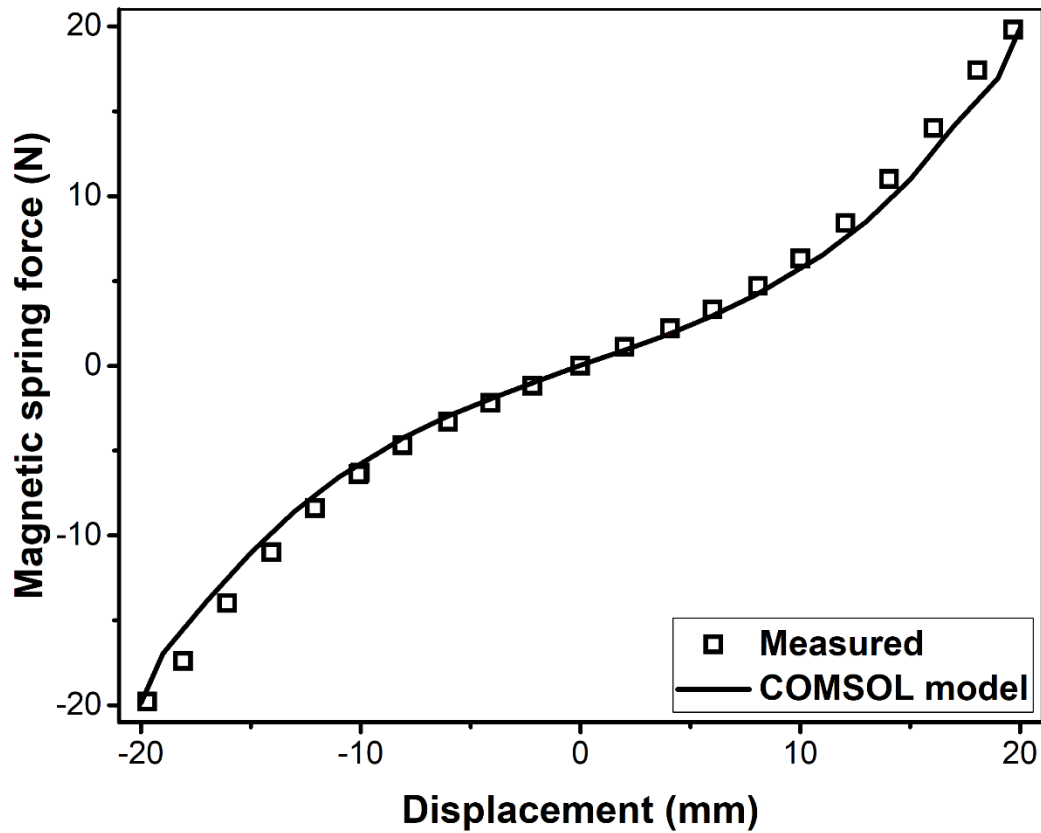


**Figure 32.** Load-deflection curve of the magnets arrangement used in dual-purpose device.

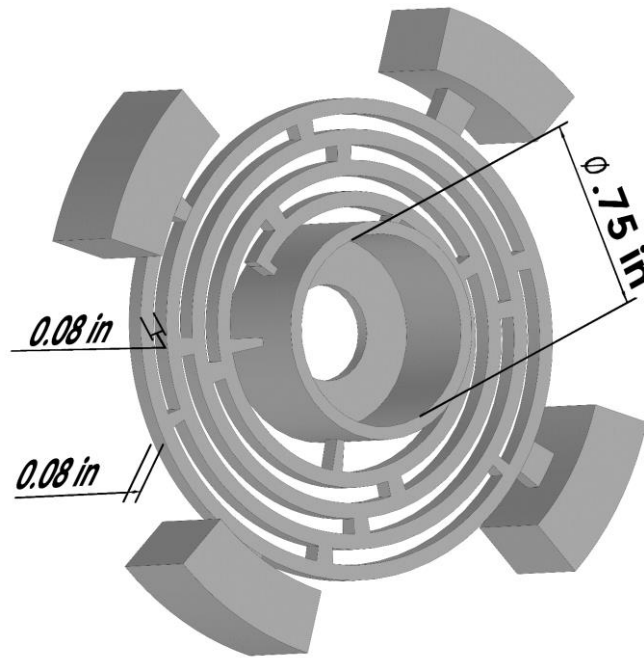
The nonlinear load-deflection curve was curve-fitted to a higher order polynomial, i.e.  $K_{m1}\chi + K_{m3}\chi^3$ . These linear and nonlinear magnetic spring stiffness coefficients i.e.  $K_{m1}$  and  $K_{m3}$ , respectively, are given in **Table V**.

**Table V.** Measured stiffness coefficients for the magnetic spring.

| Coefficient | Value                          |
|-------------|--------------------------------|
| $K_{m3}$    | 1.368e+06 [N m <sup>-3</sup> ] |
| $K_{m1}$    | -70.22 [N m <sup>-1</sup> ]    |

#### 4.3.2 Mechanical spring restoring force

Characterization of the mechanical spring was performed using experiment setup shown in **Figure 29** and COMSOL software. As shown in **Figure 33**, the spring is made of a central socket that is connected to spiral arm to support loads along the longitudinal axis.

**Figure 33.** 3D cartoon schematic of the mechanical spring design used in this work.

The levitated magnet is tightly fit inside the socket and a set of bridges across the spiral arm is used to prevent the levitated magnet from tilting along the transverse plane. Figure 34 shows the load-deflection curve obtained for the spring using COMSOL solid mechanics interface under the Structural Mechanics module. **Figure 34** also shows the load-deflection curve measured experimentally using the apparatus shown in **Figure 29**. Results from COMSOL simulations are in good agreement with measured data.

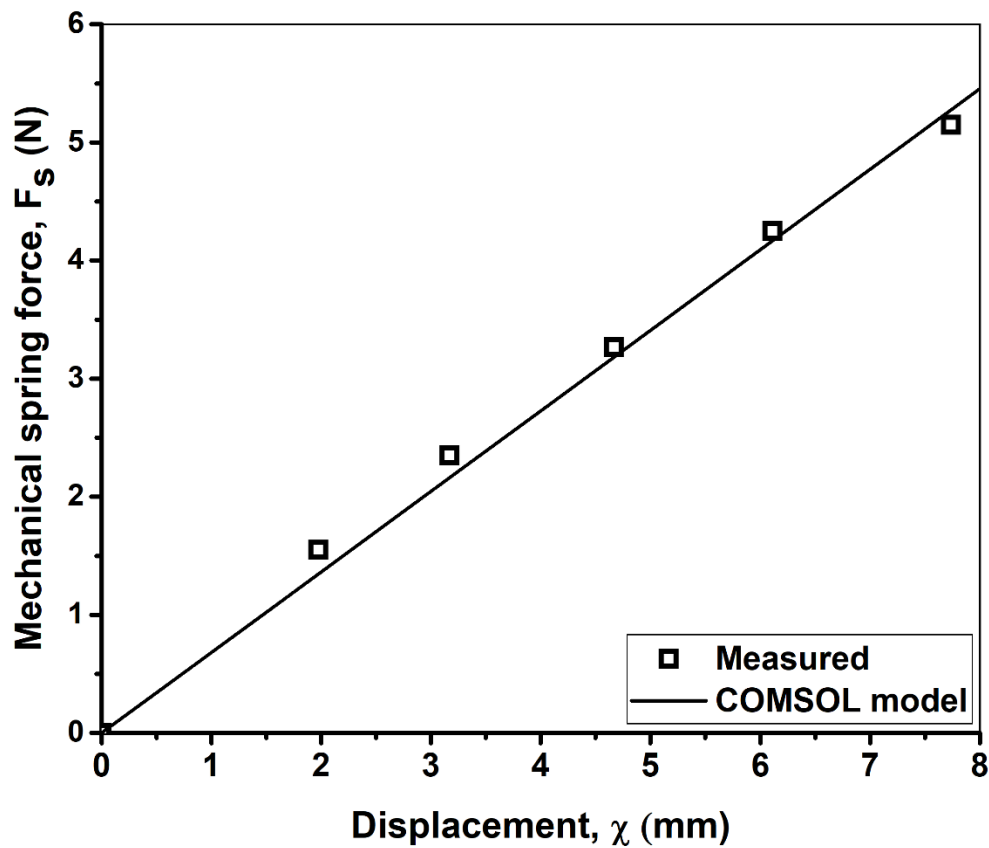


**Figure 34.** Load-deflection curve of the mechanical spring used in dual-purpose device.

As shown in **Figure 34**, the mechanical spring design adopted in this work exhibits linear behavior with a positive stiffness coefficient,  $K_{SS}$ . Both experiment and model reveal linear stiffness coefficients,  $K_{SS}$  of approximately  $688.8 \text{ [N m}^{-1}\text{]}$  and  $681.8$

[N m<sup>-1</sup>], respectively. Nonetheless, the magnetic spring exhibits a negative linear stiffness coefficient of approximately  $K_{m1} = -70.2$  [N m<sup>-1</sup>]. Thus, as stated earlier, another advantage of the presented design is its ability to reduce the overall stiffness, i.e.  $K_1 = K_{ss} + K_{m1} = 618.6$  [N m<sup>-1</sup>] and resonant frequency of the dual-purpose device.

#### 4.3.3 Vibration isolation and energy harvesting

The dual functionality of the presented device was tested using experiment setup shown in **Figure 35**. The setup consists of a shaker table (VT-500, SENTEK DYNAMICS), power amplifier (LA-800, SENTEK DYNAMICS), vibration controller (S81B-P02, SENTEK DYNAMICS), two accelerometers (PCB333B30 model, PCB Piezotronics), data acquisition system (NI myDAQ), and a PC.

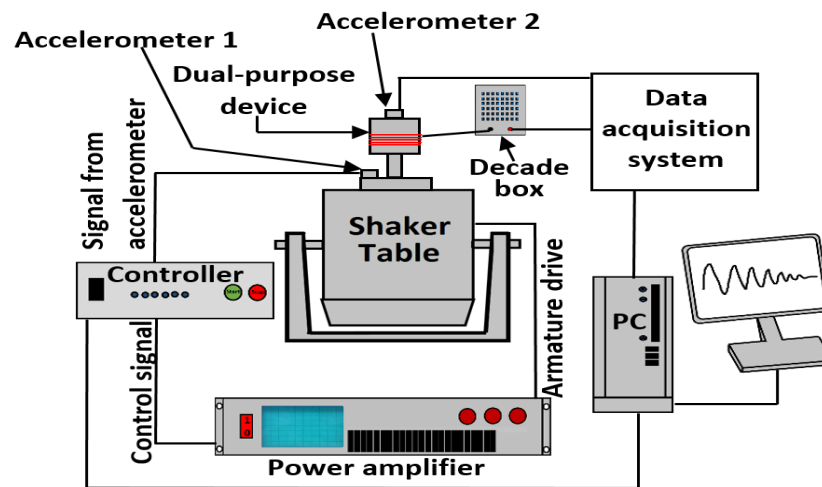


**Figure 35.** Schematic of experimental apparatus used for dynamic characterization of the dual-purpose device.

The dual-purpose device was securely mounted on the shaker table top, and its response was measured at predetermined frequencies, i.e. 7-30 [Hz] and accelerations, i.e. 0.25 g and 1 g [m/s<sup>2</sup>]. The voltage output from the dual-purpose device and the

acceleration level transmitted to the isolated object were simultaneously measured. Induced voltage was measured across a load resistance using decade box (GLOBAL SPECIALTIES RDB-10).

Upon dynamic characterization of the dual-purpose vibration isolator energy harvester resonant frequency,  $\omega_n$ , and total damping,  $c_1$ , were estimated. While the dual-purpose device was held firmly in place, the levitated magnet was brought to a predetermined height and then released. In this experiment no external excitation was applied, and therefore, the dual-purpose device acted as damped un-driven oscillator. The obtained ring-down waveform was then used to estimate resonant frequency,  $\omega_n$ , and damping,  $c_1$ , using the logarithmic decrement method [93,94]. The estimated resonant frequency and total damping of the dual-purpose device were approximately, 55.6 [Rad s<sup>-1</sup>], i.e. 8.85 [Hz] and 2.44 [N s<sup>-1</sup>.m<sup>-1</sup>], respectively. This total damping,  $c_1 = c_a + c_m$  is split into  $c_a = 2.389$  [N. $\frac{s}{m}$ ] and  $c_m = 0.051$  [N. $\frac{s}{m}$ ] where, assuming uniform magnetic flux density [59, 89], the magnetic damping is given by  $c_m = \frac{(NB)^2}{R_{coil}+R_{Load}}$  [59]. These measured values were used in model simulations to evaluate performance of the device.

Next, the apparatus shown in **Figure 35** was used to investigate the frequency response of the dual-purpose device. As part of the dynamic characterization of the dual-purpose device, both displacement transmissibility,  $\eta_a$ , and voltage induced in the coil,  $V$ , were measured. Figure 36a-b shows measured absolute displacement transmissibility,  $\eta_a$ , of the dual-purpose device at two different accelerations, i.e. 0.25 g and 1.0 g [m/s<sup>2</sup>], respectively. The low resonant frequency of the dual-purpose device is evident. This is due to the positive and negative stiffness of the mechanical spiral spring and magnetic spring, respectively. Figure 36a-b compares model predictions of displacement

transmissibility,  $\eta_a$ , against measured data. In addition to model simulation using HBM described in (44), a fourth order Runge-Kutta numerical solution was obtained and verified against measured data. Close agreement between model predictions and measured data is evident at 0.25 g [ $\text{m/s}^2$ ]. In general, at both accelerations, 0.25 g and 1.0 g [ $\text{m/s}^2$ ], experiment and models show similar trends. Numerical simulations are in close agreement with results from HBM. Nonetheless, at higher acceleration, i.e. 1.0 g [ $\text{m/s}^2$ ] both Runge-Kutta numerical model and HBM analytical model slightly deviate from experiment with maximum shifts from measured data approximately 1.2 [Hz]. This discrepancy at higher acceleration levels may be attributed to the presence of nonlinear damping [79], experimental error [81, 61], or presumably the experiment apparatus does not completely resemble a single degree of freedom system as assumed in our models [81]. Additionally, in Ref. [82] similar mismatch between model predictions and measured data was observed and attributed to wobbling and lateral vibration. This is especially true in this work because the mismatch grew at higher acceleration, i.e. 1.0 g [ $\text{m/s}^2$ ] and lateral vibrations were observed at this acceleration during the experiment. As a result, this lateral motion triggers other modes of vibrations that are not accounted for in the presented model. This is because the model we present here accounts only for vertical displacement. In Figure 36a-b transmissibility of the dual-purpose device drops to less than unity, i.e.  $\eta_a < 1$ , at corresponding frequencies,  $\omega = 11.9$  and 12.5 [Hz] at 0.25 g and 1.0 g [ $\text{m/s}^2$ ], respectively. This slight shift in frequency at higher excitation levels is due to hardening effects. As the excitation levels increased, hardening effects became more apparent due to stiffness nonlinearity manifesting itself, which led to shift in frequency response of the dual-purpose device.

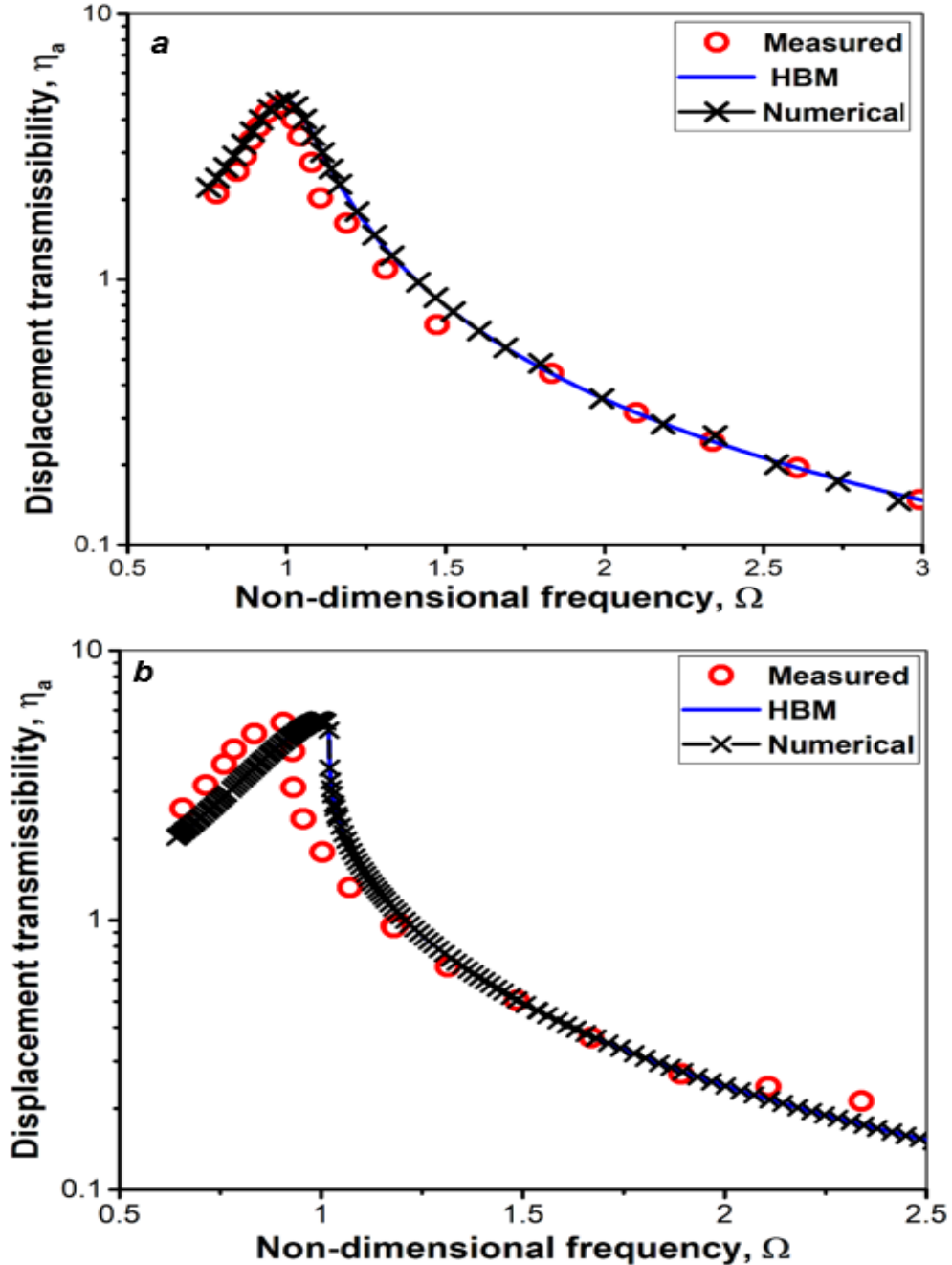


**Figure 36.** Displacement transmissibility of the dual-purpose vibration isolator energy harvester at a)  $0.25g$  [ $m\ s^{-2}$ ] (TOP) and b)  $1g$  [ $m\ s^{-2}$ ] (BOTTOM) obtained from experiment and models.

**Figure 37a-b** demonstrates the ability of the dual-purpose device to produce voltage during the dynamic operation at  $0.25\ g$  and  $1.0\ g$  [ $m/s^2$ ], respectively. Voltage,  $V$ , and displacement transmissibility,  $\eta_a$ , measurements were taken simultaneously, under

the same conditions. Hardening effects and nonlinear behavior become evident at higher acceleration, i.e.  $1.0 \text{ g [m/s}^2]$ . At this acceleration, results show a gradual increase in output voltage until  $\Omega = 1$ . This is then followed by a sharp drop in frequency response of the dual-purpose device. This is a unique characteristic of nonlinear Duffing-type oscillators known as frequency jump [87, 118]. The voltage shown in **Figure 37** was measured across a load resistance,  $R_{Load} = 900 \text{ [\Omega]}$ .

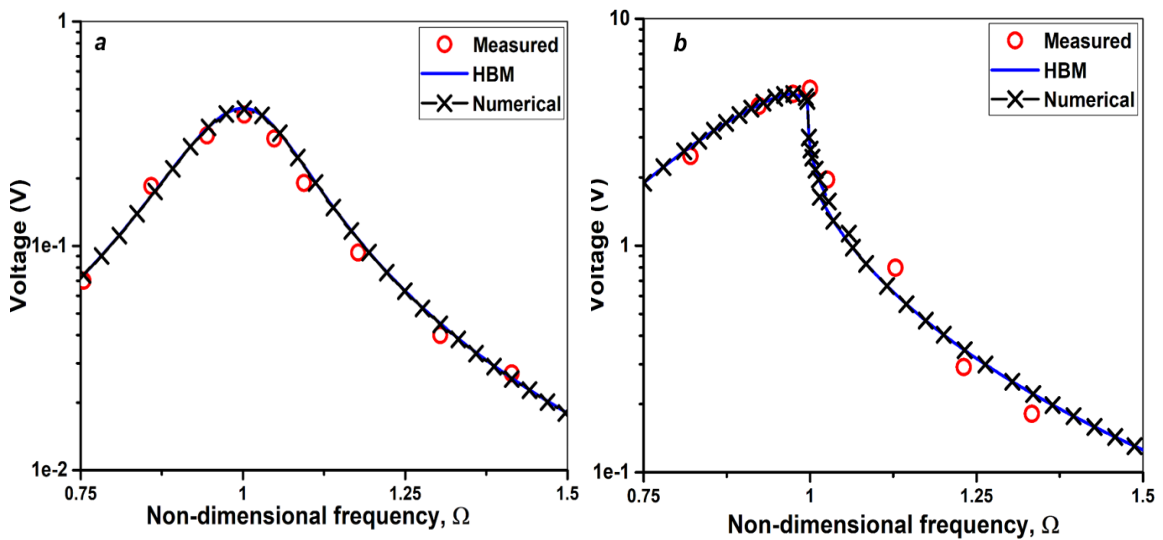


**Figure 37.** Output voltage from the dual purpose vibration isolator energy harvester at a)  $0.25 \text{ g [m s}^{-2}]$  (TOP) and b)  $1 \text{ g [m s}^{-2}]$  (BOTTOM) obtained from experiment and models.

**Figure 38a-b** shows output power,  $P$ , produced by the dual-purpose device. The power produced by the device when transmissibility dropped to unity, i.e.  $\eta_a = 1$ , was approximately  $0.115 \text{ [mW]}$  at  $1.0 \text{ g [m/s}^2]$ . This demonstrates the ability of the proposed device to simultaneously isolate the mass and harvest energy from these vibrations. The power produced by the dual-purpose device was significantly higher than the power recovered by comparable regenerative devices reported in [7] i.e.  $5.84 \text{ }\mu\text{W}$  and [10, 17], i.e.  $0.36 \text{ }\mu\text{W}$ . It is worth noting that the main purpose of this article is proof-of-concept

testing and demonstrating the ability of the dual-purpose device to simultaneously isolate vibrations and scavenge some of these vibrations. This has been achieved in this work.

Nonetheless, design improvement and parametric study are discussed next.

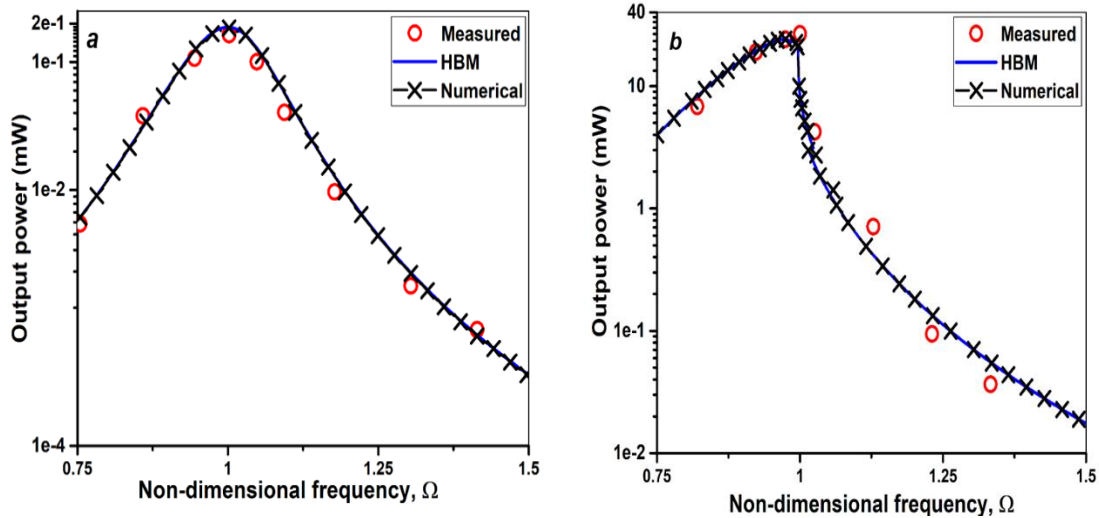


**Figure 38.** Electric output power recovered by the dual-purpose vibration isolator energy harvester at a)  $0.25\text{g}$  [ $\text{m s}^{-2}$ ] (TOP) and b)  $1\text{g}$  [ $\text{m s}^{-2}$ ] (BOTTOM) obtained from experiment and models.

#### 4.4 Model simulation and parametric study

A series of simulation studies was performed in order to assess the performance of the dual-purpose device in response to change in system parameters. Specifically, linear stiffness,  $K_1$ , nonlinear stiffness,  $K_3$ , load resistance,  $R_{Load}$ , and damping,  $\xi_1$ , design parameters were varied while other design parameters were held fixed at nominal values measured experimentally. **Figure 39a-d** shows the sensitivity of transmissibility and output power from the dual-purpose device in response to variation in linear stiffness coefficient,  $K_1$  at  $0.25\text{ g}$  and  $1.0\text{ g}$  [ $\text{m/s}^2$ ], respectively. Results reveal that decreasing the linear stiffness coefficient,  $K_1$ , lowers the cut-off frequency where transmissibility drops to unity, i.e.  $\eta_a = 1$ . This is because lower stiffness coefficient,  $K_1$ , reduces the resonant

frequency of the dual-purpose device by shifting its frequency response to the left. This indicates that for a fixed frequency beyond cut-off frequency, decreasing the linear stiffness coefficients,  $K_1$ , can potentially reduce transmissibility but also lowers output power. Additionally, decreasing the linear stiffness coefficient,  $K_1$ , results in higher power output at  $\eta_a = 1$ . For instance, at  $1.0 \text{ g [m/s}^2\text{]}$  reducing the linear stiffness coefficient from  $K_1 = 900 \text{ N.m}^{-1}$  to  $K_1 = 300 \text{ N.m}^{-1}$  lowers the cut-off frequency from  $14.61 \text{ [Hz]}$  to  $8.9 \text{ [Hz]}$  and increases output power from  $0.06 \text{ [mW]}$  to  $0.99 \text{ [mW]}$ , respectively. The unique design of the presented dual-purpose device makes it possible to achieve this desired characteristic by altering the positive and negative stiffness values for the mechanical spring and magnetic spring, respectively. Moreover, results from **Figure 39** reveal that a higher excitation level shifts the cut-off frequency slightly. For example, for a fixed linear stiffness coefficient,  $K_1 = 500 \text{ N.m}^{-1}$ , the cut-off frequency increases from  $10.73 \text{ [Hz]}$  to  $11.04 \text{ [Hz]}$  when the acceleration is increased from  $0.25 \text{ g}$  to  $1.0 \text{ g [m/s}^2\text{]}$ , respectively. This is presumably due to hardening effects appearing at higher level of excitation. Nonetheless, this little increase in cut-off frequency is accompanied by improved energy harvesting characteristics at higher accelerations.

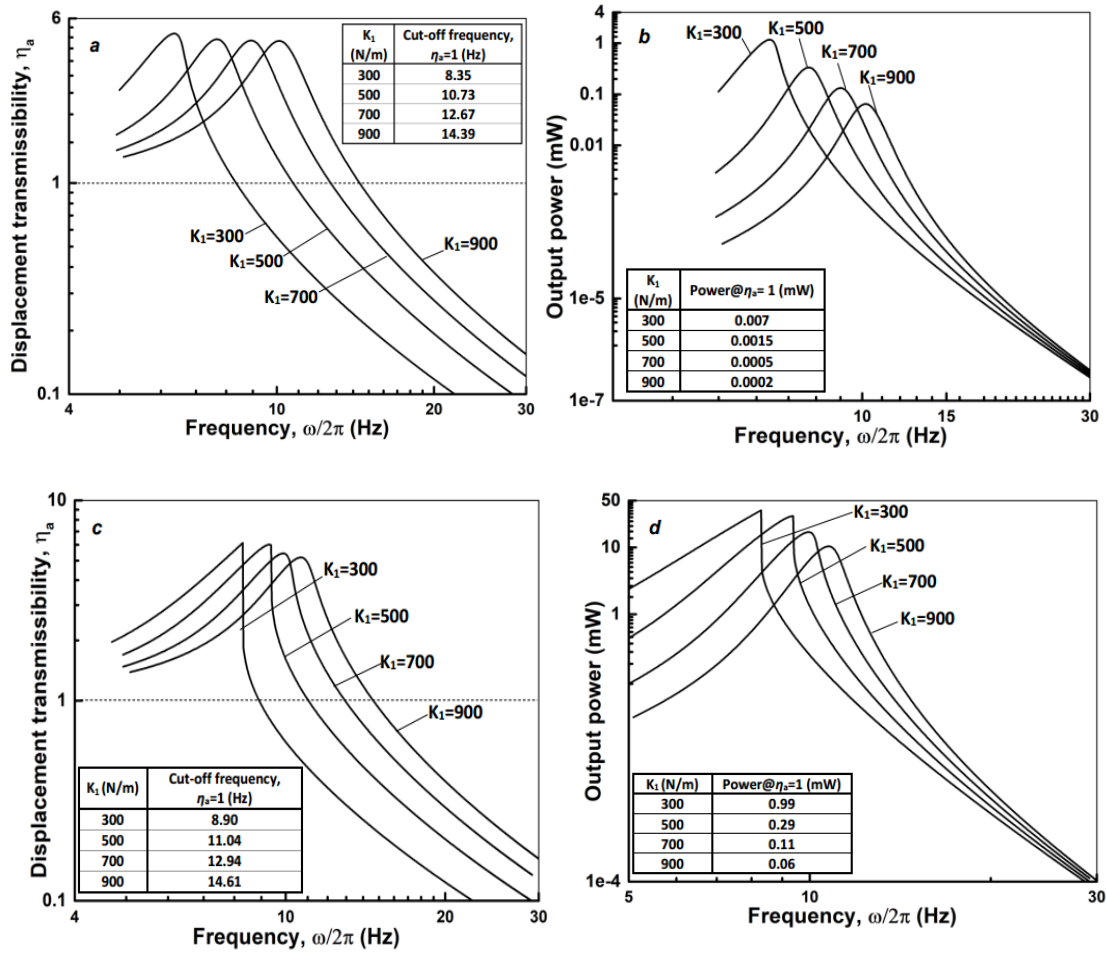


**Figure 39.** Effect of linear stiffness coefficient,  $K_1$  on device performance: (a) and (c): displacement transmissibility at  $0.25g$  and  $1g$  [ $m/s^2$ ], respectively, (b) and (d): generated power at  $0.25g$  and  $1g$  [ $m/s^2$ ], respectively. Nominal values  $R_{Load}=900 \Omega$ ,  $\xi_1=0.11$ ,  $K_3=1.368e6 N m^{-3}$ .

That is, the power extracted at  $K_1 = 500 N \cdot m^{-1}$  increases from  $0.0015$  [mW] to  $0.29$  [mW] when the acceleration level is increased from  $0.25 g$  to  $1.0 g$  [ $m/s^2$ ], respectively.

The sensitivity of the dual-purpose device to variations in nonlinear stiffness coefficient,  $K_3$ , is shown in **Figure 40** at two different acceleration levels, i.e.  $0.25 g$  and  $1.0 g$  [ $m/s^2$ ]. For acceleration level of  $0.25 g$  [ $m/s^2$ ], the effect of nonlinear stiffness coefficient is insignificant on both transmissibility and power recovery. Beyond

frequency peaks, both displacement transmissibility and power harvesting characteristics are almost independent from the nonlinear stiffness coefficient,  $K_3$ . At higher acceleration level, i.e.  $1.0 \text{ g}$  [ $\text{m/s}^2$ ], the nonlinear stiffness manifests itself and appears as a sharp drop in frequency response of both transmissibility and power harvesting curves. At  $1.0 \text{ g}$  [ $\text{m/s}^2$ ], it is also noticed that larger nonlinear stiffness coefficients,  $K_3$ , show stronger nonlinear effects as evident by the sharp drop in frequency response and shift in the frequency response to the right, i.e. hardening effects.

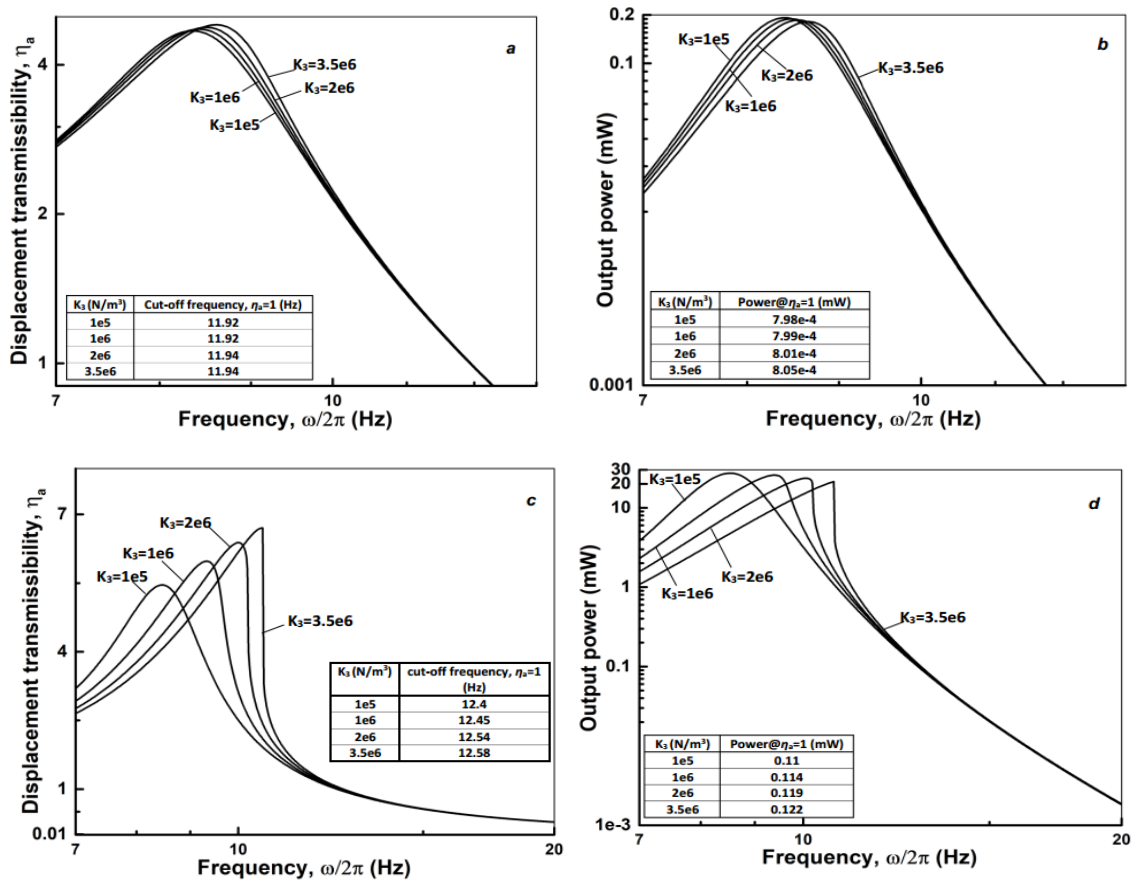


**Figure 40.** Effect of nonlinear stiffness coefficient,  $K_3$  on device performance: (a) and (c): displacement transmissibility at  $0.25\text{g}$  and  $1\text{g}$  [ $\text{m/s}^2$ ], respectively, (b) and (d): generated power at  $0.25\text{g}$  and  $1\text{g}$  [ $\text{m/s}^2$ ], respectively. Nominal values  $R_{Load}=900 \ \Omega$ ,  $\xi_1=0.11$ ,  $K_1=618.6 \ \text{N m}^{-1}$ .

This is because nonlinearity effects become more evident at higher level of excitations. Lastly, for fixed nonlinear stiffness coefficient,  $K_3$  higher acceleration levels improve the power output while slightly increase cut-off frequency. At  $K_3 = 3.5e6 \text{ N.m}^{-3}$ , the power output increased from 0.0008 [mW] to 0.122 [mW], while the cut-off frequency slightly changed from 11.94 [Hz] to 12.58 [Hz] at 0.25 g to 1.0 g [ $\text{m/s}^2$ ], respectively.

**Figure 41** depicts the effect of load resistance,  $R_{Load}$ , on transmissibility and power generation at both 0.25 g and 1.0 g [ $\text{m/s}^2$ ]. Results suggest that there exists an optimum load resistance to maximize power extraction. Output power climbs to a maximum value and drops afterward. This is expected since maximum power transfer occurs when load resistance approximately matches coil resistance, i.e.  $R_{Load} \cong R_{coil}$  [11]. It is also evident that for the simulated values, i.e.  $100 [\Omega] < R_{Load} < 10000 [\Omega]$ , the effect of load resistance,  $R_{Load}$ , on transmissibility is minimal, as suggested in **Figure 41**. Nonetheless, load resistance minimum contributes to the magnetic damping,  $c_m$ . In the dual-purpose device, the total damping  $c_1 = c_a + c_m$  is mostly dominated by viscous damping, i.e  $c_a = 2.389 [\text{N} \cdot \frac{\text{s}}{\text{m}}]$ , compared to  $c_m = 0.051 [\text{N} \cdot \frac{\text{s}}{\text{m}}]$ .

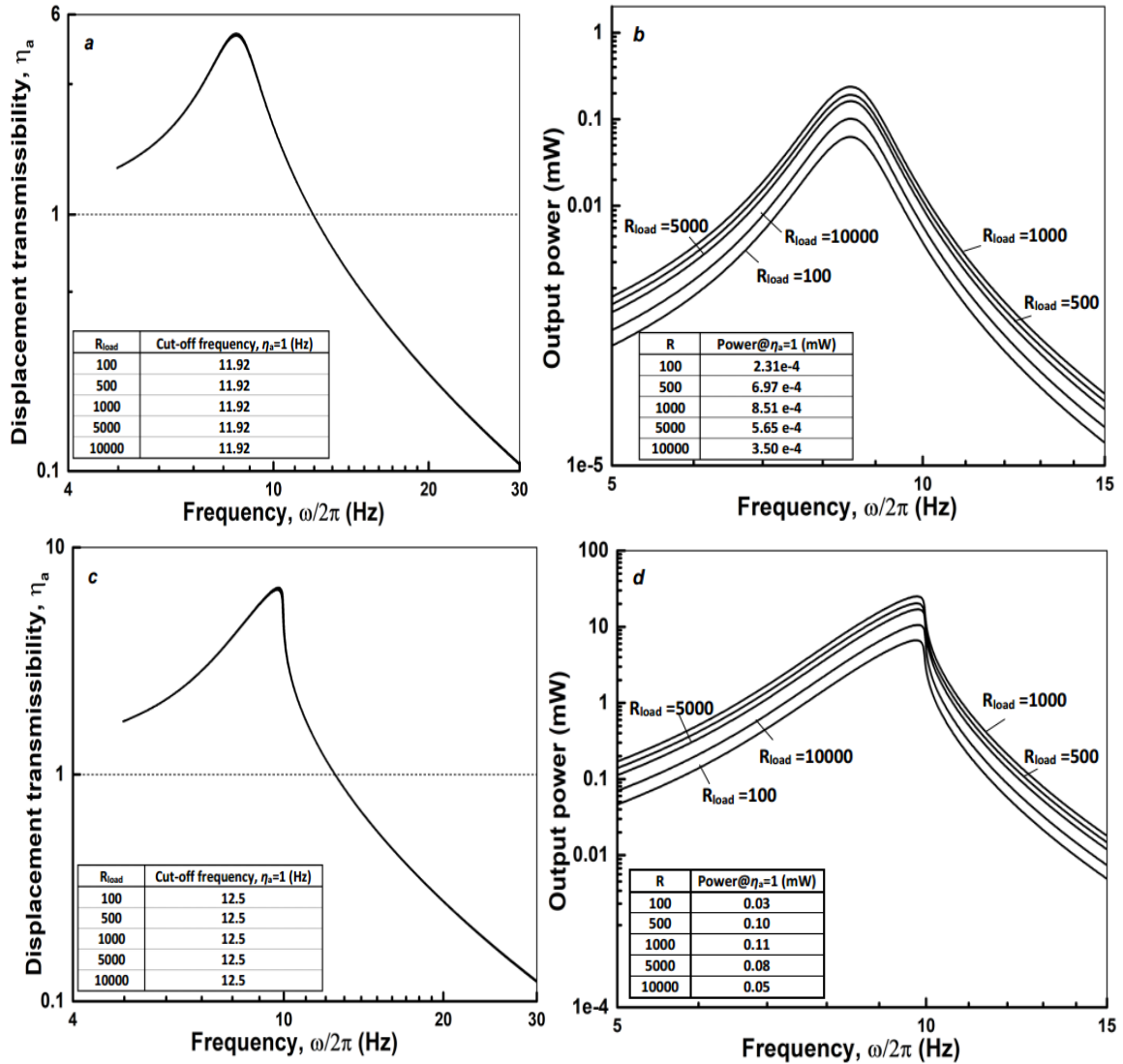


**Figure 41.** Effect of load resistance,  $R_{Load}$ , on device performance: (a) and (c): displacement transmissibility at 0.25g and 1g [m/s<sup>2</sup>], respectively, (b) and (d): generated power at 0.25g and 1g[m/s<sup>2</sup>], respectively. Nominal values  $\xi_1=0.11$ ,  $K_1=618.6$  N m<sup>-1</sup>,  $K_3=1.368e6$  N m<sup>-3</sup>.

The effect of total damping,  $\xi_1 = \frac{C_a+C_m}{2m\omega_n}$ , on the performance of the dual-purpose

device is further investigated in **Figure 42**. Before cut-off frequency, lower damping results in higher transmissibility and increased output power. Nonetheless, this region of operation is not of significance because vibration isolators are meant to operate beyond cut-off frequency, i.e. when  $\eta_a \leq 1$ . Also, results suggest that the cut-off frequency

where transmissibility drops to unity, i.e.  $\eta_a = 1$ , is almost independent from damping. For a fixed frequency beyond cut-off frequency, lower damping reduces transmissibility and improves output power.

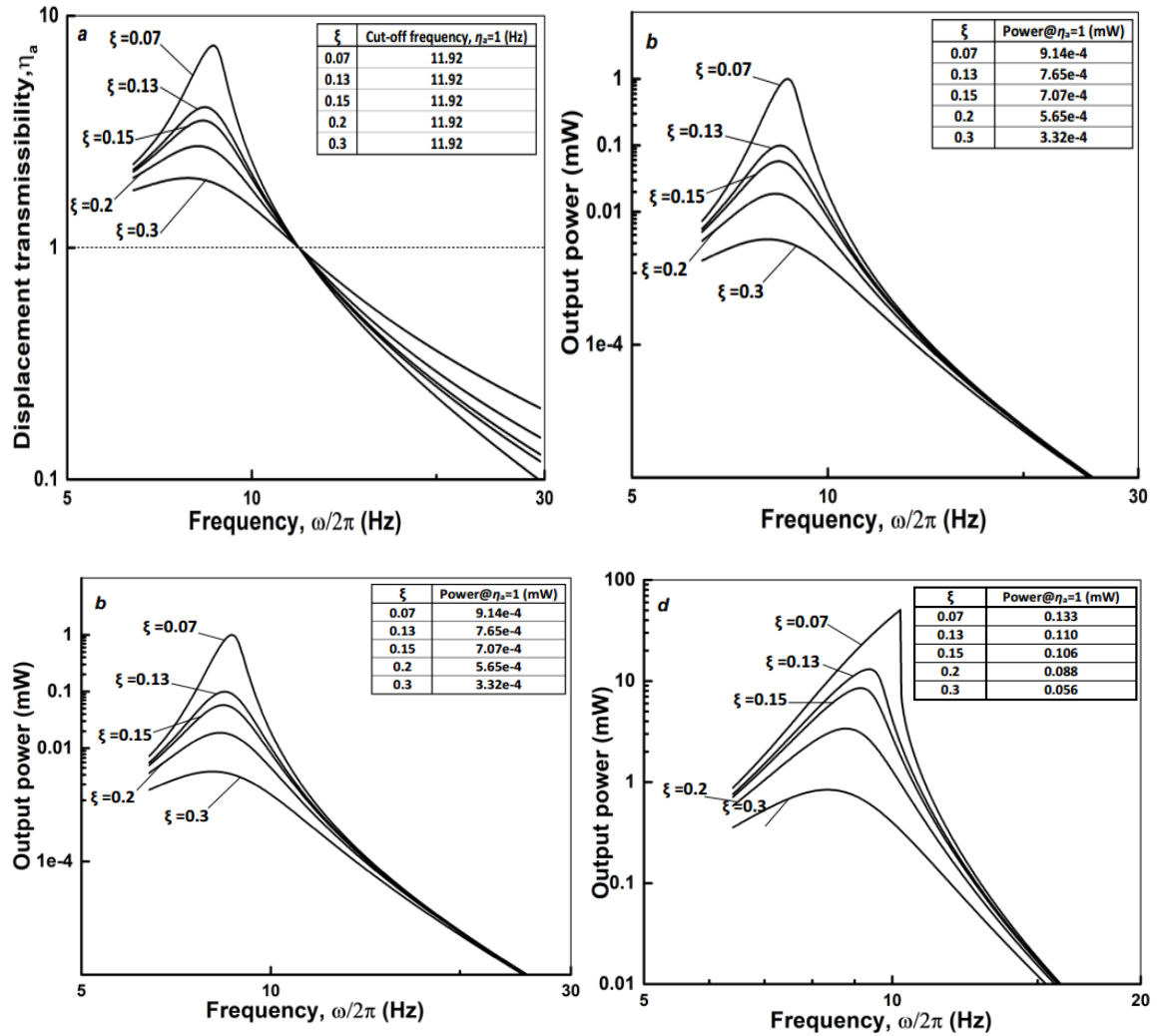


**Figure 42.** Effect of damping,  $\xi_1$  on device performance: (a) and (c): displacement transmissibility at 0.25g and 1g [ $\text{m/s}^2$ ], respectively, (b) and (d): generated power at 0.25g and 1g [ $\text{m/s}^2$ ], respectively. Nominal values  $R_{Load}=900 \Omega$ ,  $K_1=618.6 \text{ N m}^{-1}$ ,  $K_3=1.368e6 \text{ N m}^{-3}$ .

## **CHAPTER 5**

### **CONCLUSIONS**

In this dissertation, we studied a dual purpose vibration isolation energy harvester (VI-EH) design. Growing demands of onboard sensors and gadgets that are exposed to environmental vibrations highlight the vital role of such devices for next generation of technology. In the first step, theoretical study was performed using both numerical (Runge-Kutta) and analytical (Harmonic Balance Method or HBM) approaches. Results showed that a combination of magnetic spring with positive nonlinear stiffness and mechanical spring with negative stiffness is able to shift the cut-off frequency to the lower frequencies which improves the transmissibility metrics of the device. Also, it was shown that results from HBM method is in good agreement to numerical approach. In the next step, design and fabrication of the prototype using rapid manufacturing technique accomplished. To fully understand the behavior and characteristics of the device, a full testing setup was built and used to run the experiments. Also, the magnetic field simulations and magnetic spring stiffness were simulated using COMSOL software and the results were compared to the experimental data. The dynamic tests were performed at different accelerations levels to examine the ability of the device to isolate vibrations from different input sources. Results showed that the combination of mechanical flat spiral spring and magnetic spring reduces the resonant frequency of the

dual purpose device. Moreover, results demonstrate the ability of the dual-purpose device to isolate vibrations and generate useful electric energy during dynamic operation.

During the experiment, the dual-purpose device successfully attenuated oscillations higher than 12.5 [Hz]. The device also produced 26.8 [mW] of output power.

Nonetheless, since the primary function (vibration isolation) of the VI-EH system is achieved harvesting some of the free and abundant kinetic energy contained in these oscillations (secondary function) may be useful in the future as power requirements for onboard sensors is continuously dropping. However, other design improvements may lead to improved power metrics. So, for future works, using a nonlinear damping element in the system as well as softening stiffness nonlinearities may be used to improve the performance of the system.

**APPENDIX A**  
**NOMENCLATURE**

| Symbol          | Description  | Unit                        |
|-----------------|--|-----------------------------|
| $A$             | Amplitude of input base excitation   | m                           |
| $\bar{A}$       | Non-dimensional amplitude of input base excitation   | Unitless                    |
| $a$             | Projected length of oblique spring in horizontal direction   | m                           |
| $a_0$           | Length of oblique spring   | m                           |
| $B$             | Magnetic flux density  | T                           |
| $c_1$           | Linear damping coefficient   | $\text{N s m}^{-1}$         |
| $c_3$           | Non-linear damping coefficient   | $\text{N s}^3\text{m}^{-3}$ |
| $c_a$           | air viscous damping  | $\text{N s m}^{-1}$         |
| $c_m$           | magnetic damping   | $\text{N s m}^{-1}$         |
| $F_{mag}$       | Magnetic spring force  | N                           |
| $\mathcal{F}_s$ | Force of a single oblique spring along its axis  | N                           |
| $F_{s,a}$       | Taylor series expansion of total oblique springs force in vertical direction.                        | N                           |
| $F_s$           | Total oblique springs force in vertical direction  | N                           |
| $F_t$           | Total restoring force of the system in vertical direction  | N                           |
| $\bar{F}_t$     | Non-dimensional total restoring force of the system in vertical direction.                           | Unitless                    |
| $\bar{F}_{t,a}$ | Taylor series approximated non-dimensional total restoring force of the system in vertical direction | Unitless                    |
| $\bar{K}$       | Non-dimensional total stiffness of the system  | Unitless                    |
| $K_1$           | Total linear stiffness coefficient   | $\text{N m}^{-1}$           |
| $K_3$           | Total non-linear stiffness coefficient   | $\text{N m}^{-3}$           |
| $\bar{K}_a$     | Taylor series approximated non-dimensional total stiffness of the system                             | Unitless                    |

|                      |  |                   |
|----------------------|--|-------------------|
| $k_{m1}$             | Linear stiffness of magnetic spring                | $\text{N m}^{-1}$ |
| $k_{m3}$             | Non-linear stiffness of magnetic spring            | $\text{N m}^{-3}$ |
| $k_s$                | Linear stiffness of oblique spring                 | $\text{N m}^{-1}$ |
| $k_{ss}$             | Linear stiffness of spiral spring                  | $\text{N m}^{-1}$ |
| $m$                  | Total mass of isolated object and levitated magnet | $\text{Kg}$       |
| $n$                  | Number of oblique spring                           | Unitless          |
| $P$                  | Output power                                       | $\text{W}$        |
| $R$                  | Coil resistance                                    | $\Omega$          |
| $R_L$                | Load resistance                                    | $\Omega$          |
| $t$                  | Time   | $\text{s}$        |
| $V$                  | Induced voltage                                    | $\text{v}$        |
| $x$                  | Vertical displacement of moving mass               | $\text{m}$        |
| $\bar{X}$            | Non-dimensional response amplitude of the system   | Unitless          |
| $y$                  | Base excitation                                    | $\text{m}$        |
|                      |  |                   |
| <b>Greek Symbols</b> |  |                   |
| $\alpha$             | Non-dimensional linear stiffness coefficient       | Unitless          |
| $\beta$              | Non-dimensional nonlinear stiffness coefficient    | Unitless          |
| $\gamma$             | Non-dimensional geometric coefficient              | Unitless          |
| $\Lambda$            | Degree of nonlinearity                             | Unitless          |
| $\eta$               | Displacement transmissibility                      | Unitless          |
| $\eta_a$             | Absolute transmissibility ratio                    | Unitless          |
| $\eta_e$             | energy conversion efficiency                       | Unitless          |
| $\xi_1$              | Non-dimensional linear damping ratio               | Unitless          |

|                |  |                     |
|----------------|--|---------------------|
| $\xi_3$        | Non-dimensional non-linear damping ratio             | Unitless            |
| $\sigma$       | Non-dimensional geometric Coefficient                | Unitless            |
| $\tau$         | Non-dimensional time scale                           | Rad                 |
| $\varphi$      | Input excitation phase shift                         | Rad                 |
| $\chi$         | Relative displacement of moving mass                 | m                   |
| $\dot{\chi}$   | Relative velocity of moving mass                     | m s <sup>-1</sup>   |
| $\ddot{\chi}$  | Relative acceleration of moving mass                 | m s <sup>-2</sup>   |
| $\bar{\chi}$   | Non-dimensional relative displacement of moving mass | Unitless            |
| $\bar{\chi}'$  | Non-dimensional relative velocity of moving mass     | Unitless            |
| $\bar{\chi}''$ | Non-dimensional relative acceleration of moving mass | Unitless            |
| $\psi$         | Inclination angle                                    | Rad                 |
| $\omega$       | Input excitation frequency                           | Rad s <sup>-1</sup> |
| $\omega_n$     | Resonant frequency                                   | Rad s <sup>-1</sup> |
| $\Omega$       | Non-dimensional frequency                            | Unitless            |

## BIBLIOGRAPHY

- [1] Sazonov E, Li H, Curry D, Pillay P. Self-powered sensors for monitoring of highway bridges. *IEEE Sensors Journal*. 2009 Nov;9(11):1422-9.
- [2] Wu, Z., et al., An energy harvesting bracelet. *Applied Physics Letters*, 2017. 111(1): p. 013903.
- [3] Zhang, Z., et al., A high-efficiency energy regenerative shock absorber using supercapacitors for renewable energy applications in range extended electric vehicle. *Applied Energy*, 2016. 178: p. 177-188.
- [4] Lin, X. and G. Xuexun. Hydraulic transmission electromagnetic energy-regenerative active suspension and its working principle. in *2010 2nd International Workshop on Intelligent Systems and Applications*. 2010.
- [5] Gonzalez-Buelga A, Clare LR, Cammarano A, Neild SA, Burrow SG, Inman DJ. An optimised tuned mass damper/harvester device. *Structural Control and Health Monitoring*. 2014 Aug;21(8):1154-69.
- [6] Frahm, H., Device for damping vibrations of bodies. 1911, Google Patents.
- [7] Kwon, S.-C. and H.-U. Oh, Experimental validation of satellite micro-jitter management strategy in energy harvesting and vibration isolation. *Sensors and Actuators A: Physical*, 2016. 249: p. 172-185.
- [8] Snowdon, J.C., Vibration isolation: use and characterization. *The Journal of the Acoustical Society of America*, 1979. 66(5): p. 1245-1274.
- [9] Seah, W.K., Z.A. Eu, and H.-P. Tan. Wireless sensor networks powered by ambient energy harvesting (WSN-HEAP)-Survey and challenges. in *Wireless Communication, Vehicular Technology, Information Theory and Aerospace & Electronic Systems Technology*, 2009. *Wireless VITAE 2009. 1st International Conference on*. 2009. Ieee.
- [10] Bowen CR, Arafa MH. Energy harvesting technologies for tire pressure monitoring systems. *Advanced Energy Materials*. 2015 Apr;5(7):1401787.
- [11] Park, G., et al., Energy harvesting for structural health monitoring sensor networks. *Journal of Infrastructure Systems*, 2008. 14(1): p. 64-79.

- [12] Priya, S. and D.J. Inman, Energy harvesting technologies. Vol. 21. 2009: Springer.
- [13] Stephen, N., On energy harvesting from ambient vibration. *Journal of sound and vibration*, 2006. 293(1-2): p. 409-425.
- [14] Roundy, S., et al., Improving power output for vibration-based energy scavengers. *IEEE Pervasive computing*, 2005. 4(1): p. 28-36.
- [15] Li Y, Baker E, Reissman T, Sun C, Liu WK. Design of mechanical metamaterials for simultaneous vibration isolation and energy harvesting. *Applied Physics Letters*. 2017 Dec 18;111(25):251903.
- [16] Hu G, Tang L, Banerjee A, Das R. Metastructure with piezoelectric element for simultaneous vibration suppression and energy harvesting. *Journal of Vibration and Acoustics*. 2017 Feb 1;139(1):011012.
- [17] Davis RB, McDowell MD. Combined Euler column vibration isolation and energy harvesting. *Smart Materials and Structures*. 2017 Apr 4;26(5):055001.
- [18] Li Z, Zuo L, Kuang J, Luhrs G. Energy-harvesting shock absorber with a mechanical motion rectifier. *Smart Materials and Structures*. 2012 Dec 21;22(2):025008.
- [19] Ali SF, Adhikari S. Energy harvesting dynamic vibration absorbers. *Journal of Applied Mechanics*. 2013 Jul 1;80(4):041004.
- [20] Madhav C, Ali SF. Harvesting energy from vibration absorber under random excitations. *IFAC-PapersOnLine*. 2016 Jan 1;49(1):807-12.
- [21] Tang X, Zuo L. Simultaneous energy harvesting and vibration control of structures with tuned mass dampers. *Journal of Intelligent Material Systems and Structures*. 2012 Dec;23(18):2117-27.
- [22] Di Monaco F, Tehrani MG, Elliott SJ, Bonisoli E, Tornincasa S. Energy harvesting using semi-active control. *Journal of Sound and Vibration*. 2013 Nov 11;332(23):6033-43.
- [23] Chtiba MO, Choura S, Nayfeh AH, El-Borgi S. Vibration confinement and energy harvesting in flexible structures using collocated absorbers and piezoelectric devices. *Journal of Sound and Vibration*. 2010 Feb 1;329(3):261-76.
- [24] Fang Z, Guo X, Xu L, Zhang H. Experimental study of damping and energy regeneration characteristics of a hydraulic electromagnetic shock absorber. *Advances in Mechanical Engineering*. 2013;5:943528.

- [25] Ding R, Wang R, Meng X, Chen L. Study on coordinated control of the energy regeneration and the vibration isolation in a hybrid electromagnetic suspension. *Proceedings of the Institution of Mechanical Engineers, Part D: Journal of Automobile Engineering*. 2017 Sep;231(11):1530-9.
- [26] Pei Y, Liu Y, Zuo L. Multi-resonant electromagnetic shunt in base isolation for vibration damping and energy harvesting. *Journal of Sound and Vibration*. 2018 Jun 9;423:1-7.
- [27] Kan J, Liu D, Wang S, Wang B, Yu L, Li S. A piezohydraulic vibration isolator used for energy harvesting. *Journal of Intelligent Material Systems and Structures*. 2014 Sep;25(14):1727-37.
- [28] Huang B, Hsieh CY, Golnaraghi F, Moallem M. Development and optimization of an energy-regenerative suspension system under stochastic road excitation. *Journal of Sound and Vibration*. 2015 Nov 24;357:16-34.
- [29] Sapiński B. Experimental study of a self-powered and sensing MR-damper-based vibration control system. *Smart Materials and Structures*. 2011 Aug 31;20(10):105007.
- [30] Liu C, Jing X, Daley S, Li F. Recent advances in micro-vibration isolation. *Mechanical Systems and Signal Processing*. 2015 May 1;56:55-80.
- [31] Maciejewski I, Meyer L, Krzyzynski T. Modelling and multi-criteria optimisation of passive seat suspension vibro-isolating properties. *Journal of Sound and Vibration*. 2009 Jul 24;324(3-5):520-38.
- [32] Maciejewski I, Meyer L, Krzyzynski T. The vibration damping effectiveness of an active seat suspension system and its robustness to varying mass loading. *Journal of sound and vibration*. 2010 Sep 13;329(19):3898-914.
- [33] Zuo L, Zhang PS. Energy harvesting, ride comfort, and road handling of regenerative vehicle suspensions. *Journal of Vibration and Acoustics*. 2013 Feb 1;135(1):011002.
- [34] Ibrahim RA. Recent advances in nonlinear passive vibration isolators. *Journal of sound and vibration*. 2008 Jul 22;314(3-5):371-452.
- [35] Sun X, Jing X. Multi-direction vibration isolation with quasi-zero stiffness by employing geometrical nonlinearity. *Mechanical systems and signal processing*. 2015 Oct 1;62:149-63.
- [36] Zhang W, Zhao J. Analysis on nonlinear stiffness and vibration isolation performance of scissor-like structure with full types. *Nonlinear Dynamics*. 2016 Oct 1;86(1):17-36.

- [37] Benacchio S, Malher A, Boisson J, Touzé C. Design of a magnetic vibration absorber with tunable stiffnesses. *Nonlinear Dynamics*. 2016 Jul 1;85(2):893-911.
- [38] Xu D, Yu Q, Zhou J, Bishop SR. Theoretical and experimental analyses of a nonlinear magnetic vibration isolator with quasi-zero-stiffness characteristic. *Journal of Sound and Vibration*. 2013 Jul 8;332(14):3377-89.
- [39] Jing XJ, Lang ZQ, Billings SA. Output frequency response function-based analysis for nonlinear Volterra systems. *Mechanical systems and signal processing*. 2008 Jan 1;22(1):102-20.
- [40] Jing XJ, Lang ZQ, Billings SA, Tomlinson GR. Frequency domain analysis for suppression of output vibration from periodic disturbance using nonlinearities. *Journal of Sound and vibration*. 2008 Jul 22;314(3-5):536-57.
- [41] Jing XJ, Lang ZQ. Frequency domain analysis of a dimensionless cubic nonlinear damping system subject to harmonic input. *Nonlinear Dynamics*. 2009 Nov 1;58(3):469.
- [42] Lang ZQ, Billings SA, Yue R, Li J. Output frequency response function of nonlinear Volterra systems. *Automatica*. 2007 May 1;43(5):805-16.
- [43] Lang ZQ, Jing XJ, Billings SA, Tomlinson GR, Peng ZK. Theoretical study of the effects of nonlinear viscous damping on vibration isolation of sdof systems. *Journal of Sound and Vibration*. 2009 Jun 5;323(1-2):352-65.
- [44] Guo PF, Lang ZQ, Peng ZK. Analysis and design of the force and displacement transmissibility of nonlinear viscous damper based vibration isolation systems. *Nonlinear Dynamics*. 2012 Mar 1;67(4):2671-87.
- [45] Laalej H, Lang ZQ, Daley S, Zazas I, Billings SA, Tomlinson GR. Application of non-linear damping to vibration isolation: an experimental study. *Nonlinear Dynamics*. 2012 Jul 1;69(1-2):409-21.
- [46] Wu W, Chen X, Shan Y. Analysis and experiment of a vibration isolator using a novel magnetic spring with negative stiffness. *Journal of Sound and Vibration*. 2014 Jun 23;333(13):2958-70.
- [47] Shi X, Zhu S. Magnetic negative stiffness dampers. *Smart materials and structures*. 2015 Jun 17;24(7):072002.
- [48] Carrella A, Brennan MJ, Waters TP, Shin K. On the design of a high-static–low-dynamic stiffness isolator using linear mechanical springs and magnets. *Journal of Sound and Vibration*. 2008 Aug 19;315(3):712-20.

- [49] Robertson WS, Kidner MR, Cazzolato BS, Zander AC. Theoretical design parameters for a quasi-zero stiffness magnetic spring for vibration isolation. *Journal of Sound and Vibration*. 2009 Sep 25;326(1-2):88-103.
- [50] Virgin LN, Santillan ST, Plaut RH. Vibration isolation using extreme geometric nonlinearity. *Journal of Sound and Vibration*. 2008 Aug 19;315(3):721-31.
- [51] Gatti G, Kovacic I, Brennan MJ. On the response of a harmonically excited two degree-of-freedom system consisting of a linear and a nonlinear quasi-zero stiffness oscillator. *Journal of Sound and Vibration*. 2010 May 10;329(10):1823-35.
- [52] Sun X, Jing X. A nonlinear vibration isolator achieving high-static-low-dynamic stiffness and tunable anti-resonance frequency band. *Mechanical Systems and Signal Processing*. 2016 Dec 1;80:166-88.
- [53] Van Trung P, Kim KR, Ahn HJ. A nonlinear control of an QZS isolator with flexures based on a Lyapunov function. *International Journal of Precision Engineering and Manufacturing*. 2013 Jun 1;14(6):919-24.
- [54] Le TD, Ahn KK. Experimental investigation of a vibration isolation system using negative stiffness structure. *International Journal of Mechanical Sciences*. 2013 May 1;70:99-112.
- [55] Liu X, Huang X, Hua H. On the characteristics of a quasi-zero stiffness isolator using Euler buckled beam as negative stiffness corrector. *Journal of Sound and Vibration*. 2013 Jul 8;332(14):3359-76.
- [56] Xu D, Zhang Y, Zhou J, Lou J. On the analytical and experimental assessment of the performance of a quasi-zero-stiffness isolator. *Journal of Vibration and Control*. 2014 Nov;20(15):2314-25.
- [57] Kovacic I, Brennan MJ, Waters TP. A study of a nonlinear vibration isolator with a quasi-zero stiffness characteristic. *Journal of sound and vibration*. 2008 Aug 19;315(3):700-11.
- [58] Wu Z, Jing X. A bio-inspired structure for vibration isolation. In 2015 IEEE International Conference on Cyber Technology in Automation, Control, and Intelligent Systems (CYBER) 2015 Jun 8 (pp. 2079-2084). IEEE.
- [59] Mann BP, Sims ND. Energy harvesting from the nonlinear oscillations of magnetic levitation. *Journal of Sound and Vibration*. 2009 Jan 9;319(1-2):515-30.
- [60] Apo DJ, Priya S. High power density levitation-induced vibration energy harvester. *Energy Harvesting and Systems*. 2014 Jun 1;1(1-2):79-88.

[61] Lee C, Stamp D, Kapania NR, Mur-Miranda JO. Harvesting vibration energy using nonlinear oscillations of an electromagnetic inductor. In *Energy Harvesting and Storage: Materials, Devices, and Applications* 2010 Apr 29 (Vol. 7683, p. 76830Y). International Society for Optics and Photonics.

[62] Tehrani MG, Elliott SJ. Extending the dynamic range of an energy harvester using nonlinear damping. *Journal of Sound and Vibration*. 2014 Feb 3;333(3):623-9.

[63] Elliott SJ, Tehrani MG, Langley RS. Nonlinear damping and quasi-linear modelling. *Philosophical Transactions of the Royal Society A: Mathematical, Physical and Engineering Sciences*. 2015 Sep 28;373(2051):20140402.

[64] Ruzicka JE, Derby TF. Influence of damping in vibration isolation. *SHOCK AND VIBRATION INFORMATION CENTER (DEFENSE) WASHINGTON DC*; 1971.

[65] Laalej H, Lang ZQ. Numerical investigation of the effects of mr damper characteristic parameters on vibration isolation of SDOF systems under harmonic excitations. *Journal of Intelligent Material Systems and Structures*. 2010 Mar;21(5):483-501.

[66] Sims ND, Stanway R, Peel DJ, Bullough WA, Johnson AR. Controllable viscous damping: an experimental study of an electrorheological long-stroke damper under proportional feedback control. *Smart materials and structures*. 1999 Oct;8(5):601.

[67] Sims ND, Stanway R, Johnson AR, Peel DJ, Bullough WA. Smart fluid damping: shaping the force/velocity response through feedback control. *Journal of intelligent material systems and structures*. 2000 Dec;11(12):945-58.

[68] Green PL, Worden K, Atallah K, Sims ND. The effect of duffing-type nonlinearities and coulomb damping on the response of an energy harvester to random excitations. *Journal of Intelligent Material Systems and Structures*. 2012 Dec;23(18):2039-54.

[69] Nammari A, Bardaweel H. Design enhancement and non-dimensional analysis of magnetically-levitated nonlinear vibration energy harvesters. *Journal of Intelligent Material Systems and Structures*. 2017 Nov;28(19):2810-22.

[70] Robertson W, Cazzolato B, Zander A. A simplified force equation for coaxial cylindrical magnets and thin coils. *IEEE Transactions on Magnetics*. 2011 Aug;47(8):2045-9.

[71] Van Deun J, Cools R. Integrating products of Bessel functions with an additional exponential or rational factor. *Computer Physics Communications*. 2008 Apr 15;178(8):578-90.

- [72] Vokoun D, Beleggia M, Heller L, Šittner P. Magnetostatic interactions and forces between cylindrical permanent magnets. *Journal of magnetism and Magnetic Materials*. 2009 Nov 1;321(22):3758-63.
- [73] Rivin EI. *Dynamic Properties of Vibration Isolation Systems*. In *Passive Vibration Isolation 2003*. Asme press.
- [74] Collette C, Janssens S, Artoos K. Review of active vibration isolation strategies. *Recent patents on Mechanical engineering*. 2011 Sep 1;4(3):212-9.
- [75] Winthrop MF, Cobb RG. Survey of state-of-the-art vibration isolation research and technology for space applications. In *Smart structures and materials 2003: Damping and isolation 2003 Jul 31 (Vol. 5052, pp. 13-27)*. International Society for Optics and Photonics.
- [76] Ravindra B, Mallik AK. Performance of non-linear vibration isolators under harmonic excitation. *Journal of Sound and Vibration*. 1994 Feb 24;170(3):325-37.
- [77] Wang Y, Wang RC, Meng HD. Analysis and comparison of the dynamic performance of one-stage inerter-based and linear vibration isolators. *International Journal of Applied Mechanics*. 2018 Jan 29;10(01):1850005.
- [78] Mofidian SM, Bardaweel H. Displacement transmissibility evaluation of vibration isolation system employing nonlinear-damping and nonlinear-stiffness elements. *Journal of Vibration and Control*. 2018 Sep;24(18):4247-59.
- [79] Bian J, Jing X. Superior nonlinear passive damping characteristics of the bio-inspired limb-like or X-shaped structure. *Mechanical Systems and Signal Processing*. 2019 Jun 15;125:21-51.
- [80] Zhou N, Liu K. A tunable high-static–low-dynamic stiffness vibration isolator. *Journal of Sound and Vibration*. 2010 Apr 26;329(9):1254-73.
- [81] Dong G, Zhang X, Xie S, Yan B, Luo Y. Simulated and experimental studies on a high-static-low-dynamic stiffness isolator using magnetic negative stiffness spring. *Mechanical Systems and Signal Processing*. 2017 Mar 1;86:188-203.
- [82] Dhote S, Yang Z, Behdinan K, Zu J. Enhanced broadband multi-mode compliant orthoplanar spring piezoelectric vibration energy harvester using magnetic force. *International Journal of Mechanical Sciences*. 2018 Jan 1;135:63-71.
- [83] Zhu T, Cazzolato B, Robertson WS, Zander A. Vibration isolation using six degree-of-freedom quasi-zero stiffness magnetic levitation. *Journal of Sound and Vibration*. 2015 Dec 8;358:48-73.

- [84] Zheng Y, Zhang X, Luo Y, Zhang Y, Xie S. Analytical study of a quasi-zero stiffness coupling using a torsion magnetic spring with negative stiffness. *Mechanical Systems and Signal Processing*. 2018 Feb 1;100:135-51.
- [85] Sodano HA, Bae JS, Inman DJ, Belvin WK. Concept and model of eddy current damper for vibration suppression of a beam. *Journal of Sound and Vibration*. 2005 Dec 20;288(4-5):1177-96.
- [86] Ebrahimi B, Khamesee MB, Golnaraghi MF. Design and modeling of a magnetic shock absorber based on eddy current damping effect. *Journal of Sound and Vibration*. 2008 Sep 9;315(4-5):875-89.
- [87] Ramlan R, Brennan MJ, Mace BR, Kovacic I. Potential benefits of a non-linear stiffness in an energy harvesting device. *Nonlinear dynamics*. 2010 Mar 1;59(4):545-58.
- [88] Tse FS, Morse IE, Hinkle RT. *Mechanical Vibrations, Theory and Applications*, Allyn and Becon. Inc.(Pearson Publishers). 1978.
- [89] Olaru R, Gherca R, Petrescu C. Analysis and design of a vibration energy harvester using permanent magnets. *Revue Roumaine des Sciences Techniques-Serie Electrotechnique*. 2014 Apr 1;59(2):131-40.
- [90] Bendame M, Abdel-Rahman E, Soliman M. Wideband, low-frequency springless vibration energy harvesters: part I. *Journal of Micromechanics and Microengineering*. 2016 Oct 19;26(11):115021.
- [91] Gutierrez M, Shahidi A, Berdy D, Peroulis D. Design and characterization of a low frequency 2-dimensional magnetic levitation kinetic energy harvester. *Sensors and Actuators A: Physical*. 2015 Dec 1;236:1-0.
- [92] Berdy DF, Valentino DJ, Peroulis D. Design and optimization of a magnetically sprung block magnet vibration energy harvester. *Sensors and actuators A: Physical*. 2014 Oct 1;218:69-79.
- [93] Mofidian SM, Bardaweel H. Theoretical study and experimental identification of elastic-magnetic vibration isolation system. *Journal of Intelligent Material Systems and Structures*. 2018 Nov;29(18):3550-61.
- [94] Elvin N, Erturk A, editors. *Advances in energy harvesting methods*. Springer Science & Business Media; 2013 Feb 15.
- [95] Tao K, Lye SW, Miao J, Hu X. Design and implementation of an out-of-plane electrostatic vibration energy harvester with dual-charged electret plates. *Microelectronic Engineering*. 2015 Mar 5;135:32-7.

- [96] Bu L, Wu X, Wang X, Liu L. Non-resonant electrostatic energy harvester for wideband applications. *Micro & Nano Letters*. 2013 Mar 1;8(3):135-7.
- [97] Anton SR, Sodano HA. A review of power harvesting using piezoelectric materials (2003–2006). *Smart materials and Structures*. 2007 May 18;16(3):R1.
- [98] Mallick D, Amann A, Roy S. A nonlinear stretching based electromagnetic energy harvester on FR4 for wideband operation. *Smart Materials and Structures*. 2014 Nov 28;24(1):015013.
- [99] Beeby SP, O'Donnell T. Electromagnetic energy harvesting. In *Energy Harvesting Technologies 2009* (pp. 129-161). Springer, Boston, MA.
- [100] Yang B, Lee C, Xiang W, Xie J, He JH, Kotlanka RK, Low SP, Feng H. Electromagnetic energy harvesting from vibrations of multiple frequencies. *Journal of Micromechanics and Microengineering*. 2009 Jan 30;19(3):035001.
- [101] Karnopp D. Active and semi-active vibration isolation. In *Current Advances in Mechanical Design and Production VI* 1995 Jan 1 (pp. 409-423). Pergamon.
- [102] Soong TT, Costantinou MC, editors. *Passive and active structural vibration control in civil engineering*. Springer; 2014 May 4.
- [103] Patel S, Park H, Bonato P, Chan L, Rodgers M. A review of wearable sensors and systems with application in rehabilitation. *Journal of neuroengineering and rehabilitation*. 2012 Dec;9(1):21.
- [104] Knight C, Davidson J, Behrens S. Energy options for wireless sensor nodes. *Sensors*. 2008;8(12):8037-66.
- [105] Maravandi A, Moallem M. Regenerative shock absorber using a two-leg motion conversion mechanism. *IEEE/ASME Transactions on Mechatronics*. 2015 Dec;20(6):2853-61.
- [106] Jin-qiu Z, Zhi-zhao P, Lei Z, Yu Z. A review on energy-regenerative suspension systems for vehicles. In *Proceedings of the world congress on engineering 2013 Jul 3* (Vol. 3, pp. 3-5).
- [107] Makihara K, Onoda J, Minesugi K. A self-sensing method for switching vibration suppression with a piezoelectric actuator. *Smart Materials and Structures*. 2007 Feb 14;16(2):455.
- [108] Zhang Y, Zhang X, Zhan M, Guo K, Zhao F, Liu Z. Study on a novel hydraulic pumping regenerative suspension for vehicles. *Journal of the Franklin Institute*. 2015 Feb 1;352(2):485-99.

- [109] Noritsugu T. Energy saving of a pneumatic system (2). Energy regenerative control of a pneumatic drive system. Application to active air suspension. *Hydraul. Pneum.* 1999;38:1-4.
- [110] Aoyama Y, Kawabata K, Hasegawa S, Kobari Y, Sato M, Tsuruta E. Development of the full active suspension by Nissan. *SAE transactions.* 1990 Jan 1:1537-45.
- [111] Kovacic I, Brennan MJ. *The Duffing equation: nonlinear oscillators and their behaviour.* John Wiley & Sons; 2011 Feb 11.
- [112] Erturk A, Inman DJ. Broadband piezoelectric power generation on high-energy orbits of the bistable Duffing oscillator with electromechanical coupling. *Journal of Sound and Vibration.* 2011 May 9;330(10):2339-53.
- [113] Karami MA, Inman DJ. Equivalent damping and frequency change for linear and nonlinear hybrid vibrational energy harvesting systems. *Journal of Sound and Vibration.* 2011 Nov 7;330(23):5583-97.
- [114] Kacem N, Baguet S, Hentz S, Dufour R. Computational and quasi-analytical models for non-linear vibrations of resonant MEMS and NEMS sensors. *International Journal of Non-Linear Mechanics.* 2011 Apr 1;46(3):532-42.
- [115] Souayah S, Kacem N. Computational models for large amplitude nonlinear vibrations of electrostatically actuated carbon nanotube-based mass sensors. *Sensors and Actuators A: Physical.* 2014 Feb 1;208:10-20.
- [116] Jallouli A, Kacem N, Bourbon G, Le Moal P, Walter V, Lardies J. Pull-in instability tuning in imperfect nonlinear circular microplates under electrostatic actuation. *Physics Letters A.* 2016 Dec 1;380(46):3886-90.
- [117] Wang Z, Wang B, Wang M, Zhang H, Huang W. Model and experimental study of permanent magnet vibration-to-electrical power generator. *IEEE Transactions on applied superconductivity.* 2010 Jun;20(3):1110-3.
- [118] Brennan MJ, Kovacic I, Carrella A, Waters TP. On the jump-up and jump-down frequencies of the Duffing oscillator. *Journal of Sound and Vibration.* 2008 Dec 23;318(4-5):1250-61.